Studies on the effect of defects and dopants on the optical, photocatalytic and magnetic properties of TiO_2 nanoparticles.

Susmita Paul

Registration Number- TZ121473 OF 2012

A thesis submitted in partial fulfillment of the requirements for the degree of Doctor of Philosophy

Department of Physics

School of Sciences

Tezpur University

Napaam, Tezpur-784028

Assam, India.

November 2014

Dedicated to my parents,

Subhash Chandra Paul

and

Ratna Paul.

ABSTRACT

Nanocrystalline transition metal oxides are of considerable interest owing to their potential applications in a range of processes. These are expected to be the key materials for further applications in the field of science and technology. Among various semiconductors TiO_2 has been a focus of attention because of its excellent properties such as high activity, good stability and non-toxicity. It has been widely used in the fields of renewable energy and ecological environmental protection. However, as a wide band gap semiconductor TiO_2 can show optical absorption and photocatalytic activity only under UV irradiation. Scientists and industrial communists tangled in photocatalytic research are in constant endeavor to intensify the spectral sensitivity of TiO_2 based photocatalyst to visible region. Doping opens up the possibility of changing the electronic structure of TiO_2 with properties better than undoped TiO_2. Nonetheless, doping is also known to have an immense effect on fueling magnetism in this otherwise non-magnetic TiO_2.Tunable ferromagnetism attainable in DMS is one of the leading areas of semiconductor spintronics. Diluted magnetic semiconductors (DMS) represent a synergetic collaboration between charge based semiconductors and spin based magnetism [1]. The discovery of room temperature ferromagnetism in Co-doped anatase TiO_2 has led to intense experimental and theoretical research in the field of doped titanium oxides [2]. Non-Magnetic metal oxide exhibiting room temperature ferromagnetism is a surprising phenomena arising at the nanoregime. Santara.et.al [3] observed ferromagnetism in undoped TiO_2 nanoribbons. The observed magnetism was corroborated to the existence of oxygen vacancies.

The first systematic study on the role of metal ion dopant in quantum size TiO_2 was performed by measuring the photoreactivities and the charge carrier recombination dynamics [4]. Although this study was a pioneer work in the research of metal ion doped TiO_2 , the photoreactivity experiments were carried out under UV light which means that the prepared nanoparticles was not visible light responsive. Many endeavors were made to extend the absorption of metal ion doped TiO_2 to visible region after this pioneering work [5,6]. More recently TiO_2 doped with lanthanide ions has also provoked great interests [7,8]. Lanthanide ions are known for their stability to form complexes with various Lewis bases. They have special electronic structure of $4f^n5d^n$,(n

being the number of electrons) that leads to different optical properties and dissimilar catalytic capacity [9]. Choi.et.al [10] reported the mechanism of Gd doping using density functional theory and addressed the structural benefits of electrodes in accomodating the Gd dopants and their consequences on the photocatalytic degradation. Density functional theory is an extraordinarily valuable method to analyze and throw light on the doping process and its effect on the electronic structure.

The main scope of the thesis is to study the defects and dopant mediated changes in the optical, photocatalytic and magnetic properties of TiO_2 nanoparticles prepared by sol-gel method. In our work we have chosen Ni^{2+}, Mn^{2+} as the transition metal ion dopants and Gd^{3+}, Er^{3+} as the rare-earth metal ion dopants. These dopant ions are chosen as they are expected to introduce their respective *d* or *f* shell in the TiO_2 matrix, inducing photoactive transition in the visible region, thereby throwing light on the use of material as potential photocatalytic candidate on one hand and modulating the magnetic nature of non-magnetic TiO_2 on the other hand. In the thesis theoretical computation based on density functional theory (DFT) has been carried out for Mn and Gd doped TiO_2 nanoparticles to establish the presence of these states. The results obtained from the partial density of states are correlated with the visible light photocatalytic degradation of phenol.

In Chapter 1 the photocatalytic reaction mechanism using TiO_2 as a photocatalyst has been thoroughly discussed. The Density functional theory has been highlighted. Further, the magnetic properties of undoped and doped TiO_2 has been emphasized in a broader aspect. Lastly, few areas of applications of TiO_2 are mentioned based on its different properties.

In Chapter 2 preparation method of pure and doped TiO_2 nanoparticles employing sol-gel method has been discussed. The detailed, structural, morphological and valence state of the dopant ion and its co-ordination environment in TiO_2 are analyzed using X-ray diffraction, Raman spectroscopy, transmission electron microscope (TEM), X-ray photoelectron spectroscopy (XPS) respectively.

Although doping in the semiconductor nanostructures is an important method of tuning the electronic structure and obtaining superior properties. But researchers are also in the search of improving the photocatalytic activity of TiO_2 nanoparticles without adding impurities. Recently the anatase-rutile mixture is found to have a magical effect on the charge transfer process. [11]. In chapter 3 the optical and photocatalytic activity of mixed phase TiO_2 under visible light illumination has been broadly discussed. A

detailed analysis on the emissivity and carrier lifetime have been carried out using steady state and time resolved photoluminescence spectra. Due to the synergistic effect of mixed anatase and rutile phases, mixed phase nanocrystalline titania are found to exhibit superior photocatalytic activity.

Chapter 4 reports some interesting optical and magnetic properties of Ni^{2+} doped TiO_2 nanoparticles. Ni doping introduces *d* states in the band gap of TiO_2 and shifts the optical response from UV to visible region. A remarkable red shift of the absorption edge is observed with increasing nickel content. The photocatalytic activity is significantly increased after doping. Room temperature ferromagnetism is observed in the entire doped nanoparticles and oxygen vacancy mediated exchange interaction is proposed to explain the observed ferromagnetism.

Mn^{2+} serves as an active dopant because of its magnetic and optically active nature. In Chapter 5 based on the studies of lattice strain, Raman spectra and Urbach parameter Mn doping is found to introduce some strong lattice distortion. The changes in the property are attributed to the introduction of Mn 3*d* states. The presence of these states have been identified using DFT study. The chapter than moves on discussing the magnetic nature of Mn doped TiO_2 nanoparticles at room temperature as well as at 10 K. A comparative study on the magnetic behavior of the highest doped sample has been carried out under both aerobic and anaerobic atmosphere. It is surmised that although oxygen vacancies are generated due to doping, the numbers are insufficient in comparison to the vacuum annealed sample to bring any ferromagnetic ordering.

Chapter 6 discusses the enhanced photocatalytic activity of Gd doped TiO_2 nanoparticles due to formation of Gd 4*f* energy levels in the band gap of TiO_2. The PDOS analysis based on DFT study clearly shows the Gd 4*f* state , that is more prominent near Fermi level whereas Ti and O have lesser impact. The other states of Gd i.e., *s*, *p* and *d* has almost no contribution in comparison to the *f* state. Hence *f* state of Gd is the key factor to tune the optical property and increase the photocatalytic efficiency of TiO_2 nanoparticles. In contrast to the usual belief that incorporation of ferromagnetic Gd may induce ferromagnetic signal, we have observed paramagnetism at room temperature as well as at 10 K. To the best of our knowledge there are no reports on magnetism in Gd doped TiO_2 nanoparticles.

Erbium, a member of the lanthanide rare earth series possess 11 electrons in the 4*f* shell. Er doped TiO_2 nanocrystals are mainly used for optical applications [12]. Chapter 7 reports detailed study on the optical and magnetic properties of Er doped

TiO_2 nanoparticles. Compared to undoped TiO_2 the emission intensity of the doped TiO_2 samples is noticeably enhanced, suggesting that the host matrix not only functions as an ideal host for well dispersed and highly accommodated concentration of Er^{3+} but also as a good sensitizer for proficient absorption of light and transfer of energy to Er^{3+} ions. One of the important finding of this chapter is the analysis of magnetic nature of the sample which has not been reported so far. The results clearly suggest absence of any ferromagnetic interaction. There is persistence of antiferromagnetic ordering and it gets stronger at 0.07 mol. The antiferromagnetic nature is ascribed to the super exchange interaction of Er^{3+} via O^{2-}.

Chapter 8 summarizes the results discussed above and highlights the probable areas for the expansion of these works.

Bibliography:

1. Xing,G.Z., Comparative Study of Room- Temperature Ferromagnetism in Cu-Doped ZnO Nanowires Enhanced by Structural Inhomogeneity, *Adv. Mater* **20** (18),3521-3527, 2008.
2. Matsumoto.Y, et.al Room temperature ferromagnetism in transparent transition metal-doped titanium dioxide, *Sci.* **291**(5505),854-856, 2001.
3. Santara,B., et.al Evidence of oxygen vacancy induced room temperature ferromagnetism in solvothermally synthesized undoped TiO_2 nanoribbons, *Nanoscale* **5** (12), 5476-5488, 2013.
4. Choi, W, et.al The role of Metal Ion Dopants in Quantum-Sized TiO_2: Correlation between Photoreactivity and Charge Carrier Recombination Dynamics, *J.Phys.Chem* **98** (51), 13669-13679, 1994.
5. Gracia, F., et.al. Structural, Optical and Photoelectrochemical Properties of M^{n+} TiO_2 model thin film Photocatalysts, *J.Phys.Chem.B* **108** (44), 17466-17476, 2004.
6. Wen,L., et.al Synthesis, Characterisation and Photocatalysis of Fe doped TiO_2 : A combined Experimental and Theoretical study, *Int.J.Photoenergy* **2012**, 368750, 2012.
7. Li,F.B., et.al Photocatalytic degradation of 2-mercaptobenzothiazole in aqueous La^{3+}- TiO_2 suspension for odor control, *Appl. Catal B* **48** (3),185-194,2004.
8. Zalas,M and Laniecki.M. Photocatalytic hydrogen generation over Lanthanides doped titania, *Sol.Energy.Mater.Sol.Cells* **89** (2-3), 287-296, 2005.

9. Devi,L.G., et.al. Photocatalytic degradation of Imidachloprid Under solar light Using Metal Ion Doped TiO_2 Nanoparticles: Influence of Oxidation States and Electronic Configuration of Dopants, *Catal.Lett* **130** (3-4), 490-503, 2009.
10. Choi,J., et.al. Three-dimensional Gd doped TiO_2 fibrous photoelectrodes for efficient visible-light driven photocatalytic performance, *Rsc.Adv* **4** (23), 11750-11757, 2014.
11. Lei, S and Duan,W. Highly active mixed phase TiO_2 photocatalysts fabricated at low temperature and the correlation between the phase composition and photocatalytic activity, *J.Environ.Sci* **20** (10), 1263-1267, 2008.
12. Bhaumik. S., et.al. Optical and Magnetic properties of Er doped SnO_2 nanoparticles, *Phys. Status. Solidi* **210** (10), 2146-2152, 2013.

DECLARATION

I hereby declare that the thesis entitled "**Studies on the effect of defects and dopants on the optical, photocatalytic and magnetic properties of TiO_2 nanoparticles**" being submitted to Tezpur University, Tezpur, Assam in partial fulfillment of requirements for the award of the Degree of Doctor of Philosophy is a record of research work done by me during the Ph.D course. Ant text, figures, theories that are not of own framed are properly referenced in order to acknowledge the original authors(s). This work has not been submitted in part or full for the award of any degree, diploma, fellowship or any other similar title or recognition from any other institute or organization.

Date: 13/11/2019

Susmita Paul.

(Susmita Paul)
Department of Physics
Tezpur University.
Tezpur-784028 (Assam)

Tezpur University

CERTIFICATE

This is to certify that the thesis entitled "**Studies on the effect of defects and dopants on the optical, photocatalytic and magnetic properties of TiO_2 nanoparticles**" submitted to the School of **Science** Tezpur University in partial fulfillment for the award of the Degree of Philosophy (Ph.D.) in **Physics** is a record of research work carried out by **Miss. Susmita Paul** under my supervision and guidance.

All help received by her from various sources have been duly acknowledged.

No part of this thesis has been reproduced elsewhere for award of any other degree.

Date: 13.11.2014

Place: TEZPUR

Prof.Amarjyoti Choudhury

(Professor)

School of Science.

Department of Physics.

TABLE OF CONTENTS

Chapter 3

Monitoring the optical and photocatalytic properties of mixed phase TiO_2 nanoparticles.

Chapter 4

Exploring the optical, photocatalytic and magnetic property of Ni^{2+} doped TiO_2 nanoparticles.

Chapter 5

Effect of Manganese doping in tailoring Optical and Photocatalytic properties of TiO_2 nanoparticles and the role of oxygen vacancies in paramagnetic to ferromagnetic transition.

Chapter 6

Investigation of the changes in the various properties of TiO_2 nanoparticles by gadolinium doping.

Chapter 7

Extending photocatalytic activity of TiO_2 nanoparticles to visible region of illumination and the study of magnetic property of Er doped TiO_2 nanoparticles.

Chapter 8

Concluding remarks and future directions

LIST OF TABLES

LIST OF FIGURES

List of abbreviations

DOS	Density of states.
DFT	Density functional theory.
CB	Conduction band.
VB	Valence band.
LDA	Local density approximation.
GGA	Generalized gradient approximation.
PAW	Projected augmented wave.
VASP	Vienna Ab-initio software package..
DMS	Diluted magnetic semiconductor.
BMP	Bound magnetic polaron.
RRKY	Ruderman-Kittel-Kasuya-Yosida.
DSSC	Dye sensitized solar cell.
FET	Field effect transistor.
XRD	X-ray diffraction technique.
TEM	Transmission electron microscope.
EDX	Energy dispersive X-ray analysis.
XPS	X-ray photoelectron spectroscopy.
K-M	Kubelka Munk plot.
TRPL	Time resolved photoluminescence spectra.
DRS	Diffuse reflectance spectra.
ZFC	Zero field cooling.
FC	Field cooling.
CW	Curie Weiss.
BGR	Band gap renormalization.

List of symbols.

d	d spacing.
eV	electron volt.
π	pi.
T	temperature.
K	Kelvin.
λ	wavelength.
$\mathring{A}$	angstorm.
nm	nanometer.
Oe	Oerested.
θ	diffraction angle.
β	Full width at half maximum.
k	force constant.
m*	effective mass of electron.
ε	Dielectric constant.
α_B	Exciton Bohr radius.

ACKNOWLEDGEMENT

It gives me immense pleasure to express my deep sense of gratitude to those who have helped me directly or indirectly in accomplishing my research work and without whom the thesis would not have been possible.

At the outset, I would like to thank my research supervisor Prof Amarjyoti Choudhury for offering constant help and guidance through out my research work at Tezpur University. His valuable suggestions and criticism have inspired me to put my sincere efforts into my work. I shall be highly obliged to him for all my life for being there with words of encouragement, wisdom and positivism.

I am also grateful to Dr Gazi Ameen Ahmed , Dept of Physics, Tezpur University for extending his kind co-operation from time to time during my PhD work.

I would also like to acknowledge Dr. Dambarudhar Mohanta , Prof. Nidhi Saxena Bhattacharya, Prof. Jayanta K. Sharma for their encourgament, criticism and inspiration to carry out my work.

It has been a wonderful experience to spent some very special and memorable moments of my life with some wonderful labmates Biswa da, Bondita ba, Priyanka , Pawan. I will always remember the fruitful working environment, the beneficial discussion and of course the joyous moment we spent together both inside and outside the lab.

I would like to acknowledge UGC for financial support to the project F.No.42-785/2013 (SR). In this context I would like to take the opportunity to thank Sophisticated Analytical Instrument Facility (SAIF), NEHU, Shillong for helping me in providing the HRTEM images, IIT Kanpur for providing the magnetic measurement results. Special thanks to Shreedhar Bojja, IICT Hyderabad in carrying out the XPS analysis of my samples. I also thank Biju, Mrinmoy (Dept of Physics) for helping me with UV-Vis , PL measurements, Prakash Da (SAIC , Tezpur University) for carrying out the XRD analysis, Jayanta Da (Dept of Env.sci) for taking the ICP measurements of my samples. Sincere thanks to all the faculty members, Dept of Physics, Tezpur University.

I am fortunate enough to have some good friends and seniors around me: Mansi, Kakoli, Kashmiri, Nibedita, Manjit, Babu, Upamanyu Da

Last but not the least I thank my parents from the deepest core of my heart. They have always been so supportive to walk extra miles and talk all the pains to help me overcome of my frustrations during the course of my PhD work. Thank you so much Ma and Baba for all your blessings. I sincerely acknowledge all my uncles and aunts for their constant support and encouragement. I also extend my unfeigned thanks to my dear cousins Riya, Rima, Tupa, Papai, Mamon. At the end I thank the Almighty for giving me moral strength to carry out my PhD work.

Date Susmita Paul

CHAPTER 1

Introduction

1.1. Nanomaterials

Nanoscience and Nanotechonology is an umbrella term encompassing a range of varied research area used to indicate the study of novel properties of 1-100 nm size and their wide range of applications. Nanoscience is the investigation of properties of materials with structural features in the nanometer range. The underlying theme of nanotechnology is miniaturization and wide range of properties of nanomaterials. The development of advanced tools for characterizing these nanomaterials has provided scientists with new insights for understanding and developing new devices and clues to design new nanostructured materials for a sustainable usage of raw materials and energy.

Nanomaterials exhibit a number of special properties relative to bulk counterpart. Size affects constitute a fascinating aspect of nanomaterials. Due to small size and a large surface to volume ratio nanoparticles exhibit interesting novel properties. Their fine grain dimensions, significant volume fractions of atoms located at the grain boundaries confer them special attributes [1]. Classical laws of physics fails to explain the origin of these novel properties in this nanoregime [2]. From the elementary quantum mechanics it is known that when the electronic particles or charge carriers are confined in a volume limited by potential barriers that are comparable or smaller than the de Broglie wavelength of the particle , the allowed energy becomes discrete rather than continuous as in bulk materials. This effect of size or spatial confinement is termed as size quantization or quantum confinement. Electrons in the nanoregime experience a confinement in space. Dimensional confinement of electrons in materials leads to the modification of the density of states (DOS) giving rise to shape dependent properties. Based on the dimensional confinement of electrons nanomaterials are generally classified as 2D, 1D, 3D [3]. In 1D the confinement of electrons is imposed only along one axis (eg quantum well). In case of 2D electrons are confined only in two directions but are free to move only in one directions (eg nanowires, nanotubes). Howevern in

3D electron experiences confinement in all the three dimensions (eg nanoparticles) [3]. Due to the quantum confinement effect the structural, optical, electrical and magnetic behavior of the nanoparticles are found to be totally different from their bulk counterparts.

The properties of bulk semiconductors are dependent on the energy gap between its valence band and conduction band. Transition from bulk to nanoregime results in discreteness and the density of states ceases to be continuous. As a result electrons occupy specific number of well separated states at a given energy [4]. The absorption of energy excites electrons from valence band to the conduction band leaving behind holes in the valence band. At low temperatures these two charge carriers form a weak coupled pair called exciton [5]. The excitons correspond to a hydrogen like bound state of an electron-hole pair and characterized by exciton Bohr radius defined by [6].

$$\alpha_B = \frac{4\pi\varepsilon_o\varepsilon_r\hbar^2}{m_o e^2}\left(\frac{1}{m_e^*} - \frac{1}{m_h^*}\right) \quad \text{---------- (1.1)}$$

where, ε_r = relative dielectric constant

m_e^* = effective mass of electron

m_h^* = effective mass of hole

m_o = rest mass of electron.

For most of the semiconductors the exciton Bohr radius is within the range of 1-10 nm. The exciton radius is an important parameter to explain the quantum confinement effect. The effect of quantum confinement on the electronic states was theoretically investigated by Efros and Efros. According to Schmitt-Rink et.al [7] the optical properties show dramatic enhancement when the size is smaller than the excitonic Bohr radius. This is based on the observation that as the dimensionality of the bulk semiconductor is reduced, the density of states becomes intense in narrowing energy bands and ultimately results in discrete energy states [7].The energy separation between the discrete levels in the semiconductor nanostructures varies inversely to the size of the material [8]. The blue shift in the optical absorption spectra is noticed due to an increase in the band gap of the semiconductor nanostructures.

Semiconductors nanostructured materials have been studied intensely in the

last several years using various physical and chemical methods. Nanosized semiconductors exhibit special thermodynamic, magnetic, photochemical, photo-physical, and electro-physical properties. When semiconductors are in the nanoscale regime, their size has significant effects on their properties. Tuning the size of such semiconductor nanoparticles opens up the prospect to control their characteristics [9]. The size of the nanoparticle strongly effects the semiconductor light wave communication and the resulting processes. These processes depend on the optical absorption of light, dynamics of photogenerated exciton, the consequences of electron-hole recombination, and the photo-chemical reactions in the presence of reagents adsorbed on the semiconductor surface [10]. The size effects in the nanoparticles are classified into two types. The first one is the increased surface to volume ratio and the other is the alteration in the electronic state of the semiconductor due to quantum size effects dominating below a critical size of ~10 nm at room temperature. The critical size which is the threshold for the quantum size effects varies for different semiconductors depending on the chemical structure of the nanoparticle. It is similar to de -Broglie wavelength of free electron [11]. Among the various semiconductor nanocrystalline TiO_2 is one of the most widely studied oxide semiconductor. This chapter is focused on the fundamental properties of TiO_2. Generally pure TiO_2 suffers from problems of large band gap. This drawback limits its application as an efficient photocatalyst under visible light. The fundamental processes involved in photocatalysis as well as the state of the art for pristine and doped TiO_2 is also highlighted in this chapter. The dopant induced changes on the optical and magnetic property has also been focused. Because of the lack of detailed information about the effects of metal doping on crystal structures and electronic structures, there is still much dispute. Theoretical analysis by using Density Functional Theory (DFT) has been discussed to clarify the effects of doping in detail.

1.2. Crystal Structure of TiO_2

TiO_2 belongs to the family of transition metal oxides. There are three commonly known polymorphs of TiO_2 found in nature: anatase (tetragonal), brookite (orthorhombic), rutile (tetragonal) [12]. The three different crystal structure can be described in terms of the chains of octahedra. Each Ti^{4+} ion is surrounded by an octahedron of six O^{2-} ions. Anatase is built up from octahedrals that are interconnected by their vertices whereas in

rutile the edges are connected [13]. Anatase TiO_2 consists of arrangement of parallel octahedron, while in the rutile phase some octahedron are distorted by 90°. The brookite phase of TiO_2 is a bit complicated and is not often used for experimental investigation [14] . In this phase both edges and vertices are connected [12]. Fig.1.1 shows the crystal structure of the different forms of TiO_2.

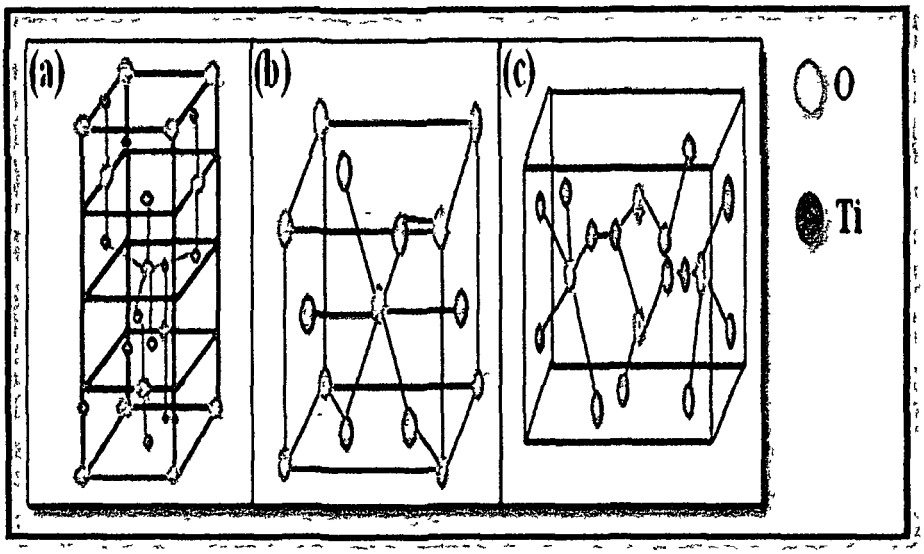

Fig.1.1. Crystal structure of (a) anatase (b) rutile (c) brookite

The valence band of TiO_2 is composed of the 2*p* orbitals of oxygen hybridized with the 3*d* orbitals of titanium while the conduction band is composed of only 3*d* orbitals of titanium [15]. In comparison to rutile phase , anatase form of TiO_2 has inherent surface band bending that forms spontaneously in a deeper region with a steeper potential [12]. Surface hole trapping dominates and spatial charge separation is obtained by the transfer of photogenerated holes towards the surface of particle via the strong upward band bending [12]. In the rutile phase the bulk recombination of electron and hole takes place due to which holes very close to the surface are trapped and transferred to the surface [15]. The difference in the bonding arrangement and structure leads to difference in their practical applications, eg anatase is used as good photocatalytic candidate whereas rutile is used as pigments due to effective light scattering [12].

1.3. Process of Phase transformation

Temperature has a profound effect on the anatase to rutile phase transformation. There

occurs both phase conversion as well as microstructural modification on annealing at high temperature. A noteworthy feature is that in bulk TiO_2 rutile is stable while anatase is metastable [16,17].The brookite phase of TiO_2 transforms into rutile phase with anatase as an intermediate [18,19]. The polymorphic transformation is however quite complex. In nanocrystalline TiO_2 the competition between surface energy and the energetic of the polymorphs stabilizes the anatase at smaller particle size and thereby results in a crossover in thermodynamic stability between anatase and rutile phases [18, 20].Upon heating nanocrystalline TiO_2 dehydrate and coarsen as they change from anatase to rutile phase. The transformation from anatase to rutile phase is often followed by contemporaneous presence of a mixed phase that is coexistence of both pure anatase and pure rutile phase. Studies have shown that mixture of both these phases can contribute to enhanced photocatalytic activity [19].

1.4. TiO_2 as a photocatalyst.

Photocatalytic mechanisms usually involves light and a catalytically active species [21]. A substance can be taken as a catalyst if it accelerates a chemical reaction without itself undergoing any changes. When light of sufficient energy illuminates the photocatalyst an electron from the valence band is promoted to the conduction band, leaving an electron deficiency or hole (h^+) in the valence band and an excess of negative charge in the conduction band (e^-).These conduction band electrons and valence band holes undergo redox reactions known as interfacial charge transfer. Overall a photocatalytic reactions may be summarized as follows [22].

$$(Ox_1)_{ads} + (Red_1)_{ads} \xrightarrow{\text{photocatalyst+hv}} (Ox_2)_{ads} + (Red_2)_{ads}$$

In practice the photocatalytic process progress through the presence of aqueous environment. In case of TiO_2 the photocatalytic reactions are composed of the following steps [22]:

a). Activation of the photon energy greater than its band gap (3.2 eV) that generates electron-hole pair:

$$TiO_2 \xrightarrow{h\nu \geq 3.2eV} e^- + h^+$$

This is a very important step. The efficiency of the photocatalyst is dependent on the wavelength and intensity of illumination source.

b). Adsorption of the compound to be oxidized on the catalyst surface and the lattice oxygen (O_L^{2-}).

c). Recombination of the photogenerated charge carriers to produce heat.

$$e^- + h^+ \rightarrow \text{heat}$$

This is the most dominant step. More than 95% of the charge carriers recombine before taking part in a chemical reaction. The recombination takes place either on the bulk or on the surface and the kinetics of the processes determine the efficiency of a photocatalyst.

d). Trapping of the charge carriers on the photocatalyst surface. The charge carrier recombination and trapping determine the overall quantum efficiency of a photocatalyst.

e). Oxidation of the adsorbed compounds. This step is assisted by holes on the surface or by the attack of the hydroxyl radicals generated by photocatalysis.

But being a wide band gap semiconductor TiO_2 can utilize only a limited portion of the solar spectrum. This lowers the utilization of the material for practical applications. Extending the absorption of the material to the visible region requires changes in the underlying electronic structure that is closely interrelated to the chemical composition and related atomic arrangements. Doping is an indispensable way to produce favorable changes in the electronic structure while keeping the integrity of the original crystal structure. Reducing the size of the band gap through introduction of energy levels between the valence band and conduction band makes TiO_2 to be active under visible light [21].

1.5. Tuning of optical properties of TiO_2 by doping.

Investigation of the optical property of the nanomaterial is a very powerful tool to understand the electronic properties of the materials as the energy dependence of the optical properties is related to the band structure. When light of sufficient energy falls on a material, it induces electronic transition from occupied states below Fermi level to

the unoccupied state above Fermi level. The quantitative study of these transitions provides some understanding of the initial and final energy bands and symmetry of the associated wave functions. There are two main types of band gap transition in semiconductors [23]. For direct band gap semiconductors, electronic transition from the valence band to the conduction band is electrically dipole allowed [23] and the electronic absorption as well as emission is usually strong. For indirect band gap semiconductors the electronic transition from the valence band to the conduction band is electrical dipole forbidden and the transition is phonon assisted implying that the energy and momentum of the electron-hole pair are changed in the transition [23]. Anatase and rutile TiO_2 is reported to exhibit both direct and indirect band gap, but the indirect band gap transition is preferred over the direct one owing to the fact that the low strength direct transition is forbidden [24,25]. In anatase and rutile TiO_2 the indirect allowed transition occurs due to $M \rightarrow \Gamma$ transition from O $2p$ to Ti $3d$ level in the Brillouin zone [25,26].

Doping of TiO_2 is an important approach in the band gap engineering to change the optical response of the material [12]. Doping involves incorporation of foreign atom into the catalyst matrix of the parent metal oxide. From chemical point of view doping is equivalent to the introduction of defect like Ti^{3+} into the semiconductor lattice. In a bulk crystalline material translational symmetry leads to the formation of electronic energy bands. Introduction of the dopant ions breaks the periodicity of the lattice and perturbs the band structure. The perturbation is actually categorized by the presence of discrete energy levels within the band gap. The introduction of such energy levels in the band gap introduce a red shift in the band gap transition and visible light absorption through a charge transfer between the dopant ion and conduction band or valence band in the crystal field, in turn satisfying the criteria for enhanced photocatalytic activity.

Das.et.al [27] reported band gap reduction in Co doped TiO_2 nanoparticles to the exchange interaction between dopant d electron and host sp electrons. Li.et.al [28] in their work on Nd^{3+} doped TiO_2 nanoparticles attributed band gap reduction to the formation of electronic states of the Nd^{3+} dopant ion in the host matrix. For efficient photocatalytic process it is worth mentioning that the dopant ion must act as both electron and hole traps. Trapping of either electron or hole is however ineffective as the immobilized charge species rapidly recombines with the movable counterparts. The

recombination process competes with the charge transfer process to absorb species in the volume of the semiconductor particle or on its surface followed by the release of heat. The process in turn adversely effect the photocatalytic mechanism and decrease the overall photocatalytic efficiency.

Another very interesting optical property is the band gap widening due to doping the semiconductor to a high free carrier concentration [29]. Mei.et.al [30] in their work reported that the band gap of TiO_2 is increased after Nd doping. They attributed this behavior to Burstein Moss effect [31]. According to this effect when the electron concentration is high enough, the Fermi level of the system passes through the conduction band and there are considerable conduction carriers at the bottom of the conduction band. The electrons in the valence band are excited to above the Fermi level instead of to the bottom of the conduction band that are occupied by the conduction electrons. This results in widening of the band gap of the doped degenerate semiconductors compared to the undoped one. The dopant localized states spread out the band edges producing absorption tail deep in the forbidden gap. The strength of the band tail is characterized by Urbach energy which is an important tool to investigate the perfection of the lattice [32,33]. A schematic of the formation of Urbach energy is shown below, Fig.1.2. The dopant atoms substitute the atomic sites and therefore Urbach tail consists of a mixed signal from lattice distortion and impurity band. The equation for Urbach energy is given by:

$$\alpha = \alpha_o \exp \frac{E}{E_u} \quad \text{---------- (1.2).}$$

Where α is the absorption coefficient, E is the photon energy and E_u is the Urbach energy [34]. The reciprocal of the slopes of the linear portion below the band gap gives the Urbach energy. The Urbach energy is therefore very important to understand the disorder in a material. The higher the Urbach energy the greater is the disorder in the material [35].

Although the effects of metal ion doped TiO_2 is investigated frequently, but it remains difficult to make undeviating assessment and potray a clear conclusions due to diverse experimental environment and different methods for sample preparation and photoreactivity testing. Doping of TiO_2 is an essential way to produce constructive changes in the electronic structure while keeping the veracity of the original crystal

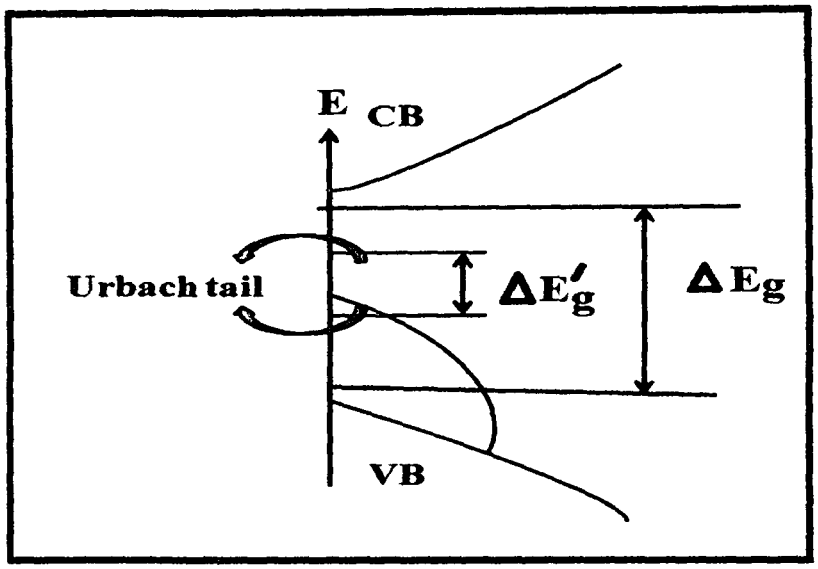

Fig.1.2: Schematic of Urbach tail formation. $\Delta E_u = \Delta E_g - \Delta E_g'$

structure. Often in nanotechnology the motivation is on providing solutions to real world technological problems. The construction and characterization of the systems that demonstrate the potential for use is often an end goal. Nanotechnology greatly benefits from theoretical inputs. Firstly it is quite impractical to perform experiments quite a large number of times. Secondly experimental results cannot always be straight forwardly interpreted and therefore theoretical analysis is significant to elucidate the vital physics behind the situation and resolve many ambiguities. The behavior of the nannoscale systems is governed according to the Schrodinger equation. With the help of this equation small systems like hydrogen atom can be computed. Approximate methods are therefore needed to acquire information about many atom systems such as molecules or surfaces. With the development in the computational techniques, theoretical investigations of quantum mechanical system has highly risen. Many algorithms have been developed that allow the complicated equations governing quantum mechanical behavior to be answered approximately. Computational physics is a very important tool to provide elucidation and way for continuing and impending future experiment. Density functional theory (DFT) is an exceptionally valuable method to analyze and throw light on doping process and its effect on the electronic structure. Thanks to the spectacularly increased processing powers and more efficient software codes that implements comparable computational techniques performing such calculation very

smoothly compared to the scenario just a decade ago. Yu.et.al [36] with the help of DFT calculation confirmed the red shift of absorption edges and the narrowing of the band gap of Fe doped TiO_2 nanorods. Guo and Du [37] reported that addition of copper atom can lead to the enhancement of *d* states near the upper most part of the valence band of TiO_2 and the Ag or Au doping creates some new energy states in the band gap.

1.6. Density Functional Theory (DFT).

Density functional theory (DFT) is an *ab-initio* method used to know the ground state of the atoms, molecules and solids. Solution of many electron Schrodinger equation by traditional wave function presents a difficult task as the wave function is a function of 3N spatial coordinates and N spin coordinates, N being the number of electrons in the system. Once the electron density is known the external potential and consequently the Hamiltonian of the system can in principle be uniquely determined.

Density functional theory (DFT) states that all ground state properties are functionals of charge density ρ in which the total energy is given by:

$$E[\rho]=T[\rho]+U[\rho]+E_{XC}[\rho] \quad \text{----------} \quad (1.3)$$

Where $T[\rho]$ - kinetic energy, $U[\rho]$ - classical electrostatic energy and $E_{XC}[\rho]$-energy due to many body contributions.

The first term represents electron-nucleus attraction. The second term represent the electron-electron repulsion where as the third term corresponds to the nucleus-nucleus interaction. Optimisation of the total energy with respect to variation in ρ leads to set of coupled equations known as Kohn-Sham equations. Density functional theory reduces quantum mechanical ground state many electrons to self consistent one electron form through the Kohn-Sham equation [38-39]. This is a very useful approach for the elaboration of the ground state properties of metals, semiconductors and insulators. Kohn and Sham [39] formulated mapping of the interacting many body electron system onto a system of non interacting electrons moving in an effective potential due to all other electrons and ions. Basically in density functional theory we have to find a self-consistent solution of Kohn-Sham equation that leads to the ground state density. In practice in order to calculate the band structure of a solid, the Kohn-Sham orbital $\psi_i(r)$ are usually expanded in terms of some chosen basis functions with some

co-efficients that are to be determined variationally. The choice of the basis set leads to the nearly correct solution of the one electron band structure problem.
The one electron energy Kohn Sham equation is given by:

$$\left[-\nabla^2 + V_{eff}(r)\right]\Psi_i = \varepsilon_i \Psi_i(r) \quad \text{---------- (1.4)}$$

The accurate form of exchange correlation is unfortunately not known. So it is very necessary to introduce some approximation and the most successful and well tested is so called the local density approximation (LDA) [38] and Generalized Gradient Approximation (GGA). In constructing LDA functionals it is assumed that the density is homogeneous and the total exchange-correlation energy is found by integrating the corresponding exchange correlation energies.

The Generalized Gradient Approximation (GGA) is used widely to provide the accuracy required for density functional theory to be used in various types of analysis. In GGA the exchange correlation energy depends not only on the electron density ρ(r) at a particular point but also on the gradient of the charge density $\nabla\rho(r)$. The GGA tends to improve the accuracy of DFT calculations somewhat.

1.6.1. Pseudopotentials.

It is a very well known fact that the physical properties of solids are dependent on the valence electrons to a much greater than core electrons. The pseudopotential exploits this by removing the core electrons that are highly localized and by replacing the strong ionic potential by a weaker pseudo potential that acts as a set of pseudo function rather than true valence wave functions. The physical reason behind the pseudo potential is very simple , the core electrons wave functions of an atom remains unchanged inspite of placing into different chemical environment, the true atomic potential can be replaced by pseudo potentials that effectively reproduces the effect of core electrons. The combination of pseudo potential and plane wave is very important for the electronic structure calculations.

1.6.2. Projected Augmented Wave.

The projected augmented wave is computationally very efficient technique used in *ab-initio* electronic structure calculations. In this method an augmentation sphere is

included surrounding each nucleus in the lattice and outside this augmentation sphere the wave functions are represented with smooth normal plane waves. Within the augmentation sphere the wave functions are presented with projectors and auxillary localize wave functions just in case of ultrasoft pseudopotentials. In PAW all electron wave function can be preserved. The full wave functions oscillates heavily around the nucleus, hence all integrals in the PAW method are evaluated as combination of integral smooth functions outside the augmentation spheres plus contribution from radial integration over augmentation spheres.

1.6.3. Plane Wave basis set

Density Functional theory thus provides a remarkably accurate method of simulating materials quantum mechanically. Due to the cost effective factor , it has paved the way to understand a plethora of materials which would have otherwise been out of reach of quantum mechanical simulations.

In a real DFT calculations convergence criteria must be obtained with respect to the number of k-points. It is usual to converge the wave functions in terms of a plane wave energy cut off that determine the number of plane waves. The number of plane wave require increases with the fine quality of the features of the wave functions. The core wave functions of the atoms tends to oscillate rapidly and so they are unsuitable to contribute to the expansion with plane waves. As the core electrons donot participate in contributing to the physical properties of the solids they are typically removed. The core electrons screen the nuclear potential and to recompense for their non appearance pseudopotentials are used [40,41]. In Density functional theory, by comparing the total energies of different atomic configurations the most energetically favored structure is calculated. The allowed energy states are relaxed to lowest energy configuration and the interatomic forces are calculated from the variation in total energy. Another important feature is the spin polarization calculation used in DFT. The DFT calculations done in the thesis uses Vienna Ab-initio Software Package (VASP). The package performs *ab-initio* quantum mechanical molecular dynamics using pseudopotential and a plane wave basis set. Both LDA/GGA functionals are available. VASP always needs minimum four files:

- INCAR: that contains all settings of the programme parameters that we

wish to use.

- KPOINTS: contains all information regarding the k-point set.
- POSCAR: contains information regarding the geometry of our system.
- POTCAR: the information regarding the potentials functionals are contained in this file.

Due to the variation in electronic band structure a wide range of optical and electronic properties are observed in solid state materials. The atoms in a solid state materials are closely spaced together with the interatomic separation distance to form solid, the outer orbitals of the atom overlap and interact strongly with each other as a result of which electronic bands are formed [42]. The electronic states of a solid are determined by density of solids (DOS). In VASP spin polarization is not considered by default it has to be turned on for systems that contains magnetic spin. The spin polarised structure are found to be more stable than spin unpolarised. The concept of the density of states sprouts from the concept electronic band formation in solids. The density of states is defined as the number of electronic states or unit energy within a given interval.

The density of states function D (ε) may be written in the form:

$$D(\varepsilon)=\sum_{i}\delta(\varepsilon-\varepsilon_{i}) \quad \text{---------- (1.5)}$$

Calculation of the Density of States using VASP requires a fairly dense mesh of k-points in the Brillouin zone. A decomposition of the local states into state-resolved density of states gives the projected density of states (PDOS). The density of state analysis gives an idea of the trap states generated due to dopant incorporation [43].

In this thesis optical properties and photocatalytic activities of some transition and rare earth metal doped TiO_2 nanoparticles have been explored. Theoretical study based on DFT are carried out to identify the states generated due to doping.

1.7. Diluted Magnetic Semiconductors.

Dilute magnetic semiconductors have been the forefront of research due to their possible applications in nanomagnetics and spintronics for information storage, transport and processing. In DMS some fractions of atoms in a non-magnetic semi-conductor is replaced by magnetic ions (Fig.1.3).

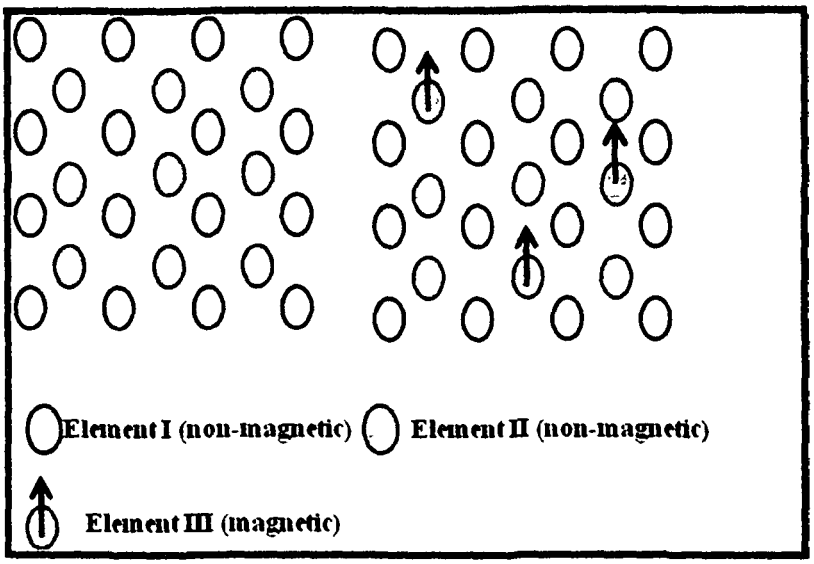

Fig.1.3: Schematic representation of a non-magnetic semiconductor (left) and a diluted magnetic semiconductor (right).

The emerging research area known as spintronics seeks to explore the properties and applications of established electronic devices by making use of spin of electrons in addition to their charge [44]. A different number of semiconductor oxides have been investigated to test the magnetic nature. Initially ferromagnetism has been reported for GaAs doped with Mn^{2+} ions or InAs doped with Mn^{2+} ions [45]. However they are disqualified for practical applications due to their high Curie temperature that was around 170 K and 35 K for (Ga, Mn)As and (In, Mn)As respectively [45,46]. Since than there has been a large incentive for developing new DMS materials that are ferromagnetic above room temperature. Matsumoto and his group was the first to successfully obtain room temperature ferromagnetism in Cobalt doped doped TiO_2 nanoparticles [47]. Although there are reports on the observation of ferromagnetism above room temperature, however the origin of magnetism in such systems is not fully understood. The magnetic properties of doped TiO_2 are strongly sensitive to preparation condition, morphology and presence of defects.

Bhattacharya *et al* [48]. synthesized Mn doped TiO_2 nanoparticles by one pot RAPET technique (reaction under autogenic pressure at elevated temperature) and

reported ferromagnetic behavior upto 1%. However, with the increase in dopant concentration upto 5 and 7 % the system showed paramagnetic behavior. Peng et al [49] observed ferromagnetism in Mn doped TiO_2 nanoparticles prepared by a simple sol-gel method. Sellers and Seebauer reported room temperature ferromagnetism in Mn doped TiO_2 nanopillars prepared by atomic layer deposition method [50].Thus, synthesis condition and morphology has a profound effect in modulating the magnetic property in TiO_2.

Presence of defects and annealing condition is also reported to affect the magnetism. Choudhury et.al [51] observed paramagnetism in air annealed Co doped TiO_2 nanoparticles while the same material exhibited ferromagnetism on calcination under vacuum. This contrasting nature of the magnetic property in the same system under two different annealing atmosphere is attributed to the formation of high density of oxygen defects under vacuum annealing [51].

Recently rare-earth doped DMS have caught up great interests because of their unique fluorescence properties and due to the high emission quantum yields. In transition metal magnetic moment arises from partially filled outermost $3d$ electrons, whereas in rare earth ions magnetic moment arises from the inner $4f$ incomplete sub-shell. Theoretical analysis have been carried out to explain the ferromagnetism in Gd doped GaN [52,53]. Dalpian and Wei reported that the direct coupling between the Gd atoms was antiferromagnetic in nature in Gd doped GaN [52]. The ferromagnetic phase was stabilized by the electrons due to the mixing of Gd f with host s states.

Thus it is surmised that introducing transition or rare earth ions in TiO_2 lattice result in partially filled d or f electron shells with unpaired electrons that couples ferro-magnetically or anti ferromagnetically. Apart from the doped systems ferromagnetism has also been observed in oxide systems without adding impurities. Coey et al. [54] observed ferromagnetism in HfO_2 without adding impurity. They corroborated the observed magnetism to the presence of oxygen vacancies. Elfimov et al. [55, 56] demonstrated that Ca vacancies in CaO produce local magnetic moments and transform the non magnetic to half metallic ferromagnet .These discoveries introduce a new path to study ferromagnetism in undoped TiO_2. Hong et al. [57] and Yoon et al. [58] reported magnetism in TiO_2 thin films. They attributed these magnetism to the presence of oxygen vacancies that acts as n-type dopant.

1.8. Theoretical models for explaining ferromagnetism in DMS.

Two main theories are used for explaining ferromagnetism in oxide DMS- RRKY (Ruderman-Kittel-Kasuya-Yosida) interaction and Bound magnetic polaron (BMP) [59,60]. The RRKY model describes the magnetic interaction between a single localized magnetic ion and the delocalised conduction band electrons. As a result of this interaction the conduction electrons very close to the magnetic ion is magnetized and act as an effective field to induce polarization in the nearby magnetic ions with the polarization decaying in an oscillatory manner [61]. The oscillation mediates through either ferromagnetic or antiferromagnetic exchange coupling depending upon the separation between the magnetic ions.

The theory of bound magnetic polaron was given by Coey and his workers and is suitable for insulating systems where electrons are strongly localized [59]. In this model an electron trapped in an oxygen vacancy (F centre) forms hydrogenic orbitals with radius $r_H = \varepsilon(\frac{m}{m^*})a_B$, where ε is the dielectric constant, m is the electron mass , m* is the effective mass of the donor electron and a_B is the Bohr radius. Formation of bound magnetic polaron is schematically shown in Fig.1.4.

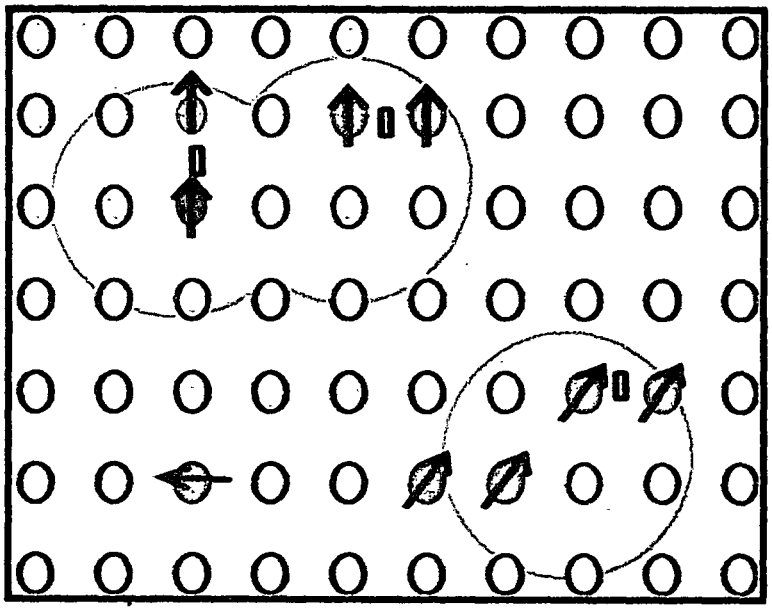

Fig.1.4: Schematic of bound mangnetic polaron. The cations are represented by small circles, the unoccupied oxygen vacancies are represented by small circles.

A Bound Magnetic Polaron is formed when the spin of the trapped electron couples effectively with the magnetic impurities within the hydrogenic radius. The oxygen defects in the BMP are responsible for the shallow donors and strongly stabilize the ferromagnetic state. When the neighboring polarons donot interact strongly a paramagnetic phase results. It is difficult to make any quantitative prediction about the distances, but the critical distance above which the exchange between two BMPs becomes ferromagnetic is typically of the order of a few Bohr radii [62, 63].

1.9. Applications of undoped and doped TiO_2 nanoparticles

TiO_2 is close to being an ideal photocatalyst and benchmark for photocatalysis activity. The single drawback is that it doesnot abosrb visible light. The photocatalytic performance of pure TiO_2 can be enhanced by creating defects in the band gap of TiO_2. Oxygen deficient TiO_2 has been reported to have enhanced visible light activity [64,65]. Apart from photocatalysis other most important application of TiO_2 is in dye sensitized solar cells. Ito.et.al [66] demonstrated the methodical fabrication of TiO_2 electrodes that showed reproducible conversion efficiencies over 10%. Elsanousi.et. al [67] fabricated highly ordered TiO_2 nanotube array by aniodic oxidation on titanium foils and predicted significant photo-conversion efficiencies may be obtained by the front side illumination of DSSC when the length of the nanotube array is increased to several micrometers [67]. Hwang.et.al [68] prepared DSSCs using four different anatase/rutile mixed phase (AR-3, AR-15, AR-20, and AR-23 denoted for the samples of 3%, 15%,20%, and 23% rutile phase, respectively). They have reported photo conversion efficiency of 5.07% for AR-20. Some other applications of TiO_2 are in cosmetics [69], Li ion batteries [70].

The introduction of dopant ion is known to effect the electronic band edges or introduce impurity states in the band gap of the system. Choi.et.al [71] presented a systematic study of metal ion doping of quantum sized TiO_2 for 21 metal ions and observed that the photoreactivity of TiO_2 is significantly increased in presence of these metal ions. Peng.et.al [72] successfully prepared Chromium doped TiO_2 by sol-gel dip coating process and reported an enhancement in photocatalytic activity under visible light.

Rare earth doped TiO_2 is also reported to show good photocatalytic activity.

Stengl.et.al [73] reported enhanced photocatalytic degradation of orange II dye under UV and Visible light by doping rare earth ions in TiO_2. The increased photocatalytic activity was correlated to the higher adsorption and the 4*f* electronic transition of rare earth ions [73]. Choi.et.al [74] reported visible light driven photocatalytic activity of Gd doped TiO_2 nanoparticles. The high photocatalytic activity was attributed to the retarded recombination induced by the lower energy levels for Gd^{3+} carriers.

Huang.et.al [75] evaluated the performance of DSSC using Zn doped TiO_2 nanoparticles and obtained an efficiency of 7.6% for 0.5 at %. The influence of F concentration in TiO_2 on performance of DSSCs was also investigated [76]. The highest efficiency obtained was about 11.3%. Well crystallized Nb doped TiO_2 nanoparticles prepared by a novel synthetic route has been used as photoanode of dye sensitized solar cells [77]. Some other applications of doped TiO_2 are in Li-ion batteries [78], gas sensing [79].

Spintronic technology in which data is processed based on electron spin rather than charge promises to transfigure the computing industry with smaller, faster and more efficient data storage and processing. Diluted magnetic semiconductor (DMS) is one of the key elements in spintronics. Spintronic technology has already been tested in mass storage components such as hard drives. The first spin based field effect transistor (spin FET) was first proposed by Datta and Das in 1990 [80]. A schematic of Datta-Das Spin FET is illustrated in Fig.1.5. In Datta-Das Spin FET the source and the drain are ferromagnets that act as injector and detector of the electron spin, the drain injects electrons with spin parallel to the transport direction. Lee.et.al [81] reported fabrication of Cobalt doped TiO_2 nanowire and the electric field effect transistor (FET) function of these nanowires.

Future nanotechnology is believed to be very much dependent on nanoscale material and devices. At this computer era spintronic devices finds extensive applications. Modern computers make use of spin valve in order to read and write data on their hard drive. Development of computer technology has been the initial driving force in spintronics. So it is very important to exploit and optimize the interesting properties exhibited by these nanomaterials.

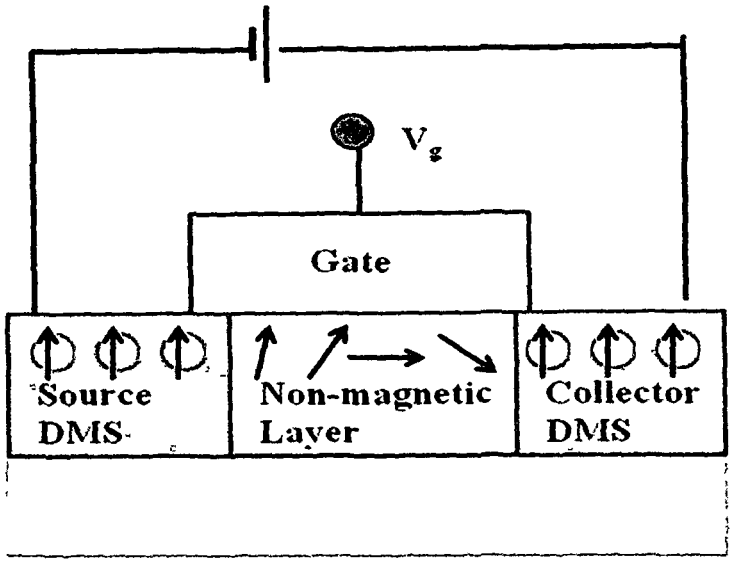

Fig.1.5: Datta-Das spin based field effect transistor using diluted magnet semiconductor.

1.10. Objective of the thesis.

The main objective of the thesis is to study the changes in the optical and magnetic properties of nanocrystalline titania by doping with some transition and rare-earth metal ions. Incorporation of these dopants changes the structural and electronic properties of the host lattice and imparts superior luminescent and magnetic properties. In our work we have chosen Ni and Mn as the transition metal ion dopants and Gd and Er as the rare-earth metal ion dopants. Modification in the structural and morphological property are studied with the help of X-ray Diffraction, Raman, Tem. Investigation of the optical property involves understanding the absorption, emission and carrier recombination behavior of the nanoparticles with the help of UV-Vis, Steady state and time resolved photoluminescence spectra. X-ray Photoelectron spectroscopy are employed to know the oxidation state of the dopant ions and also to understand the presence of oxygen vacancies created by the incorporation of these dopant ions. As doping of these transition and rare earth metal ions create their respective *d* and *f* states within the band gap of the host lattice , so computational techniques involving Density Functional theory is carried out to establish the presence of the *d* and *f* states. Now creation of these states is believed to effect the charge carrier recombination rate and shift the optical

response to the visible region. Both these properties are beneficial for the use of the material as a potential photocatalytic candidate. In our work the feasibility of the photocatalytic degradation of phenol was studied employing visible light.

Furthermore we have also studied the effect of these dopant ions (Mn, Ni, Gd, Er) in tuning the magnetic properties of undoped TiO_2 which is otherwise non-magnetic. In transition metal magnetic moment arises from partially filled outermost $3d$ electrons, whereas in rare earth ions magnetic moment arises from the inner $4f$ incomplete sub-shell. In transition metal ions the strength of the spin-orbital coupling is much smaller than the crystal field energy and hence, the orbital momentum is quenched and only spin moment contributes towards magnetism. In contrast in rare earth ions the $4f$ electrons are shielded by the $5d6s$ electrons and the strength of spin-orbital coupling is much greater than the crystal field energy. These $4f$ electrons undergo indirect exchange interactions via $5d$ or $6s$ conduction electrons and yields high magnetic moment per atoms due to high orbital momentum.

References

1. Rao,C.N.R., Muller.A., & Cheetham., A.K., (ed) *The Chemistry Of Nanomaterials.* Wiley-VCH Verlag GmbH & Co. KGaA, Weinheim, 2004.
2. Kerker,M., The optics of colloidal silver: something old and something new, *J.Colloids and Interface Sci.* **105** (2), 297-314,1985.
3. Alivisatos,A.P., Perspectives on the Physical Chemistry Of Semiconductor Nanocrystals, *J.Phys.Chem* **100** (31), 13226-13239,1996.
4. Roduner. E., Size matters: why nanomaterials are different, *Chem Soc Rev* **35** (7), 583-592, 2006.
5. Geissbuhler, I., *Cadmium Selenide nanocrystals for specific interactions with biomolecules*, PhD thesis, Federal Polytechnique Of Lausanne.at Institute of Science and Engineering campus,Switzerland,2005.
6. Gaponenklo,S.V., *Optical Properties of Semiconductor Nanocrystals*, Cambridge University Press,USA,1998.
7. Rink,S., .et.al. Theory of linear and non-linear optical properties of semiconductor microcrystallites, *Phys, Rev. B.* **35** (15), 8113-8124, 1987.
8. Steiner,T. (ed). *Semiconductor Nanostructures for Optoelectronic Applications*, Artech House, Norwood, 2004.
9. Stroyuk, A. L., et,al. Quantum size effects in semiconductor photocatalysis, *Theor Exp Chem* **41** (4), 207-228,2005.
10. Yanagida, S., et.al. Semiconductor Photocatalysis: Size Control of Surface-Capped CdS Nanocrystllites and the Quantum Size Effect in Their Photocatalysis, *Bull Chem Soc Jpn.***68** (3),752-758,1995.
11. Stroyuk.A.L.et.al. Quantum size effects in photonics of semiconductor nanoparticles, *Theor Exp Chem* **45** (3), 67-91,2002.
12. Gupta.S.M & Tripathi.M. A review of TiO_2 nanoparticles, *Chinese Sci.Bull* **56** (16), 1639-1657,2011.
13. Carp, O., et.al. Photoinduced reactivity of titanium dioxide , *Progress in Solid State Chem* **32** (16), 33-177, 2004.
14. Thompson, T.L and Yates, Jr J.T Surface science study of photoactivation of TiO_2-

New photochemical processes, *Chem.Rev* **106** (10), 2891-2959,107.

15. Winderlich,W., et.al. Electronic properties of nano-porous TiO_2 and ZnO thin films comparison of simulations and experiments, *J.Ceram Process Res* **5**(4),1579-1584,2004.
16. Wang, J., et. al. Size effect on the thermal stability of nanocrystalline anatase TiO_2, *J.Phys.D:Appl.Phys* **46** (25),255303-255313,2013.
17. Arbiol,J., et.al. Effect of Nb doping on the TiO_2 anatase-to-rutile phase transition, *J. Appl. Phys* **99**(2), 6476-6481,2002.
18. Madras,G., et.al. Kinetic Model for TiO_2 Polymorphic Transformation from Anatase to rutile. *J. Am. Ceram. Soc.* **90** (1), 250-277, 2007.
19. Hanaor, D. A.H., et.al Morphology and photocatalytic activity of highly oriented mixed phase titanium dioxide thin films, *Surf and Coat. Technol.* **205** (12), 3658-3664, 2011.
20. Yang, G. J., et.al Effect of annealing treatment on microstructure and photocatalytic performance of nanostructured coatings through flame spraying with liquid feedstocks, *J.Vac.Soc.Technol B* **22** (5), 2364-2368,2003.
21. Bingham, S & Daoud, W. Recent advances in making nano-sized TiO_2 visible light active through rare-earth metal doping, *J. Mater.Chem* **21** (1), 2041-2050,2011.
22. Kurtoglu.M. *Effect of doping on the photocatalytic, electronic and mechanical properties of sol-gel titanium dioxide films.* PhD thesis. Drexel University, Philadhelpia, 2011.
23. Pankove, J.I. *Optical Processes in Semiconductors*, Dover Publications, Newyork, 1971.
24. Tang, H., et.al. Electrical and Optical properties of TiO_2 anatase thin films, *J. Appl. Phys* **75** (4), 2042-2047, 1994.
25. Ho, C.H., et.al Characterisation of direct and indirect interband transition of anatase TiO_2 by thermoreflectance method, *Appl. Phys. Lett* **93** (8), 081904, 2008.
26. Yin,W.J. Effective band gap narrowing of anatase TiO_2 by strain along a soft crystal direction, *Appl. Phys. Lett* **96** (22), 221901,1990.

27. Das, K., et.al. Morphology Dependent Luminescence Property of Co doped TiO_2 Nanoparticles, *J,Phys.Chem.C* **113** (22) ,14783-14792,2009.

28. Li, W., et.al. Band gap tailoring of Nd^{3+} doped TiO_2 nanoparticles, *Appl. Phys. Lett.* **83** (20), 4143-4145, 2003.

29. Gibbs, Z. M., et.al Optical band Gap and Burstein Moss effect in Iodine doped PbTe using diffuse reflectance infrared Fourier Transform Spectroscopy. *New.J.Phys.***15** (7), 075020 , 2013.

30. Mei, B., et.al The synthesis of Nb doped TiO_2 nanoparticles by spray drying: an efficient and scalable method, *J. Mater. Chem.* **21** (32), 11781-11790,2011

31. Burstein.E. Anomalous Optical Absorption Limit in InSb, *Phys.Rev.B* **93** (3), 632-633,1954.

32. Majid.A & Ali.A. Band tailing effects in neon implanted GaN, *J. Appl. Phys* **106** (12), 123528, 2009.

33. Irribaren, A., et.al. Modelling of the disorder contribution to the band-tail parameters in semiconductor materials. *Phys. Rev.B* **60** (7), 4758-4762,199.

34. Zainobidinov, S., et.al. Dependence of the Urbach energy on the Fermi level in A-Si:H films, *Ukr. J. Phys.* **53** (12), 1177-1180, 2008.

35. Tran, T.N., et.al. Optical study of disorder and defects in hydrogenated amorphous silicon carbon alloys, *Appl. Phys .Lett.* **87** (1), 011903 ,2011.

36. Yu,J., et.al. Preparation, characterization and visible light driven photocatalytic activity of Fe doped TiO_2 nanorods and first-principles study for electronic swtructure, *Appl.Catal B environ* **90** (3) , 595-602, 2009.

37. Guo, M & Du,J First-principles study of electronic structures and optical properties of Cu, Ag, and Au doped anatase TiO_2 , *Phys. B-Condensed Matter* **407** (16), 1003-1007, 2012.

38. Slater, J.C. A simplification of the Hartee-Fock Method. *Phys. Rev* **81** (3),385-390, 1951.

39. Kohn.W & Sham.L.J. Self consistent equation including exchange and correlation effects, *Phys.Rev* 140 (4A), A1133-A1138, 1965.

40. Phillips, J. C. Energy-Band Interpolation Scheme Based on a Pseudopotential, *Phys. Rev.* **112** (3), 685-695, 1958.

41. Payne, M.C.et.al Iterative minimization techniques for ab initio total-energy calculations: molecular dynamics and conjugate gradients, *Rev Mod.Phys* **64** (4),1045-1097, 1992.

42. Tsegaye, Z.A. *Density Functional Theory Studies Of Electronic and Optical Properties of ZnS Alloyed with Mn and Cr*. PhD Thesis. Norwegian University of Science and Technology at Department of Science and Technology, Norway, 2012.

43. Isserhoff, L.Y & Carter, E.A. Electronic Structure of Pure and Doped Cuprous oxide with Copper Vacancies: Suppression Of Trap States, *Chem Mater.* **25** (3), 253-265, 2013.

44. Janisch. R Transition metal doped TiO_2 and ZnO-present status of the field, *J. Phys: Condens. Matter* **17** (27), R657–R689,2005.

45. Ohno,H., et.al Magnetotransport properties of p-type (In,Mn) as diluted magnetic III-V semiconductors , *Phys Rev Lett* **68** (17) , 2664-2667,1992.

46. Ohno, H., et.al (Ga,Mn)As:a new ferromagnetic semiconductor based on GaAs, *Appl. Phys. Lett.* **69** (3), 363-365, 1996.

47. Matsumoto, Y., et.al. Room temperature ferromagnetism in transparent transition metal doped titanium di oxide, *Sci.***291** (5505), 854-856, 2001.

48. Bhattacharya, S., et.al One pot fabrication and magnetic studies of Mn doped TiO_2 nanoparticles, *Nanotechnol* **19** (49), 495711-495719,2008.

49. Peng, D., et.al. Structure , room-temperature magnetic and optical properties of Mn doped TiO_2 nanopowders prepared by sol-gel method, *Chin.Phys.B.* **19** (11), ,118102-118106, 2010.

50. Sellers,M. C.K. & Seebauer, E.G. Room temperature ferromagnetism in Mn-doped TiO_2 nanopillar matrices , *Mat. Lett.* **114** (1), 44-47, 2014.

51. Choudhury,B., et.al. Effect of oxygen vacancy and dopant concentration on the magnetic properties of high spin Co^{2+} doped TiO_2 nanoparticles, *J. Magn. Magn.*

Mater 323 (5), 440-446, 2011.

52. Dalpian, G.M & Wei, S.H. Electron induced stabilization of ferromagnetism in $Ga_{1-x}Gd_xN$, *Phys.Rev B* **72** (5),115201, 2005.
53. Dhar, S., et.al Colossal Magnetic Moment of Gd in GaN, *Phys Rev Lett* **94**(4), 037205, 2005.
54. Coey, J.M.D. et.al Magnetism in hafnium oxide, *Phys.Rev B* **72** (2), 024450, 2005.
55. Peng, H., et.al Possible origin of ferromagnetism in undoped anatase TiO_2, *Phys Rev.* **79** (9), 092411, 2009.
56. Elfimov, I.S.et.al. Possible Path to a New Class of Ferromagnetic and Half-Mettalic Ferromagnetic Material, *Phys. Rev. Lett.* **89** (21), 216403, 2002.
57. Hong, H.N., et.al Room temperature ferromagnetism observed in undoped semiconducting and insulating oxide thin films, *Phys.Rev.B* **73** (13), 132404,2006.
58. Yoon, S.D., et.al Oxygen defect induced magnetism to 880 K in semiconducting anatase TiO_2-delta films , *J.Phys.:Condens Matter* **18** (27), L355-L361,2006.
59. Coey, J. M. D., et.al. Donor impurity band exchange in dilute ferromagnetic oxides, *Nat. Mater.* **4** (2), 173-179,2005.
60. Coey,J.M.D., et.al. Ferromagnetism in Fe doped SnO_2 thin films, *Appl. Phys. Lett.* **84** (8), 1332-1334, 2004.
61. Akdogan. N *Origin of ferromagnetism in Oxide- Based Diluted Magnetic Semiconductors.* PhD Thesis. Ruhr-University Bochum, Germany,2008.
62. Akiho, D., et.al. Electrical injection of spin polarized electrons and electrical detection of dynamic nuclear polarization using a Heusler alloy spin source, *Phys. Rev.B* **87** (23), 23205, 2013.
63. Angelescu, D.E & Bhatt , N.R Effective interaction Hamiltonian of polaron pairs in diluted magnetic semiconductors, *Phys. Rev. B* **65** (7) ,075211,2002.
64. Lin, Z., et.al. New insights into the origin of visible light photocatalysis activity of nitrogen-doped and oxygen deficit anatase TiO_2, *J. Phys. Chem. B.* **109** (44), 20948-20952, 2005.
65. Liu, G., et.al Enhanced photoactivity of oxygen-deficient anatase TiO_2 sheets with

dominant {001} facets, *J.Phys.Chem.C* **113** (52), 217840-21788, 2009.

66. Ito.S., et.al Fabrication of thin film dye sensitized solar cells with solar to electric power conversion efficiency over 10%., *Thin Solid films* **516** (14), 4613-4619, 2008.
67. Elsanousi. A Highly ordered TiO_2 Nanotubes and their Application to dye sensitized Solar Cells, *J. Appl and Indus. Sci.* **1** (1),39-42, 2013.
68. Hwang.Y.K., et.al Preparation of Anatase/Rutile Mixed-Phase Titania Nanoparticles for Dye-Sensitised Solar Cells, *J.Nanosci and Nanotech* **13** (3),2255-2261, 2009.
69. Jacobs, F.J., et.al. Sunscreen with Titanium Dioxide (TiO_2) Nano-Particles: A Societal Experiment, *Nanoethics* **4** (2), 103-113, 2010.
70. Che, J. S., et.al. Constructing Hierarchical Spheres from Large Ultrathin Anatase TiO_2 Nanosheets with Nearly 100% Exposed (001) Facets for Fast Reversible Lithium Storage, *J. Am. Chem. Soc* **132** (17), 6124-6130, 2010.
71. Choi,W., et.al The Role of Metal Ions Dopants in Quantum-Sized TiO_2: Correlation be tween Photoreactivity and Charge Carrier Recombination Dynamics, *J. Phys. Chem.* **98** (51), 13669-13679, 1994.
72. Peng, H.Y., et.al Visible-light absorption and photocatalytic activity Cr-doped TiO_2 nanocrystal films, *Adv.Powder.Technol* **23** (1), 8-12, 2012.
73. Stengl, V., et.al Preparation and photocatalytic activity of rare earth doped TiO_2 nanoparticles. *Mater. Chem and Phys.* **114** (1), 217-226, 2009.
74. Choi, J., et.al Three-dimensional Gd doped TiO_2 fibrous photoelectrodes for efficient visible light-driven photocatalytic performance, *RSC Adv.* **4** (1),11750–11757, 2014.
75. Huang, Z., et.al Zn-doped TiO_2 electrodes in dye-sensitized solar cells for enhanced photocurrent, *J. Mater. Chem.* **22** (33), 17128-17132, 2012.
76. Song, J., et al. Improved Utilization of Photogenerated Charge Using Fluorine Doped TiO_2 Hollow Spheres Scattering Layer In Dye-Sensitized Solar Cells, *Appl. Mater. Interfaces* **4** (7), 3712-3717, 2012.
77. Kim, G.S., et.al Nb doped TiO_2 nanoparticles for organic dye-sensitized solar-cells,

RSC Adv **3** (37), 16380-16386,2013.

78. Zhang, W., et.al Mn-doped TiO_2 nanosheet- Based Spheres as Anode Materials for Lithium-Ion Batteries with High Performance at Elevated Temperatures, *Appl. Mater. Interfaces* **6** (10), 7292−7300 ,2014.
79. Kilinc.N., et.al Fabrication and gas sensing properties of C-doped and undoped TiO_2 nanotubes, *Ceramic.Inter* **40** (1),109-116,2014.
80. Datta. S & Das. B Electronic analog of the electro-optic modulator, *Appl.Phys.Lett.* **56** (7), 665-667,1990.
81. Lee, H., et.al Co doped TiO_2 nanowire field-effect transistors fabricated by suspended molecular template method, *Appl.Phys.Lett*, **86** (3),033110,2012.

CHAPTER 2

Materials and Methods

The choice of synthesis techniques is very important in determining the effectiveness of a photocatalyst. In this chapter we will discuss the preparation method of undoped and metal ion doped TiO_2 (Mn, Ni, Gd, Er) nanoparticles via a low cost, simple sol-gel method. In sol-gel method two simultaneous reaction takes place (hydrolysis and condensation) when organometallic precursor reacts with water. The two reactions are very sensitive to many experimental parameters such as raw material, concentration, pH, hydrolysis, temperature and mixing condition [1]. Structural and morphological studies are carried out with techniques such as X-ray diffraction (XRD), transmission electron microscopy (TEM), energy dispersive X-ray analysis (EDX). Surface area analysis is done via Brunauer-Emmett-Teller (BET). The oxidation state of the dopant ion and its coordination environment is studied through X-ray photoelectron spectroscopy (XPS).Theoretical study using density functional theory is carried out to indentify the states introduced by the dopant ion.

2.1. Sol gel synthesis of undoped and metal ion doped TiO_2 nanoparticles.

2.1.1. Preparation of undoped TiO_2 nanoparticles.

The reagents used for the synthesis were Titanium Isopropoxide (TTIP, purity 97%) and Isopropanol (99%). The synthesis was started adding 15 ml of isopropanol to 5 ml Titanium Iso-propoxide solution. The solution was allowed to stir for about 15 min and then 1 ml of water was added to initiate the hydrolysis process. The solution became turbid and the stirring was continued until gel formation. The transformation from initial sol to gel took about 6-7 hrs. The gel was left for ageing for about 12 hrs. This was followed by centrifugation with ethanol and water for 5 times. The centrifuged product was dried in an oven at 80°C. A part of the dried product was annealed in vacuum at 200°C. This part is chosen for a comparative study of the magnetic property of vacuum annealed TiO_2 and vacuum annealed Mn doped TiO_2 and is reported in Chapter 5. The remaining part of the

dried product was annealed at 450, 650, 850°C for 3 hrs and the sample were labeled as T45, T65, T85 respectively. Annealing at three different temperatures were carried out to clearly distinguish the anatase and rutile phase, their sizes and defects present. A detailed study on the optical property and photocatalytic activity of the reduced anatase, anatase-rutile mixed phase and rutile phase are reported in Chapter-3.

2.1.2. Preparation of Nickel doped TiO_2 nanoparticles.

For synthesizing Ni doped TiO_2 nanoparticles with different concentrations (0.03, 0.05, 0.07 mol) sol-gel method was used. Titanium Isopropoxide (TTIP), Isopropanol, Nickel nitrate hexahydrate was used as the starting chemicals. 5 ml of TTIP was added to 15 ml of isopropanol under constant stirring condition. Then a few drops of water were added to initiate the hydrolysis reaction. Nickel nitrate hexahydrate $Ni(NO_3)_2.6H_2O$, was slowly added to the hydrolyzed mixture under vigorous stirring to obtain the sol containing x=0.03,0.05,0.07mol nickel. On completion of the addition of all dopant solutions, the mixture was stirred for 5 h. During this time of the reaction, first a sol was formed, which ultimately transformed into gel. After this time period the stirring was stopped, and the gel was left in ageing. condition for 12h.The prepared material was dried in air at 80°C and then heat treated at 450°C to get the desired Ni^{2+} doped TiO_2 nanoparticles.

2.1.3. Preparation of Manganese doped TiO_2 nanoparticles.

Mn doped TiO_2 nanoparticles with three different concentrations (0.03 mol, 0.05 mol and 0.07 mol) were synthesized employing a simple sol-gel method. The precursors for dopant and host were taken to be Manganese Acetate tetrahydrate and titanium iso-propoxide respectively. 5 ml of titanium isopropoxide and 15 ml of 2 propanol were added to a 100 ml conical flask under constant stirring, followed by the addition of 1 ml of water to initiate the hydrolysis reaction. To the white sol of titanium isopropoxide, the dopant precursor solution were added and stirred for 7-8 h. The reaction progressed with the formation of sol which was ultimately transformed into a gel. The gel was then centrifuged in water followed by ethanol at a rate of 10,000 rpm for 4 times. The centrifuged product was dried at 80 ^{0}C. A part of the dried product was annealed in vacuum at 200°C and the remaining

product was finally annealed at 450 ^{0}C to obtain Mn doped anatase TiO_2 nanoparticles.

2.1.4. Preparation of Gadolinium doped TiO_2 nanoparticles.

Gd doped TiO_2 nanoparticles with three different nominal concentrations of Gd (0.03 mol, 0.05 mol, 0.07 mol) were synthesized employing a simple sol-gel method taking gadolinium nitrate hexahydrate and titanium iso-propoxide as the starting chemical. 5 ml of titanium isopropoxide and 15 ml of 2 propanol were added to a 100 ml conical flask under constant stirring, followed by the addition of 1 ml of water to initiate the hydrolysis reaction. To the white sol of titanium isopropoxide, the dopant precursor solution was added and stirred for 7-8 h. During such process first a sol was formed which ultimately transformed into a gel. The gel was then centrifuged in water followed by ethanol for 4 times. The centrifuged product was dried at 80 ^{0}C. The resulting product was finally annealed at 450 ^{0}C to obtain crystalline gadolinium doped anatase TiO_2 nanoparticles.

2.1.5. Preparation of erbium doped TiO_2 nanoparticles.

Pure and erbium doped TiO_2 nanoparticles with three different concentration of erbium (0.03, 0.05, 0.07 mol) were prepared taking simple sol-gel route. The reaction was started with the addition of 5 ml titanium iso-propoxide to 15 ml of 2-propanol. The reaction mixture was stirred for 15 min and then aqueous erbium nitrate hexahydrate solution was added to the above mixture and stirred. The resultant product was a gel which was centrifuged , dried and annealed at 450 ^{0}C for 4 h to get crystalline erbium doped TiO_2 nanoparticles.

2.2. Experimental method for the characterization of nanoparticles.

X-ray diffraction (XRD) study.

X-ray diffraction is an important technique to study, non-destructively, the crystallographic structure, chemical composition and physical properties of materials and thin films. It is primarily used for phase identification, defects and can provide information on unit cell dimension. In XRD an X-ray beam is generated by a cathode ray tube, filtered to produce monochromatic radiation, collimated to concentrate and directed towards the sample. The

sample to be analyzed is finely grounded, homogenized and average bulk composition is determined. The condition for a crystalline material to yield a distinct diffraction pattern is that the wavelength of incident radiation should be comparable to or less than the inter-atomic spacing in the lattice. The X-ray diffraction of a crystal can be formulated by Bragg's law [2].

$$n\lambda = 2d \sin\theta \quad \text{---------- (2.1)}$$

where n is the no of diffraction, d is the lattice spacing and θ is the diffraction angle. The usual information depth of X-ray measurement ranges from a few micrometer to a few hundred micrometer depending on the density of the material [3].

The X-ray diffraction pattern of bulk and nanomaterials have some differences. Owing to the presence of small particle size nanomaterials broadens the lines in the diffraction peaks. This broadening results in the loss of intensity in the signal of the diffraction peak whereas bulk materials have sharp, narrow and high intensity peaks [2].

X-ray diffraction pattern of pure and all the doped samples is performed using Rigaku Miniflex CD 10041 XRD unit with copper target and λ=1.54 angstrom at a scanning rate of 1°/min and in the scanning range of 10-80°. The diffraction pattern of the samples is indexed with the standard card file no of the corresponding bulk materials in the Joint Committee on Powder Diffraction Standards (JCPDS). JCPDS is the organization that maintains the data base of inorganic and organic spectra's.

2.2.1. X-ray diffraction of Ni doped TiO_2 nanoparticles.

Fig.2.1 shows the XRD pattern of undoped and all the Ni doped TiO_2 nanoparticles. All the diffraction peaks correspond to the tetragonal anatase phase (JCPDS card no.78-2486) without the trace of any secondary phase. Gaussian fitting of (101) peak indicates peak broadening with the increase in dopant concentration inferring a systematic decrease in the grain size. The mean size of the crystallites in the sample is estimated using Scherrer's equation. The average crystallite size is found to decrease from 16 nm to 7.5 nm with increasing nickel concentration and is attributed due to the formation of Ni-O-Ti bond [4].

Another possible reason is , radius of the Ni^{2+} ions (69 pm) being larger than Ti^{4+} (60 pm), it is generally difficult for all the nickel ions to penetrate the TiO_2 surface and substitute Ti^{4+} inside the lattice. In that situation only a few nickel ions penetrate the lattice , the rest sits on the grain boundary and inhibits the growth .

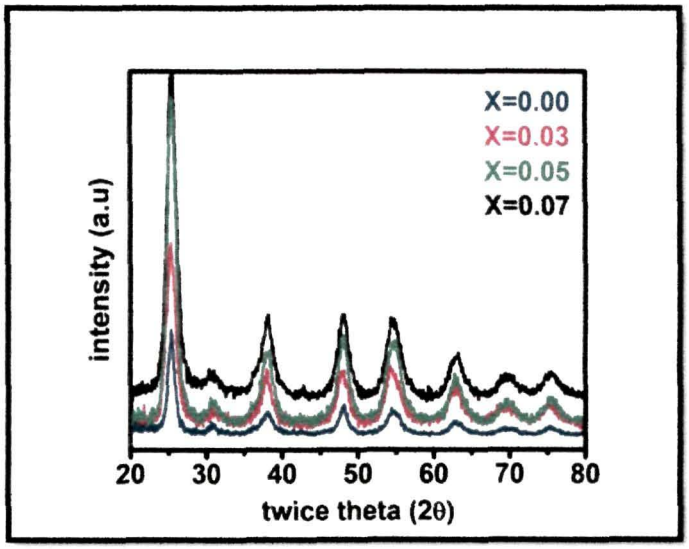

Fig.2.1: XRD pattern of Ni doped TiO_2 nanoparticles.

2.2.2. Diffraction pattern analysis of Mn doped TiO_2 nanoparticles.

The XRD patterns of $Ti_{1-x}Mn_xO_2$ (x=0.03, 0.05, 0.07) are shown in Fig 2.2 (a). The anatase phase is preserved after doping and no hint of manganese containing oxide phase is resolved. The main anatase peak (101) shifts to lower angle with increase in manganese concentration (inset of Fig.2.2a). Further an increase of the lattice c-parameter, cell volume and strain is noticed (Fig 2.2b , Table 2.1) The average crystallite size is calculated using Scherrer's formula [5]. As can be seen from the XRD patterns (inset of Fig.2.2a) the (101) diffraction peak gets broadened as the manganese concentration is increased suggesting a systematic decrease in grain size. For undoped TiO_2 the average grain size is 18 nm (fwhm = 0.4308 radian) while it decreases to 7 nm (FWHM=1.168) with 7% manganese incorporation. The incorporated manganese ions in the TiO_2 lattice thus suppress the grain growth by interfering into the intergranules that inhibits the grain boundary mobility or

alter the surface energy leading to a decrease in grain growth velocity or nucleation energy resulting in the decrease in grain size [6,7]. A detailed analysis of the optical, photocatalytic and magnetic property of this material is given in Chapter 5.

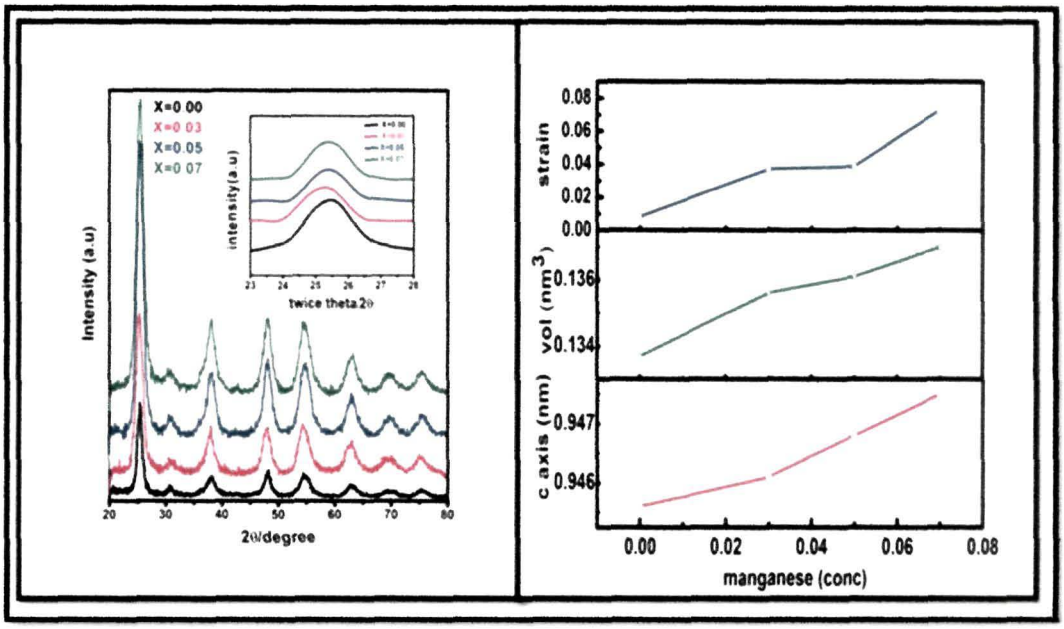

Fig.2.2: (a) XRD pattern of all the samples. Inset showing shifting of (101) peaks to lower angle side. (b) Plot of c-axis, volume, strain with increase in dopant concentration.

Dopant conc (mol)	Crystallite size (nm)	c-axis (nm)	Vol (nm^3)	strain
X=0.00	18	.9456	.1337	.0082
X=0.03	11	.9461	.1356	.0371
X=0.05	9.7	.9468	.1361	.0387
X=0.07	7	.9575	.1370	.0729

Table.2.1: Calculation of crystallite size, c-axis, vol, strain from XRD.

2.2.3. Diffraction pattern analysis of Gd doped TiO_2 nanoparticles.

Fig.2.3. shows the diffraction pattern of undoped and all the Gd doped TiO_2 samples. All the diffraction peak corresponds to the tetragonal anatase phase. A small amount of brookite phase is detected in between 27^0 and 31^0. The sizes of the nanocrystal are calculated using Scherrer's formula [5]. The crystallite size is calculated to be 7.8 nm for pristine (0.00 mol) and 5.9 nm, 5.45, 5.42 nm for 0.03, 0.05 and 0.07 mol of Gd respectively. The width of the diffraction peaks increases with the increase in doping concentration. The widening of the diffraction indicates systematic decrease in grain size and degradation of the structural quality after doping. Because of the moderately large size incongruity with Ti^{4+} (0.68 Å), Gd^{3+} (0.94 Å) ions are not expected to inhabit sites in the lattice of TiO_2 [8]. They possibly stay on the particle surface and on the grain boundaries and produce a strain in those regions. This results in the enhancement of the repulsive interaction between the Gd^{3+} ions, prevent the coalescence of nanocrystallites and thereby inhibits the growth by the formation of Gd- O-Ti bond [9].

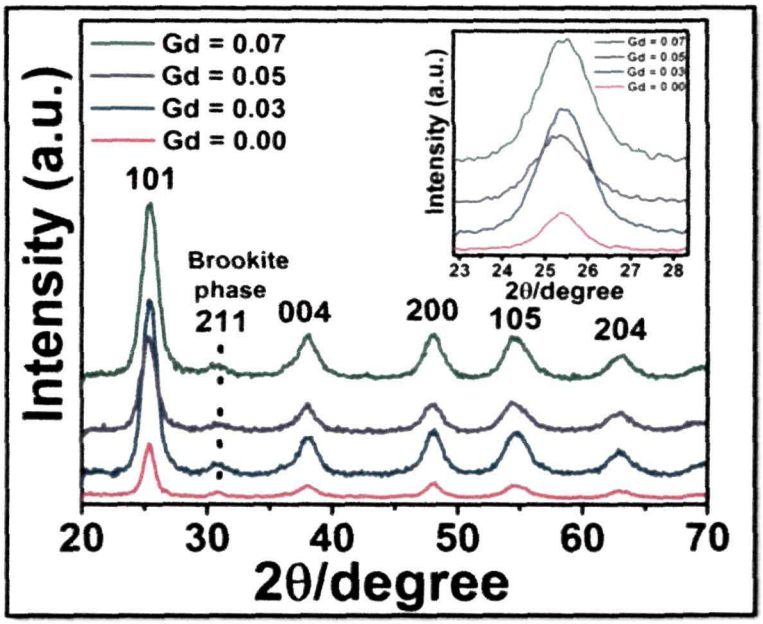

Fig.2.3: XRD pattern of undoped and Gd doped TiO_2 with Gd concentration 3 mol%, 5 mol %, 7mol % with inset showing the shifting of (101) peak to lower wave number.

It is observed that with increase in Gd doping concentration the intensity of diffraction peak is increasing. The diffraction peak intensities are affected by the change in electron density due to substitution of foreign (dopant) atoms. Through doping we change the element that is we change the mean atomic scattering factor. Doping with light atom might results in lowering of diffraction intensity. However doping with a larger Gd^{3+} results in more scattering centers and hence, results in increased peak intensity [10]. The diffraction pattern does not show any peak of secondary phases of gadolinium such as Gd_2O_3. However, slight shifting of the peaks to lower angle is noticed with the changes in the gadolinium concentration. We have also calculated the *d* spacing of all the samples considering (004) peak. The values are calculated to be 0.23586, 0.23595, 0.23615 and 0.23622 nm for undoped and (0.03, 0.05, 0.07 mol) Gd doped TiO_2 nanoparticle. The change in *d* spacing is not prominent inferring that very few percentage of the total gadolinium impurity ions are actually substituting Ti^{4+} on the lattice interior and the others may be located on the surface. Chapter 6 contains a detailed study of the effect of incorporating gadolinium ions on the optical, photocatalytic and magnetic properties of TiO_2 nanoparticles.

2.2.4. Diffraction pattern analysis of Er doped TiO_2 nanoparticles.

The XRD patterns of all the samples are shown in Fig.2.4. The peaks are indexed to the tetragonal anatase phase (JCPDS-21-1271). The peak positions donot show any appreciable changes. Furthermore, no hint of Erbium containing oxide phase is resolved within the limit of instrumental sensitivity. Gaussian fitting of the most intense (101) peak indicates broadening of the diffraction peaks, inferring a systematic decrease in the crystallite size after doping. The crystallite size of the samples are calculated using Scherrer's formula. The crystallite size is calculated to be 9.8 nm for pristine (0.00 mol) and 5.4 nm, 5.2, 5.0 nm for 0.03, 0.05 and 0.07 mol of Er respectively. Fig.2.4 (b) shows the variation of FWHM and crystallite size with increase in dopant concentration. The decrease in crystallite size occurs due to difference in the radii of Er and Ti atoms. Erbium has an ionic radius 1.004 Å [11] and Ti^{4+} (0.61 Å) [14]. Due to such huge difference in the ionic radii

incorporation of Er ions creates a tensile strength in the TiO_2 lattice and in turn prevents the grain growth [12].

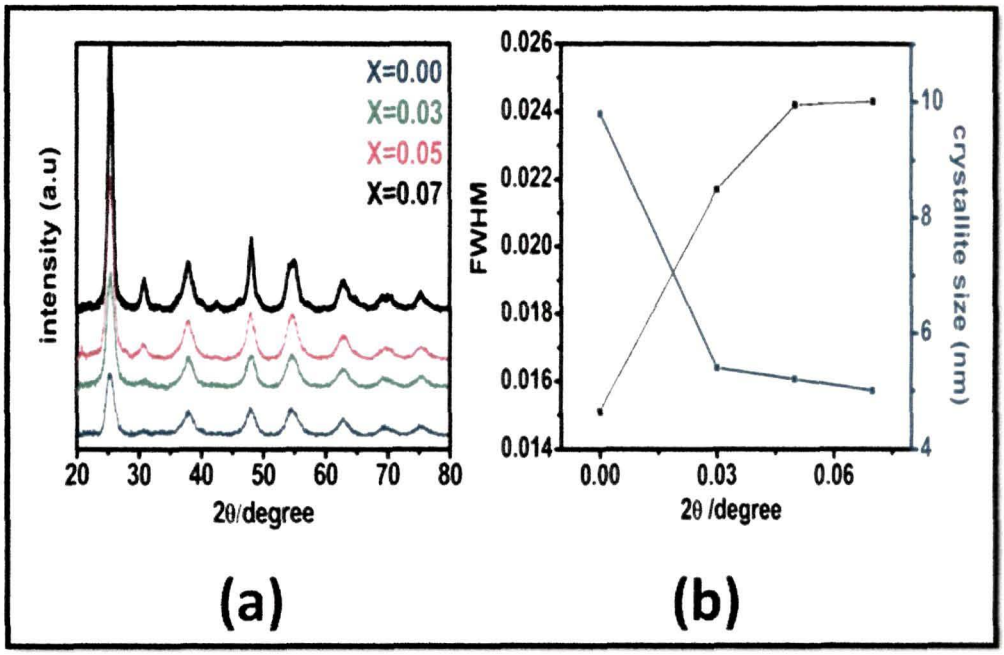

Fig.2.4: (a) X-ray Diffraction spectra of pure and Er doped TiO_2 nanoparticles. (b) Variation of FWHM and crystallite size with dopant concentration

Transmission electron microscopy analysis (TEM) and energy dispersive X-ray (EDX).

Transmission electron microscope is a very important tool for microstructural characterisation on nanometer scale. The microstructural information broadly includes ascertaining the morphology of phases, number of phases, structure of phases , identification of crystallographic defects and composition of the phases, required for structural property connection and for carrying out basic and applied research in materials. TEM gives all these aforesaid informations [13].

XRD gives information about the size of coherently diffracting grain size whereas TEM provide direct evidences of the nanoparticle size, shape. Due to the polycrystalline nature containing several grain sizes the crystallite size is not generally the same as the

particle size [10]. TEM works by using a tungsten filament to produce an electron beam in a vacuum chamber. The emitted electrons are accelerated through an electromagnetic field that closely focuses the beam. The beam is then passed through the sample material. The sample to be analyzed must be very thin so that the electrons can make their way through the sample and produce an image. For samples with less density, more electrons get through and produces brighter image. However, a darker image is produced in areas where the sample is more dense and therefore less electrons pass through.

Energy dispersive X-ray (EDX) is a qualitative and quantitative micro analytical technique for the elemental analysis or chemical characterization of a sample with atomic number Z> 3. The data produced by EDX analysis consist of spectra showing peaks corresponding to the elements making up the true composition of the sample being analyzed. In this technique when the sample is bombarded by the electron beam, electrons are ejected from the atoms generating a hole in the lower energy core level. The resulting electron vacancies are filled by electrons from the higher energy state and an X-ray is emitted to balance the energy difference between the two electron states. An energy dispersive (EDS) detector is used to separate the characteristic x-rays of different element into an energy spectrum. The detector usually consists of a crystal that grips energy of incoming X-rays by ionization yielding free electrons in the crystal that becomes conductive and thus converts the individual X-rays into electrical voltages of proportional size, the electrical pulses corresponds to the characteristic X-ray of the element [14,15,16].

2.3.1. TEM and EDX study of Ni doped TiO_2 nanoparticles.

Fig 2.5a and 2.5b shows the transmission electron microscope images of undoped and Ni^{2+} doped TiO_2 nanoparticles from where the average particle size are calculated to be 18.4 nm and 8.8 nm respectively. Addition of Ni^{2+} ions thereby arrests the growth of TiO_2 nanoparticles and this finding is quite consisted with the XRD analysis. The EDX pattern for 0.05 Ni^{2+} doped TiO_2 (Fig 2.5c) sample shows presence of constituent element in the doped sample.

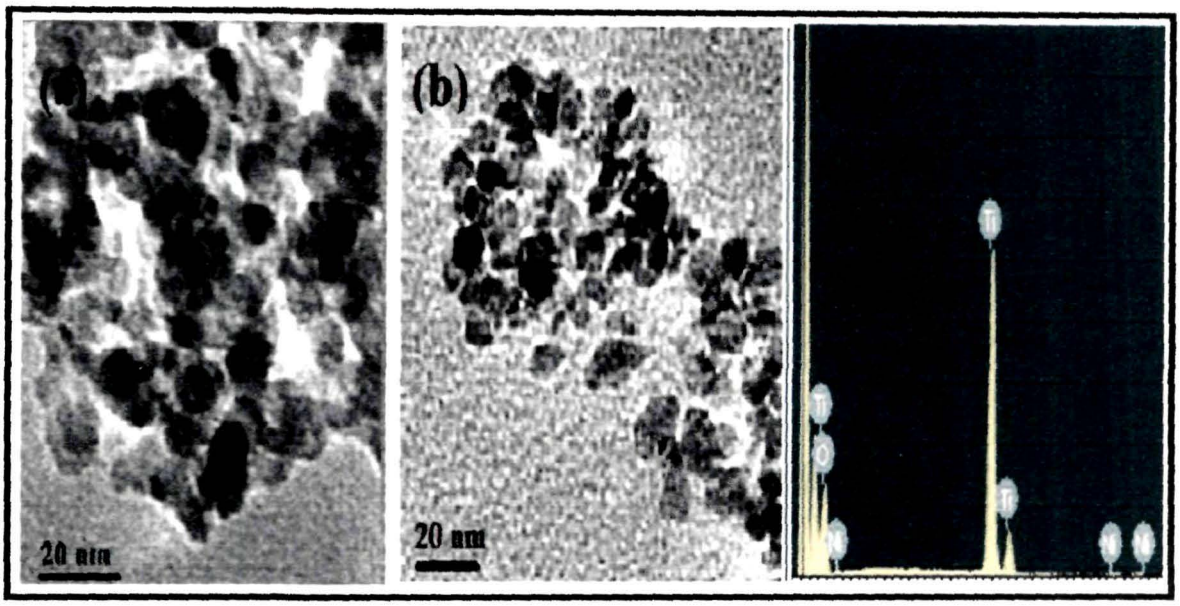

Fig.2.5: TEM images of (a) Undoped (b) 3% Ni doped TiO_2 nanoparticles (c) EDX pattern showing the constituent in the doped samples.

2.3.2. TEM and EDX study of Mn doped TiO_2 nanoparticles.

TEM images of undoped and 5 % Mn doped TiO_2 nanoparticles are shown in Fig.2.6 (a)

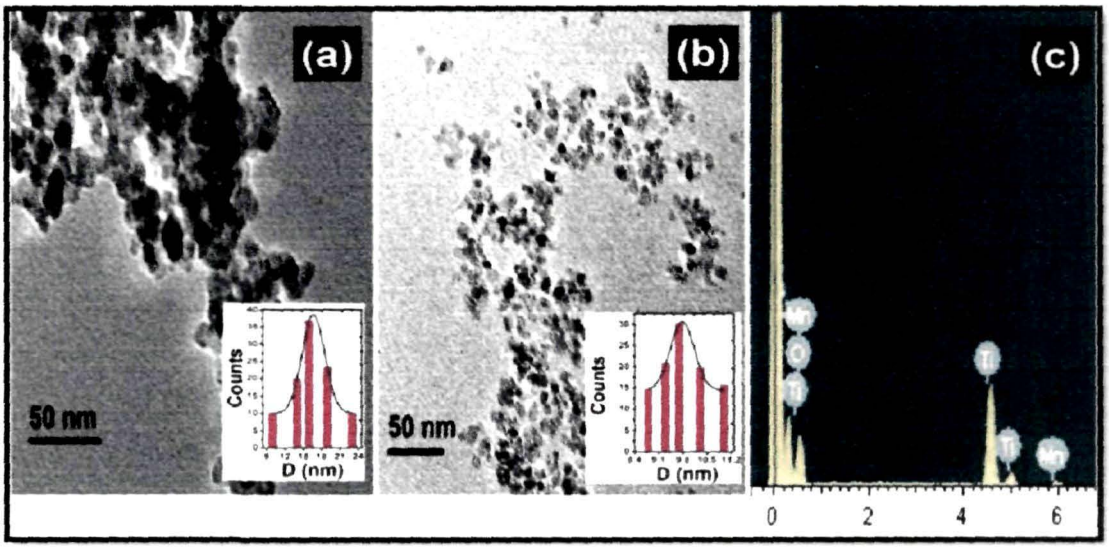

Fig.2.6: TEM images of (a) undoped (b) 0.05 mol Mn doped TiO_2, inset showing the particle size distribution (c) EDX analysis.

and Fig.2.6 (b) respectively.After Gaussian fitting the average particle size in both undoped and doped samples are calculated to be ~ 16±0.002 nm and ~ 9±0.003 nm respectively. The elemental composition verified with the help of EDX spectra (Fig.2.6c) corroborates presence of Mn, Ti, O as constituent element in the doped samples.

2.3.3. TEM and EDX study of Gd doped TiO_2 nanoparticles.

The transmission electron microscope images of the undoped and Gd doped TiO_2 nanoparticles are shown in Fig 2.7 (a-d).

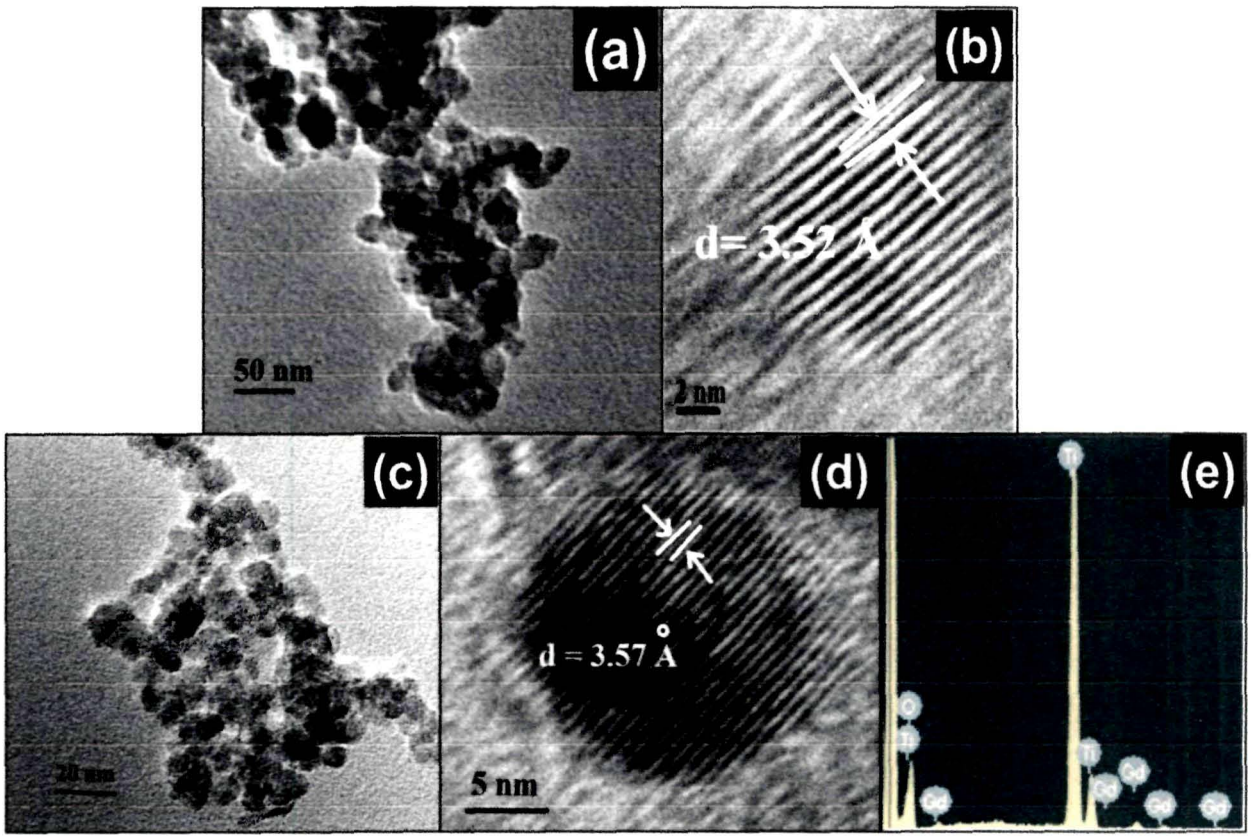

Fig.2.7: TEM images of (a) undoped (c) 0.03 mol Gd doped TiO_2; High Resolution images showing the lattice fringes of (b) undoped and (d) doped TiO_2 nanoparticles. (e) EDX analysis of 0.03 mol Gd doped TiO_2.

As observed from the micrographs, the undoped system comprises of spherical size

particles of ~ 18 nm size (as shown in Fig.2.7a). Fig 2.7b shows the corresponding high resolution image of pure TiO_2. The distinct lattice fringes with inter planar spacing of ~ 3.52 Å, corresponding to the (101) plane of anatase TiO_2 displays highly crystalline nature of the samples [17]. Fig 2.7c shows the TEM image of 0.03 mol Gd doped TiO_2. The average particle size is calculated to be ~ 12 nm. The interplanar spacing shown in Fig. 2.7d is found to be ~ 3.57 Å. The interplanar spacing of the doped and undoped TiO_2 nanoparticles do not show much variation, further confirming incorporation of only few gadolinium ions on the TiO_2 lattice. A nanoparticle of polycrystalline aggregates is composed of grains of several sizes. Scherrer's formula determines the size of coherently diffracting grain size. Moreover, the size determined by Scherrer formula is affected by instrumental broadening, crystalline strain, defects, etc. On the other hand TEM provide direct evidences of the nanoparticle size, shape. Due to the polycrystalline nature containing several grain sizes the crystallite size is not generally the same as the particle size [18,10].The compositional analysis is performed with EDX analysis. The spectrum is marked with the signals obtained from Ti, O, Gd.

2.3.4. TEM and EDX study of Er doped TiO_2 nanoparticles.

The results from TEM measurements are shown in Fig.2.8 (a-b).

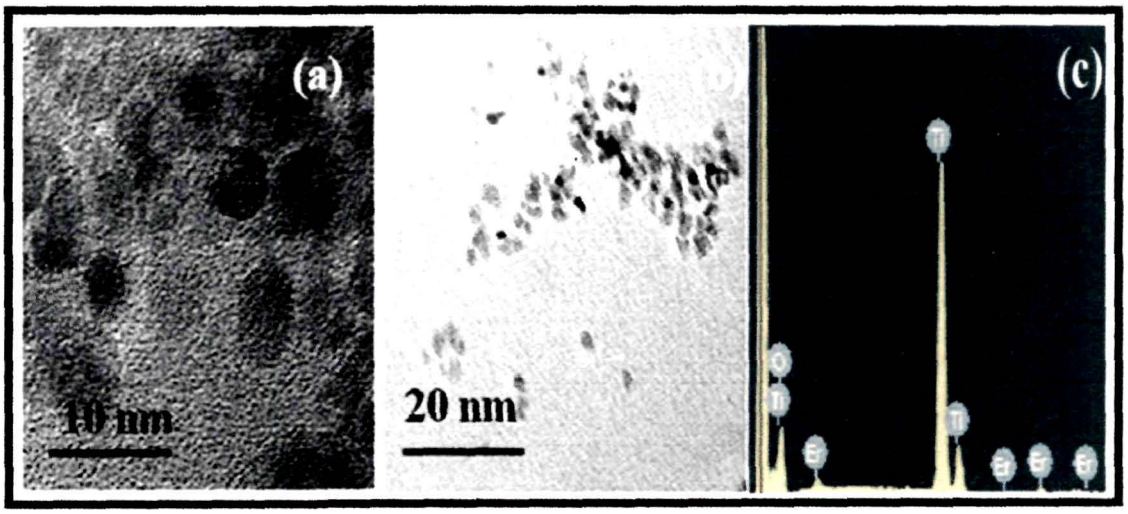

Fig.2.8: TEM images of (a) undoped (b) 0.07 mol Er doped TiO_2 (c) EDX analysis of 0.07 mol Er doped TiO_2.

The average particle size for undoped and doped system are calculated to be ~ 14 nm and ~7 nm respectively.Incorporation of Er ions thus hinders the particle growth and the results are in conformity with the decrease in crystallite size calculated from the XRD results. As the nanoparticles are synthesized without the use of any surfactant so we have no control over the shape and size of the nanoparticles. From the micrograph it is seen that the nanoparticles are highly agglomerated with non-uniform size distribution and are apparently spherical. In order to verify the presence of Er ions in the doped samples they are analyzed with the help of EDX spectroscopy, Fig.2.8 (c). The spectra clearly reveals the emission peaks corresponding to O, Ti, Er.

X-ray photoelectron Spectroscopy

X-ray photoelectron spectroscopy is a quantitative spectroscopic technique widely used for studying the properties of atoms, molecules, solids and surfaces. The principle of X-ray is based on the measurement of kinetic energy of photoelectrons generated by the sample. If an X-ray photon with energy hυ excites an atom from its initial state with energy E_i to final state with energy E_f state, in the process emitting an electron with kinetic energy KE, than according to the law of conservation of energy, the emitted electrons have kinetic energy given by [19].

$$h\upsilon + E_i = KE + E_f \quad \text{---------- (2.2)}$$

The difference between the photon energy and the electron kinetic energy gives the binding energy of the orbital from which the electron is ejected [17]. This binding energy gives the characteristic for different orbitals of specific elements [17].

X-ray photoelectron spectroscopy (XPS) of undoped and all the doped samples (Mn, Ni, Gd, Er) are recorded on KRATOS-AXIS 165 instrument equipped with dual aluminium-magnesium anodes using the Mg K_α radiation ($h\nu$=1253.6 eV) operated at 5kV and 15 mA with pass energy 80 eV and an increment of 0.1 eV .The samples were degassed out for several hours in XPS chamber to minimize air contamination to sample surface. The fitting of the XPS curve have been done using a non-linear square method with

the convolution of lorentzian and Gaussian functions after a polynomial background was subtracted from the raw spectra.

2.4.1. XPS study of Ni doped TiO_2 nanoparticles.

Fig.2.9 shows the XPS spectra of Ni doped TiO_2 nanoparticles. The binding energy peak positions appearing at 856.06 and 873.97 eV corresponds to Ni $2p_{3/2}$ and Ni $2p_{1/2}$ respectively. The binding energy difference of 17.9 eV corresponds to Ni^{2+} [18]. This binding energy peak is less than that of NiO (18.4 eV). Hence the presence of NiO in our sample can be completely ruled out. The spectra contains two more peaks appearing at 869.38 and 878.09 eV. These peaks corroborates the auger line TiLMM [19].

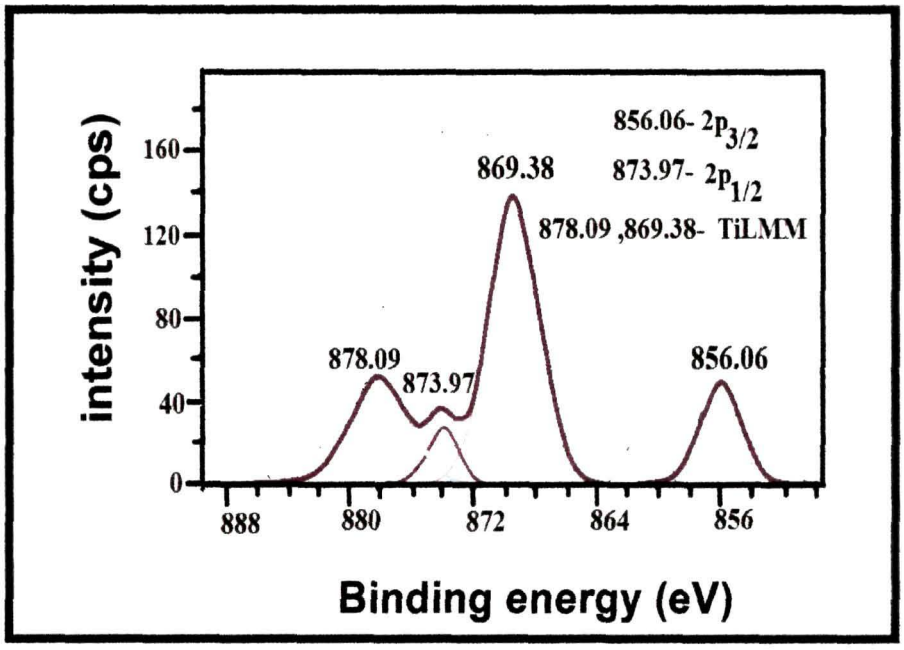

Fig.2.9: XPS spectra of Ni doped TiO_2 nanoparticles.

2.4.2. XPS study of undoped and Mn doped TiO_2 nanoparticles.

The XPS spectra are investigated to study the oxidation state of the ions present in the sample and also to study the oxygen vacancy created. Fig.2.10 (a-c) shows the XPS spectra of Ti 2p, O 1s and Mn 2p respectively. The core level binding energies of Ti $2p_{3/2}$ and

Ti $2p_{1/2}$ are at approximately 458.74 eV and 464.5 eV. The difference of 5.75 eV indicates a valence of +4 for Ti in TiO_2 [20]. As for Mn the binding energy peak for Mn $2p_{3/2}$ and Mn $2p_{1/2}$ corresponds to 641.5 and 653.5 eV, Fig.2.10 (b) and this is the typical characteristics of Mn^{2+} ions [21].To study the presence of oxygen vacancies core level XPS O1s spectra are also analyzed, Fig.2.10 (c). The spectra indicates presence of two kinds of chemical states that include crystal lattice oxygen (O_L) and chemiabsorbed oxygen (O_H).The O_L peak appearing around 530.1-530.2 eV is due to to the contribution of Ti-O in the TiO_2 crystal and that appearing at 531.9-532.62 eV is due to the hydroxyl groups (O_H) arising from the chemiabsorbed water [22]. The amount of O_H in both pure and doped sample is much more than that of O_L (Table-2.2). Naeem.et.al [23] reported that the presence of the O_H peak is developed with the increasing oxygen vacancy. These oxygen vacancies are actually created to maintain the charge neutrality when the local electrostatic bond is broken and the host Ti^{4+} ions is changed to Ti^{3+} [24].

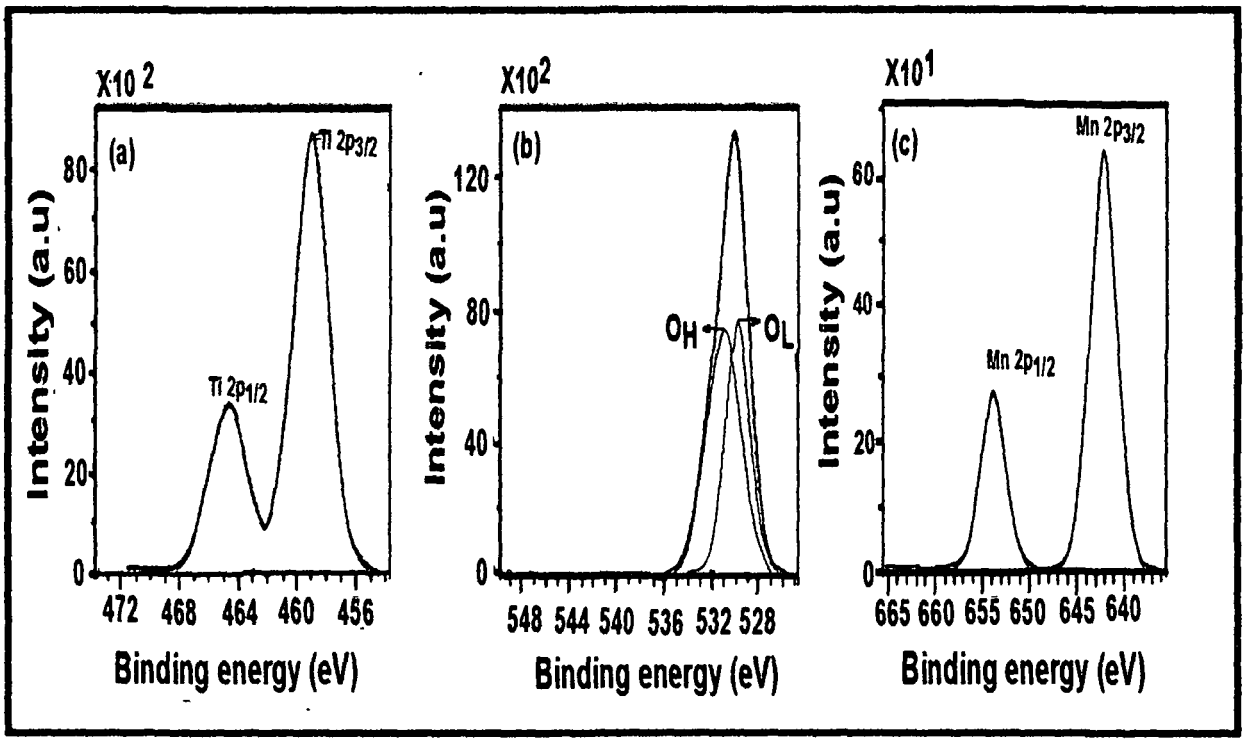

Fig.2.10: XPS spectra (a) Ti 2p (b) Mn 2p (c) O 1s spectra

Samples	Detailed Study	O_L	O_H
TiO_2	Position	530.2 eV	531.93
	At%	49.9	50.1
TiO_2: Mn	Position	530.10 eV	532.62
	At%	42.8	57.2

Table. 2.2: Quantitative analysis of O_H and O_L from XPS spectra

2.4.3. XPS study of Gd doped TiO_2 nanoparticles.

The core level XPS spectra of 0.07 Gd doped TiO_2 nanoparticles is shown in Fig.2.11. The valence state of Gd ion is ascertained to be +3 as the binding energy of Gd $4d_{3/2}$ peak at 143 eV [25].

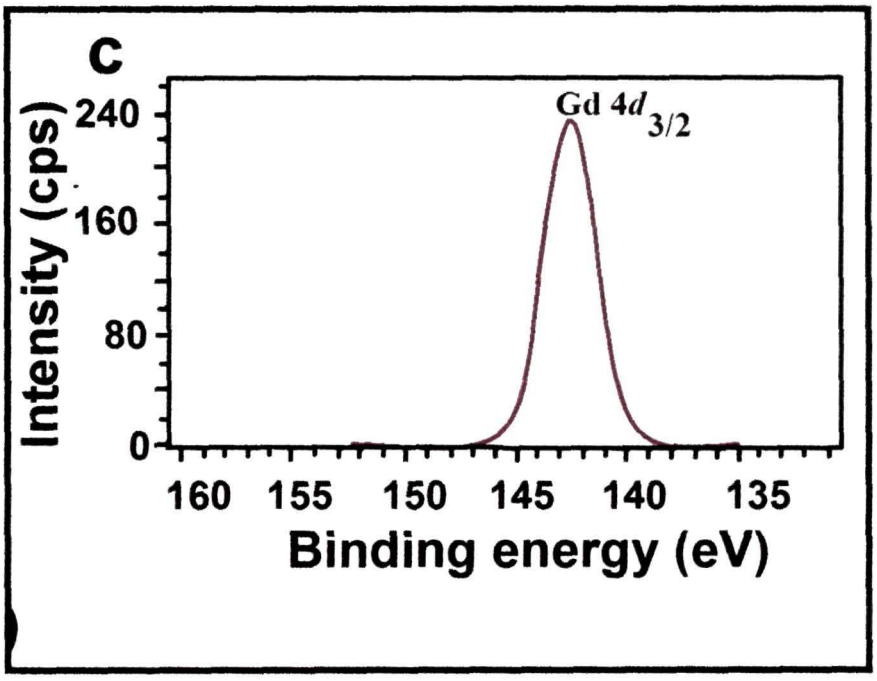

Fig.2.11: XPS spectra of Gd doped TiO_2 nanoparticles .

2.4.4. XPS study of Er doped TiO_2 nanoparticles.

Fig.2.12 shows the XPS spectra of 0.07 mol Er doped TiO_2 nanoparticles. The Er 4*d* spectrum is seen to be composed of two peaks originating at 168.74 and 178.32 eV. These peak positions corresponds to Er $4d_{5/2}$ and Er $4d_{3/2}$ respectively [26].

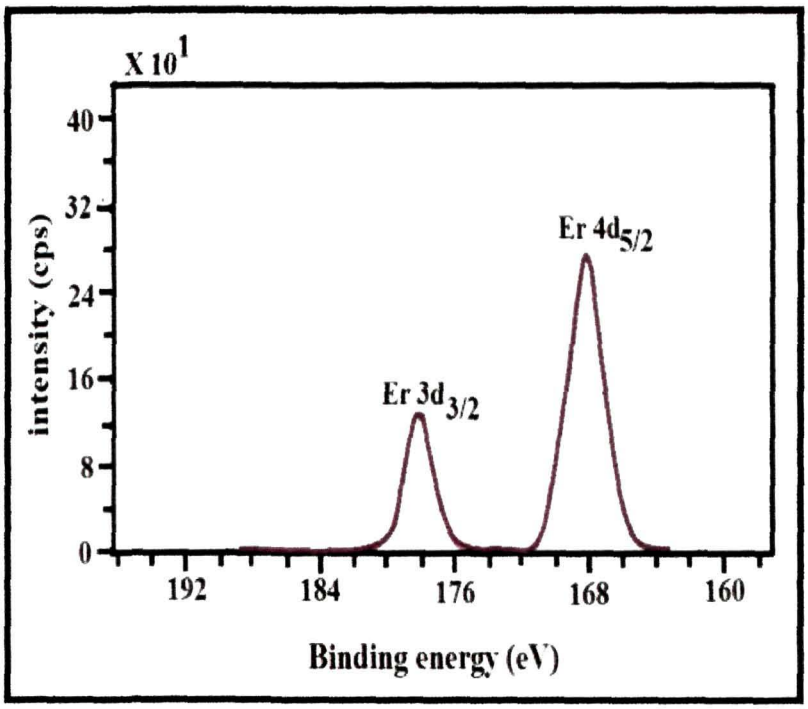

Fig.2.12: XPS spectra of Er doped TiO_2 nanoparticles .

Raman Spectroscopy.

Raman spectroscopy offers a bottom up approach in the study of nanomaterials and nanostructures. The spectra can be obtained for most molecular samples that includes solids, liquids, gels, slurries, powders, films etc [27]. Raman spectroscopy counts on inelastic or raman scattering of monochromatic light usually from a laser. For a molecule to exhibit Raman effect alteration in polarizability or the amount of deformation of the electron cloud with respect to the vibrational coordinate, is very desirable. Interaction of the laser light with phonons or other excitations in the system results in the energy of the laser

photons to shift up or down. The shift in energy gives information about the phonon modes in the system. The analysis of the Raman mode wave numbers, widths and intensities allow us to obtain information about the composition, chemical environment, bonding and crystalline/amorphous structure of the material under investigation [28] .

The Raman spectra of the samples are acquired with Reinshaw in Via Spectrometer. The 514.5 nm emission of Argon-ion laser is used as excitation source.

2.5.1. Raman Spectra of Ni doped TiO_2 nanoparticles.

The Raman spectra of undoped and Ni doped TiO_2 nanoparticles are shown in Fig. 2.13(a). The Raman modes are observable at 145 cm^{-1} (E_g) , 195 cm^{-1} (E_g), 399 cm^{-1} (B_{1g}) , 517 cm^{-1} (B_{1g}), 640 cm^{-1} (Eg). All these modes correspond to anatase phase [29]. No peaks related to Ni or its oxide phase is detected indicating that the anatase phase is well preserved even after doping.

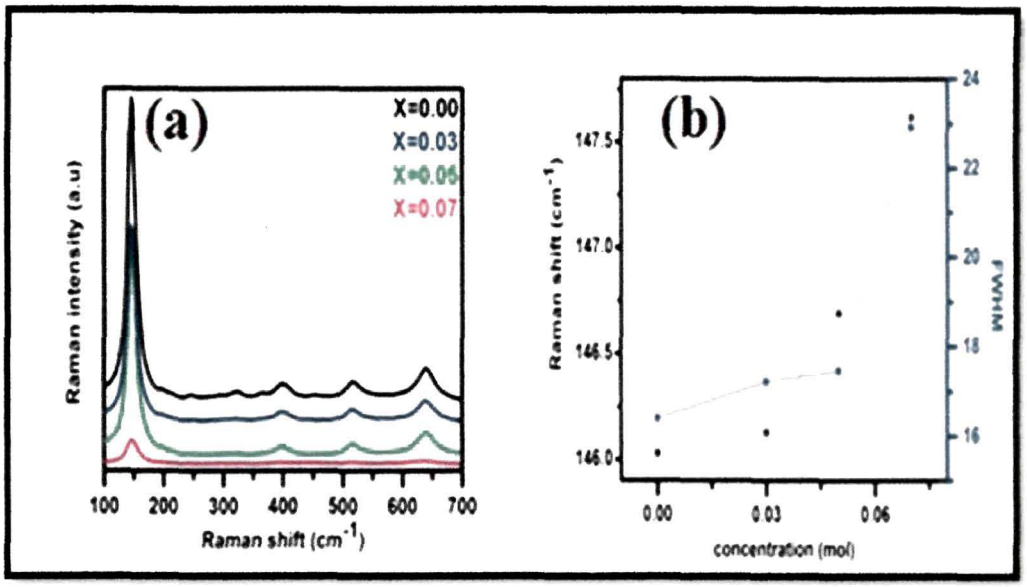

Fig.2.13: (a) Raman spectroscopy of Ni doped TiO_2 nanoparticles (b) variation of Raman shift and FWHM with dopant concentration.

The Raman peaks are very responsive to any disarray taking place in the oxygen coordination in the TiO_2 lattice. The Eg peak is attributed to the O-Ti-O bending vibration

and is very much responsive to local oxygen co-ordination surrounding the metal ion [21]. Substitution of Ti^{4+} ions by Ni^{2+} ions distorts the host lattice and generates oxygen vacancy to maintain the charge neutrality. Formation of oxygen vacancies reduces the average number of Ti-O/Ni-O bonds and shifts Eg peak to higher wavenumber [30]. The strength of a bond is determined by its force constant and the force constant is associated with frequency by $\nu \propto \sqrt{k}$ [31]. Fig.2.13(b) shows the shifting of Eg peaks to higher wave numbers and the increase in FWHM with increase in dopant concentration. The diminution in the scattering intensity of the Eg mode may be due to the collapse of translational symmetry extending in the long range. The changes are attributed due to the generation of defects caused by doping [32].

2.5.2. Raman Spectra of Mn doped TiO_2 nanoparticles.

The effect of manganese doping on the microstructural changes in nanocrystalline titania is studied by Raman Spectroscopy. Fig.2.14 shows the Raman spectra of undoped and Mn doped TiO_2 nanoparticles.

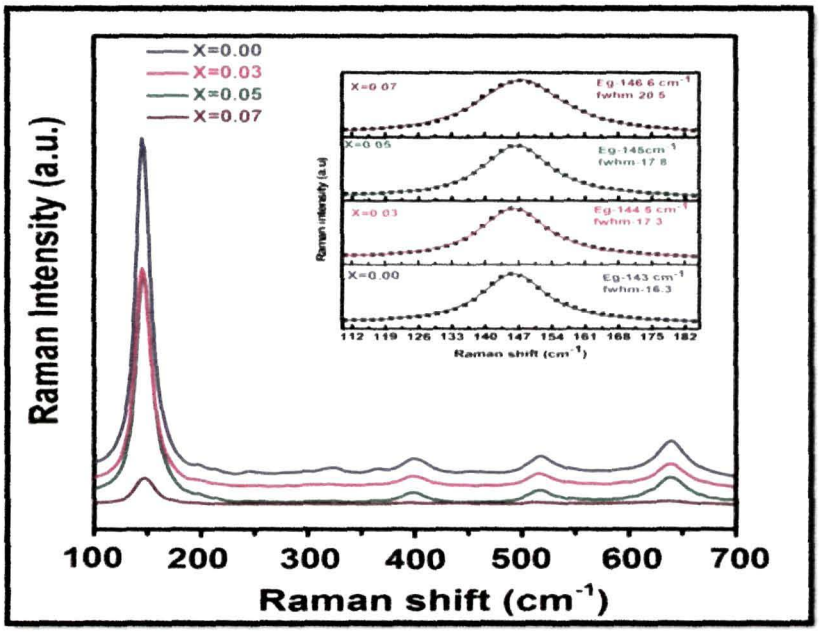

Fig.2.14: Raman spectroscopy of Mn doped TiO_2 nanoparticles. Inset showing shifting of the peaks after doping

All the modes corresponds to the anatase phase [29]. Compared to pure one the most intense E_g Raman peak at 146 cm^{-1} in manganese doped TiO_2 exhibits a decrease in intensity and blue shifting after doping. To have better understanding an expanded view of the Eg peak obtained by Lorentzian fitting is shown in inset of Fig.2.14. This peak is attributed to the O-Ti-O bending vibration and is very much responsive to local oxygen co-ordination surrounding the metal ion [30]. According to Heisenberg's uncertainity principle the relation between particle size and phonon position can be expressed as $\Delta X \Delta P \geq \hbar^2/4$, where ΔX is the particle size and ΔP is the phonon momentum distribution and $\hbar$ is the reduced Planck's constant. As the particle size decreases the phonon is more and more restrained within the particle and the phonon momentum distribution increases. This broadening of the phonon momentum leads to broadening of the scattered phonon momentum according to the law of conservation of momentum. The phonon dispersion causes asymmetric broadening and leads to the shift of Raman lines [33].

2.5.3. Raman Spectra of Gd doped TiO_2 nanoparticles.

Fig.2.15 shows the Raman spectra of pure and Gd doped TiO_2 nanoparticles.

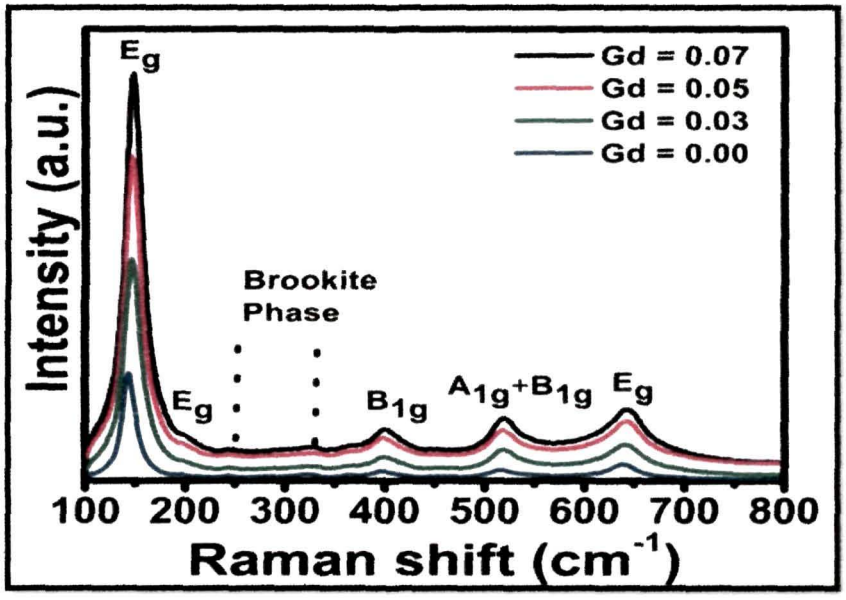

Fig.2.15: Raman spectroscopy of Gd doped TiO_2 nanoparticles.

From the Raman spectra it is evident that the raman peaks of the undoped and doped TiO_2 corresponds to the anatase phase. Appearance of small peaks in the region of 240 cm^{-1} and 320 cm^{-1} corroborates to the brookite phase [34]. No impression of impurity related modes in the Raman spectra are seen in the doped samples. This is in agreement with the XRD result obtained. The E_g peak is mainly caused by symmetric stretching vibration of O-Ti-O in TiO_2, the B_{1g} is caused by symmetric bending vibration of O-Ti-O bond and the A_{1g} is due to the antisymmetric bending vibration of O-Ti-O bond [35]. In undoped TiO_2 the E_g peak appears at 144 cm^{-1}, whereas in 0.03 mol Gd doped TiO_2 the peak is shifted to 147 cm^{-1}. With the increase in Gd^{3+} ion concentration upto 0.05 mol and 0.07 mol the E_g peak position at 147 cm^{-1} however, remains the same. In some transition and other rare earth doped TiO_2 nanoparticles it has been reported that doping generates oxygen vacancies and shifts the peak position to higher wavenumber [36]. But in our case the shifting of the peak position to higher wavenumber is not occurring gradually at each dopant concentration. This behavior may be due to the presence of very few number of gadolinium ions substituting Ti^{4+} in the TiO_2 lattice. A large population of Gd^{3+} ions remains at the surface and therefore, no appreciable shifting in the peak position is observed with increase in dopant concentration. The small peak shifting in the doped samples is likely due to the structural disorder brought about by the substitution of few gadolinium ions in the TiO_2 lattice.

2.5.4. Raman Spectra of Er doped TiO_2 nanoparticles

Raman spectra of the prepared nanoparticles are shown in Fig.2.16. The anatase phase is preserved after doping. The Raman Eg peak becomes asymmetric and blue shifted with the incorporation of dopant ion. This kind of changes in the Raman peak occurs owing to the disruption of local structure and due to the generation of defects on the lattice site of TiO_2 on Er doping

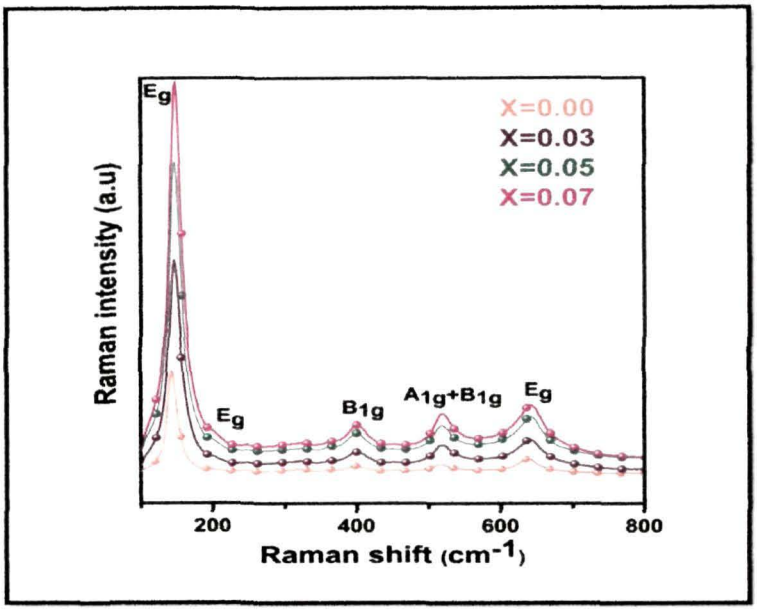

Fig.2.16: Raman spectroscopy of Er doped TiO_2 nanoparticles

Surface area and pore size analysis

Brunauer-Emmett-Teller (BET) serves as an important analysis technique for the measurement of surface area of a material. The technique is based on the exposure of a highly dispersed solid in a closed space to a gas or vapor at definite pressure. The adsorption process proceeds via formation of monolayer first which is than followed by multilayer adsorption and capillary condensation [37]. The specific surface area is calculated from the number of monolayer gas molecules necessary to shield the solid surface, and the cross-sectional area of the gas molecule being adsorbed. The determination is actually carried out at the temperature of liquid nitrogen.

The data are treated according to the adsorption isotherm equation given by

$$\frac{1}{v\left[\left(\frac{P_o}{P}\right)-1\right]} = \frac{1}{v_m c}\left(\frac{P}{P_o}\right) + \frac{1}{v_m} \qquad \text{(2.3)}$$

Where P and P_o are the equilibrium and saturation pressures of adsorbates at the

temperature of adsorption v is the adsorbed gas quantity in volume units, and v_m is the monolayer adsorbed gas quantity, c is the BET constant and can be expressed as:

$$c = \exp\left(\frac{E_1 - E_L}{RT}\right) \quad \text{----------} \quad (2.4)$$

where E_1 is the heat of adsorption and E_L is the heat for liquefaction.

The Surface area and pore size distribution of the samples are acquired with the help of Quantochromei Qautosorbanalyser. The pore size distributions of the samples are ascertained based on Barett–Joyner–Halenda (BJH) model.

2.6.1. Surface area analysis of Gd doped TiO_2 nanoparticles.

Fig.2.17 shows the nitrogen adsorption-desorption isotherm of pure and 0.03 mol Gd doped TiO_2 nanoparticles.

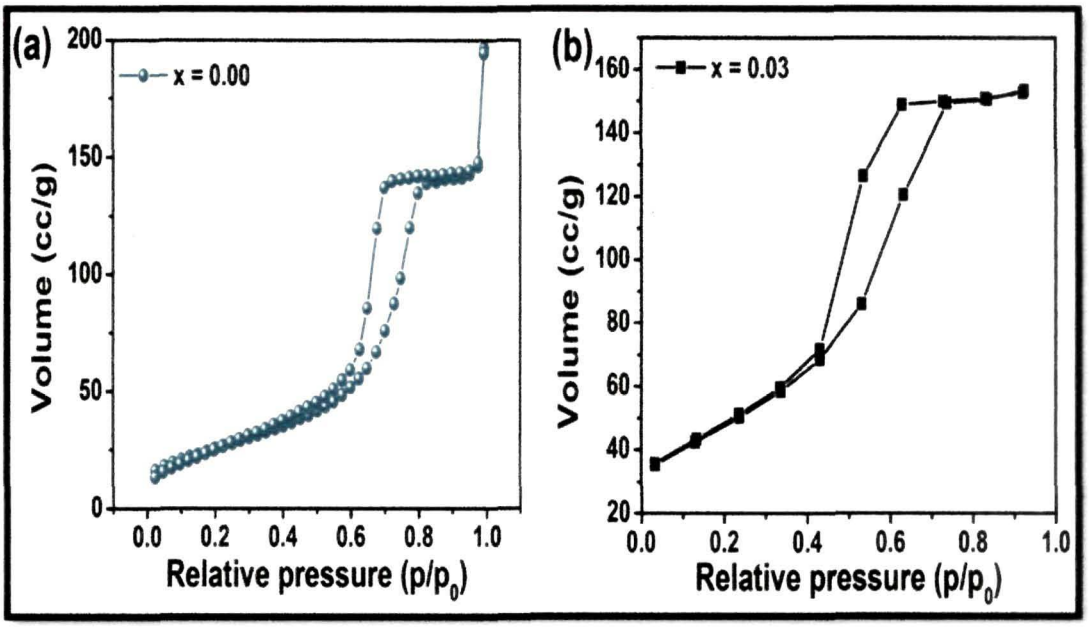

Fig.2.17: Nitrogen adsorption-desorption studies studies of (a) undoped and (b) 0.03 mol Gd doped TiO_2 nanoparticles.

The isotherms are of type IV with H1- type hysteresis loop in the relative pressure range of 0.4-0.8.The type indicates presence of mesopores and are the characteristics of materials containing agglomeration [38].The surface area for 0.03 mol Gd doped TiO_2 nanoparticles is found to be 225 m^2/g which is about 2.2 times the surface area of undoped TiO_2 (95 m^2/g). From the pore size distribution the pore diameter is determined to be 6 nm and 4 nm for undoped and doped sample respectively. The decrease in pore size after doping might be due to the larger size gadolinium ions that causes higher pore filling effect [39].Table.2.3 shows the surface area and pore size of the doped and undoped samples calculated by BET and Barret-Joyner-Halenda methods (BJH). Thus introduction of dopant ion causes a considerable increase in surface area and a decrease in pore size, thereby favoring the criteria for enhanced photocatalytic activity.

Sample	Surface Area (m^2/g)	Pore size (nm)
X=0.00	95	6
X=0.03	225	4

Table.2.3: Surface area and Pore size distribution of all the samples

Optical Characterisation of the prepared nanoparticles

2.7.1. UV-Vis spectroscopy

Ultraviolet-visible spectroscopy (UV-Vis) refers to absorption spectroscopy or reflectance spectroscopy in the ultraviolet-visible spectral region. Different molecules absorb radiation of different wavelengths. When light impinges upon a sample, the light may be totally reflected, as a result of which the substance appears white or light may be totally absorbed in which case the substance appears black. In the thesis the absorption spectra of the samples are monitored in diffuse reflectance (DRS) mode in a Shimadzu 2450 UV-vis

spectrophotometer in the wavelength range from 200-900 nm with a deuterium source for scanning the UV range and a tungsten source for scanning the visible region. The fundamental unit of the spectrophotometer consists of a source (UV and visible), a monochromator, sample container, detector, signal processor and a read out device [40-41]. The monochromator consists of an entrance slit, a collimator that renders the light beam parallel, a prism or grating for dispersing the radiation beam, a focusing lens and an exit slit to isolate the desired spectral band from other dispersed radiation [40-41]. The detector converts the electromagnetic radiation into an electron flow and therefore to a current or voltage flow in the readout circuit [40].

2.7.2. Photoluminescence spectroscopy

Photoluminescence (PL) spectroscopy is a very important tool to investigate the the amount of light radiated by the material on excitation at a particular wavelength. The instrumentation part of a steady state photoluminescence spectrometer consists of a continuous light source for stimulating the material and a collimating lens for collecting the light. The light after passing through a monochromator is collected by a photon detector or photomultiplier tube (PMT). The output signal is routed to a lock in amplifier. Steady state PL analysis of our samples is carried out using Perkin Elmer LS-55 spectrometer with a Xenon light source. The instrument has a scanning range in the visible region spanning from 200-800 nm and the measurement is done at an increment of 0.5 nm.

Unlike the steady state photoluminescence, time resolved photoluminescence spectra is also an important tool to understand the recombination process. Time Resolved photoluminescence spectra (TRPL) of the samples are recorded on a IBH Horiba-Yvon TCSPC using 340 nm Nano LED (FWHM = 750ps) and 375 nm Nano LED (FWHM=300ps) as excitation source for the samples with a time scale of 0.007ns/channel. The decay time is calculated from the slope of a plot of log I (t) versus t, or from the time at which the intensity decreases to 1/e of a value at t = 0 [42].The optical characterization of all the samples are mentioned in the respective chapters.

2.8. Photocatalytic Activity .

Photocatalytic activity of the prepared TiO_2 nanoparticles were studied by examining the degradation of aqueous solution of phenol . For visible light irradiation a 25 watt white lamp was used. In order to carry out the process 50 mg of the photocatalyst was mixed with 50 ml water in a 100 ml beaker. To this mixture 5 mg of phenol was added and the solution was stirred for about half an hour in dark to obtain the absorption-desorption equilibrium The catalyst loaded phenol solution was then placed at a distance of 6 cm and irradiated for 20, 40, 60 and 80 min. After completion of the irradiation process the samples was centrifuged at 10000 rpm to make it free from any catalyst. 5 ml of the aliquot was taken to measure the absorbance. The degradation efficiency was calculated by using the equation:

$$\%D = \left(\frac{A_o - A_t}{A_o}\right) \times 100 \quad \text{---------- (2.5).}$$

A_0 = Initial absorbance and A_t = Absorbance after time t.

2.9. Theoretical method

Theoretical calculation have been performed using density functional theory based MedeA Vienna *Ab Initio* Simulation package (VASP 5.2) on manganese and gadolinium doped TiO_2 nanoparticles. Dopant ion incorporation leads to the creation of trap states within the band gap. The corresponding calculation of density of states indicates formation of these trap states. These trap state delays the electron-hole recombination rate and has some strong correlation in contributing to enhanced photocatalytic activity.

2.9.1. Computational detail of Manganese doped TiO_2 nanoparticles.

A 2x2x1 supercell is built with the unit cell of TiO_2 in anatase form. The undoped super-cell contains 16 atoms of Ti and 32 atoms of oxygen which gives $Ti_{16}O_{32}$, Fig.2.18 (a). The Mn doped TiO_2 takes the form as $Ti_{15}MnO_{32}$ Fig.2.18 (b). The minimum energy state is computed by varying the internal position of atoms until the residual force is 0.01 eV/A^0. The cut off kinetic energy for the structural optimization is set to 400 eV along with the

convergence criterion of 10^{-5}eV. A 3x3x3 K-mesh is used which correspond to spacing less than $0.3(A^0)^{-1}$ in reciprocal space to calculate Density of states (DOS) and band structure; Fermi level is considered to be at 0 eV. The effect of Manganese (Mn) on the TiO_2 system is understood by substituting one centre titanium (Ti) atom by Mn atom and allowing it to relax in all directions.

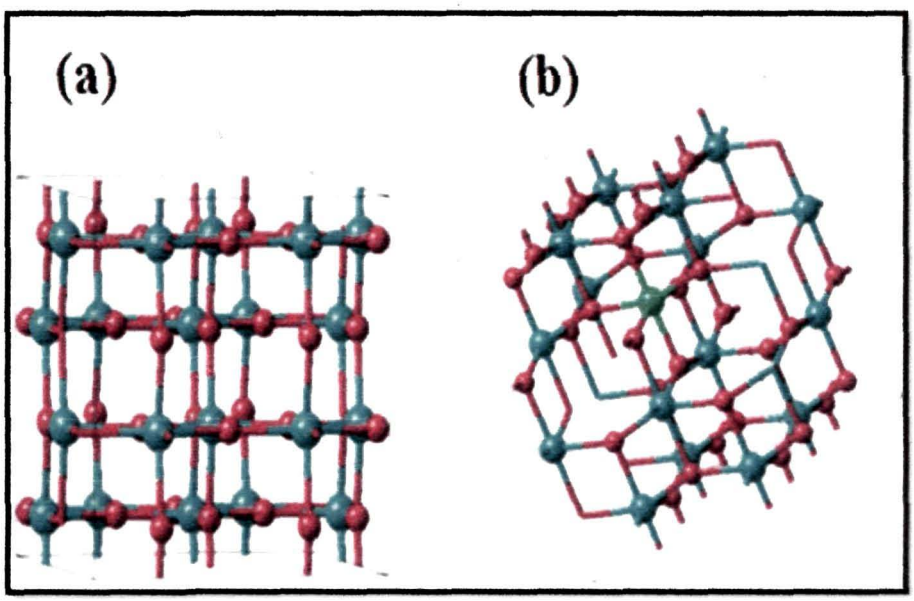

Fig.2.18: Band structure of (a) Undoped TiO_2 (b) Mn doped TiO_2 supercell (2x2x1).

2.9.2. Computational detail of Gadolinium doped TiO_2 nanoparticles.

A 2x1x1 supercell is built with the unit cell of TiO_2 in anatase form. The undoped supercell cell contains 8 atoms of Ti and 16 atoms of O which make it take the form Ti_8O_{16}, Fig.2.19 (a). The Gd doped TiO_2 takes the form as Ti_7GdO_{16} , Fig.2.19 (b). The internal position of the atoms is varied by setting the residual force to 0.01 eV/A^0 for minimum energy calculation. The structural optimization is attained by setting the cutoff kinetic to 400 eV along with the convergence criterion of 10^{-5}eV. A 2x4x2 K-mesh with spacing $0.5(A^0)^{-1}$ is used in reciprocal space to calculate Density of states (DOS) and band structure. The Fermi level is set at 0 eV , in order to describe the electron-electron exchange and correlation effects density functional calculations using generalized gradient approximation (GGA)

with Perdew-Burke-Ernzerhof (PBE) is used. The density functional theory (DFT) equations are solved via projector augmented wave (PAW) method as implemented in Vienna Ab Initio Simulation Package and interfaced with MedeA technology platform.

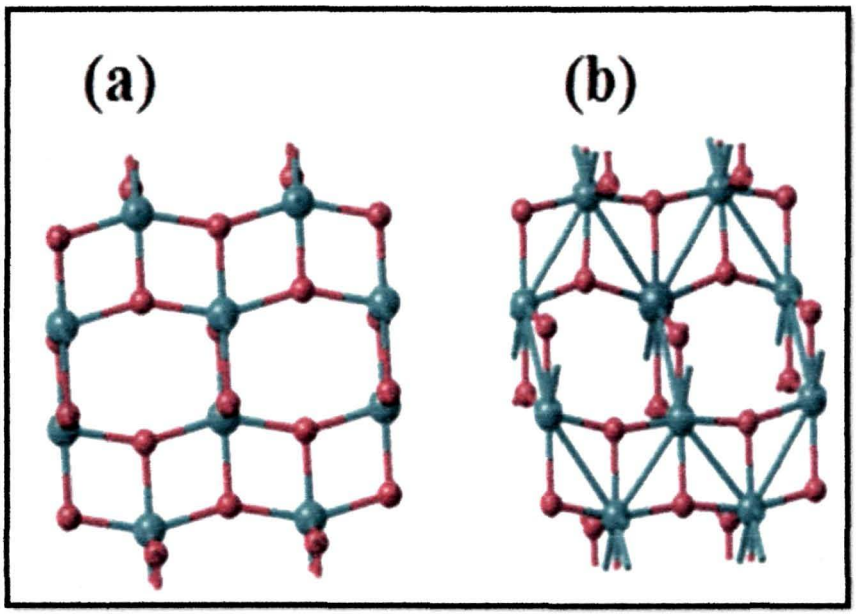

Fig.2.19: Band structure of (a) Undoped TiO_2 (b) Gd doped TiO_2supercell (2x1x1).

References.

1. Kim, J., et al. The Effect of Hydrolysis Temperature on Synthesis of Bimodally Porous Titania, *J. Nanoparticle Res* **2**(4) ,419-424,2000.
2. Sharma, R., et al. X-ray diffraction: a powerful method of characterizing Nanomaterials, *Recent trend in Sci and Technol.* **4** (8),77-79,2012.
3. www.innovationservices.philips.com/sites/default/files/materials-analysis-xrd.pdf.
4. Wang, Y., et.al. Polyol –Mediated synthesis of Ultrafine TiO_2 Nanocrystals and Tailored Physiochemical Properties by Ni Doping, *J.Phys.Chem.* C **113** (21), 9210-9217, 2009.
5. Spurr, R. A., & Meyers,H. Quantitative Analysis of Anatase-Rutile Mixtures with an X-ray Diffractometer , *Anal. Chem* **29** (5),760-762,1957.
6. Hu, K.X., et al., Influence of manganese segregation on the grain size in (Ba,Sr) TiO_3 based ceramics, *Microsc. Microanal* **11**(2), 1728-1729,2005.
7. Dillon, S.J., & Harmer, M.P. Intrinsic Grain Boundary Mobility in Alumina, *J.Am. Ceram. Soc* **89** (12), 3885-3887, 2006.
8. Abazovic, N.D., et al Room Temperature Synthesis and Photocatalytic Activity Of Titania Nanoparticle Doped with Gadolinium ions, *Dig J Nanomater Bios* **8**(2), 871-875, 2013.
9. Chen, Q., et al. Fabrication of uniform Ge-nanocrystals embedded in amorphous SiO_2 films using Ge-ion implantation and neutron irradiation methods, *Appl. Phys.Lett* **98**(7), 073103, 2011.
10. Sharma, P.K.,et al. Doping, strain, defects and magneto-optical, properties of $Zn_{1-x}Mn_xO$ nanocrystals, *Cryst Eng. Comm.* **15** (22), 4438-4447,2013.
11. Dobrzycki, Ł., et.al Structure of YAG Crystals Doped/Substituted with Erbium and Ytterbium *Inorg. Chem.* **43** (24), 7656–7664, 2004.
12. Pal, M., et.al. Effects of crystallization and dopant concentration on the emission behavior of TiO_2:Eu nanophosphors, *Nanoscale Res.Lett.* **7** (1), 1-12, 2012.
13. Neogy,S., et al., Transmission electron microscopy of nanomaterials, *Indian J. Pure and Apl.Physics* **44** (2), 119-124,2006.

14. www.intertek.com/analysis/microscopy/edx/
15. http://serc.carleton.edu/research_education/geochemsheets/eds.html.
16. http://www.ammrf.org.au/myscope/analysis/eds/.
17. Zhang, J.Z *Optical properties and Handbook of nanomaterials*,World Scientific Publishing Co. Pte. Ltd., Singapore, 2009.
18. Yao, Z., et.al. Microporous Ni-doped TiO_2 photocatalyst by plasma electrolytic oxidation, *Appl. Mater. Interfaces* **2** (9), 2617-2622, 2010.
19. Wagner, C.D., et.al. *Handbook Of X-ray Photoelectron Spectroscopy,* Perkin-Elmer Corporation,USA,1978
20. Rath, C., et.al Oxygen vacancy induced structural phase transformation in TiO_2 nanoparticles, *J.Phys D: Appl. Phys* **42** (20), 205101, 2009.
21. Xue, X., et.al Effect of Mn doping on surface enhanced Raman scattering properties of TiO_2 nanoparticles, *Spectrochimica Acta Part A: Mol. and Biomol Spec* **95,** 213–217, 2012.
22. Jhing,L., et.al Effects of Surface Oxygen vacancies on Photophysical and Photochemical Processes of Zn doped TiO_2 nanoparticles and their Relationships, *J. Phys .Chem. B* **110** (36) , 17860-17865,2006.
23. Naeem, M., et.al Effect of reducing atmosphere on the Magnetism of $Zn_{1-x}Co_xO$ Nanoparticles, *Nanotech* **17** (10),2675-2680, 2006.
24. Xiong, L.B., et.al. Ti^{3+} in the surface of titanium dioxide : Generation , Properties and Photocatalytic Application, *J. of Nanomater* **1**,1- 13,2012.
25. Raiser,D & Deville ,J.P. Study of photoemission of some gadolinium compounds, *J.Electron.Spectros and related phenomen* **57**(1), 91-97, 1991.
26. Komuro, S., et. al. Highly erbium-doped zinc–oxide thin film prepared by laser ablation and its 1.54 m emission dynamics, *J.Appl.Physics* **88** (12),7129-7136 , 2000.
27. http://www2.chem.uic.edu/tak/chem52413/notes17/PerkinElmer_Raman20Questions.pdf
28. Colomban,Ph & Slodczyk,A. Raman Intensity: An Important Tool in the study of

Nanomaterials and Nanostructures, *Acta. Phys.Polonics. A* **116** (1), 7-12, 2009.

29. Zhang.J., et.al Relationship between Synthesis Conditions and Photocatalytic Activity of Nanocrystalline TiO_2 , *J. Phys. Chem. B* **110** (2) ,927-935, 2006.
30. Lin,Y.H., et.al Giant enhancement of band edge emission based on ZnO/TiO_2 nanocomposites, *Chen, Opt express* **15** (21),13832-13837, 2007.
31. Choi, H.C., et.al, Size effects in the Raman spectra of TiO_2 nanoparticles, *Vibra. Spectrosc,* **37** (1),33-38, 2005.
32. Minh,N.V., Nano-Particles of Co doped TiO_2 Anatase: Raman Spectroscopy and Structural studies, *J. Korean. Phys. Soc.* **52** (5) , 1629-1632, 2008
33. Xu, Y.C., et.al Blue shift of Raman peak from coated TiO_2 nanoparticles , *J. Raman Spectrosc* **32** (10), 862–865, 2001.
34. Moret, P.M., et.al Brookite-rich titania films made by pulsed laser deposition, *Thin Solid Films* **366** (1), 8-10, 2000.
35. Tian.F., et.al Raman Spectroscopy: A new Approach to Measure the Percentage of Anatase TiO_2 Exposed (001) Facets, *J. Phys. Chem C* **116** (113), 7515-7519, 2012.
36. Pal, M., et.al. Size controlled synthesis of spherical TiO_2 nanoparticles: morphology, crystallization and phase transition, *J. Phys. Chem. C* **111**(1), 96-102, 2007.
37. http://particle.dk/methods-analytical-laboratory/surface-area-bet/surface-area-bet-theory/
38. Kim,S.J., et.al. Preparation and Photocatalytic Activity of Multi-elements Codoped TiO_2 Made by Sol-gel Method and Microwave Treatment , *Carbon letters* **10** (2), 123-130, 2009.
39. Chen, B.,et. al Microstructural and photocatatlytic properties of Eu-doped mesporous titanium dioxide nanopaticles by sol–gel method, *Mater.Res.Bulletin* **47** (11), 3129-3134, 2012.
40. Willard, H.H., Meritt, L.L., Dean, J.A., & Settle, F.A. *Instrumental methods of analysis*, 7th ed., CBS publishers, New Delhi, 2009.
41. http://teaching.shu.ac.uk/hwb/chemistry/tutorials/molspec/uvvisab3.htm.

42. Gaft, M., & Reisfeld, R. *Modern luminescence spectroscopy of minerals and materials*, Springer, New York, 2005.

CHAPTER 3

Monitoring the optical and photocatalytic activity of mixed phase TiO_2 nanoparticles

It is generally accepted that anatase TiO_2 is a better photocatalytic candidate compared to rutile TiO_2 , but recently the anatase-rutile mixture is found to have a magical effect on the charge transfer process [1] .Presence of rutile phase extend the photoactive response to the visible region, harvesting more light. Stabilization of charge separation by electron transfer from rutile to anatase trapping sites slows down the recombination [2], thereby improving the photocatalytic activity. Although there are several methods to prepare nanocrystalline titania but the sol-gel method represents several advantages over other methods [3]. As the method is carried out in solution, tailoring of certain desired structural characteristics such as compositional homogeneity, grain size, particle morphology, and porosity is possible with this method. The process finds wide applications in the development of new materials for catalysis [4] , photochronic applications [5], chemical sensors [6], and also in a diverge range of scientific and engineering fields such as ceramic industry [7], electronic industry [8].

The phase transformation rearranges the bonding arrangement of TiO_2 and introduces many defects in the mixed phase sample. X-ray diffraction, TEM, Raman spectroscopy have been investigated to clearly distinguish the pure anatase and rutile phase, their sizes and defects present. A detailed analysis on the optical properties of the reduced anatase, anatase-rutile mixed phase and of rutile phase is also reported.

3.1. Diffraction pattern analysis of anatase, rutile and mixed phase TiO_2.

The X-ray diffraction pattern of T45, T65, T85 are illustrated in Fig 3.1(a). The XRD pattern of the as prepared powders shows presence of brookite phase at 36° (JCPDS-761934). This phase is usually formed at low temperatures and gets disappeared at high annealing temperatures [9]. A close observation of the diffraction peak reveals that that T45 exists in pure anatase phase. The phase transition began at 650°C and complete transformation

to rutile phase occurred at 850°C, in agreement with earlier results [10, 11] .

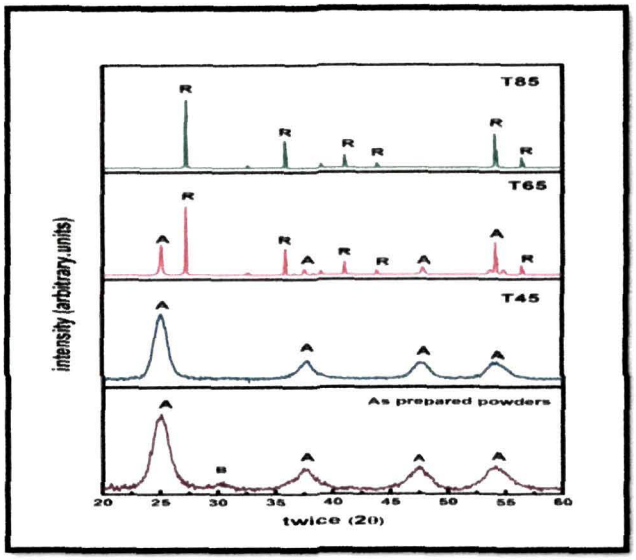

Fig.3.1: XRD pattern of as prepared and T45,T65,T85.

The peaks in the spectra are in agreement with the JCPDS file no 782486 and 894202 of tetragonal systems for pure anatase and rutile phase respectively. The average crystallite size of each samples (Table-3.1) is obtained taking the (101) peak for anatase, (110) for rutile and both (101), (110) for mixed phase using Scherrer's formula.

$$d = \frac{0.9\lambda}{\beta \mathrm{Cos}\theta} \qquad \text{----------} \qquad (3.1)$$

Here d is the crystallite size, λ is the wavelength of the X-ray (Cu Kα= 1.54Å) , β is the full width at half maximum, θ is the diffraction angle. The crystallite size is calculated to be in the nanoregime. A steady increase in size is noticed with increase in annealing temperatures. Presence of anatase and rutile mass fraction of the samples are determined using spurr's formula [12].

$$f_a = \frac{1}{1+1.26\frac{Ia}{Ir}} \qquad \text{----------} \qquad (3.2)$$

$f_r = (1-fa)$ ---------- (3.3)

where f_a and f_r are the anatase and rutile fractions and Ia and Ir are the integrated intensities of the most intense anatase (101) and rutile (110) peak respectively. The parameters calculated by using equation (3.2) and (3.3) are depicted in Table.3.1.

Sl.No	Calcination Temperature (°C)	Crystallite size (nm)		Fraction (%)	
		Anatase	Rutile	Anatase	Rutile
1	450 (T45)	10	0	100	0
2	650 (T65)	36	67	63.4	35.4
3	850 (T85)	-	70	0	100

Table.3.1: Crystallite size, phase composition of the samples calcined at different temperatures.

3.2. TEM study of anatase, rutile and mixed phase TiO_2 nanoparticles.

Fig.3.2a and Fig.3.2b shows the TEM images of T45 and T65 respectively. The average particle size is small in case of pure anatase nanoparticles and increases with its transformation to mixed phase and then to pure rutile phase. For T45 the particle size distribution is within the range of ~ 16 nm while for T65 it is ~ 30-65 nm (Fig3.2b) and for T85 (Fig3.2c) the range is ~ 126- 230 nm. It is thus evident that increase in annealing temperature increases the particle size. The phase transformation begins at the temperature of 650°C and complete transformation to rutile phase occurs at 850°C.The anatase to rutile transformation depends on many factors including the nature of Ti impurities and oxygen vacancies in the TiO_2 lattice. The valence of the impurities being less than Ti^{4+}, oxygen vacancies are created to satiate the charge imbalance. The vacancies cause rupture of the Ti-O bond and results in formation of denser rutile phase [13]. The phase transformation occurs at the grain boundary [14] or within the grains of anatase [15]. Thus the rutile phase nucleates at the grain boundary and grow in size by consuming the surrounding anatase

phase [16]. It is worth mentioning that we have obtained differences in the size calculated from XRD and TEM. The magnitude of the crystallite and particle size agrees well only for the case of stable, monodisperse, single crystals and hard spheres and any deviation from this criteria leads to variation in measured sizes [17].

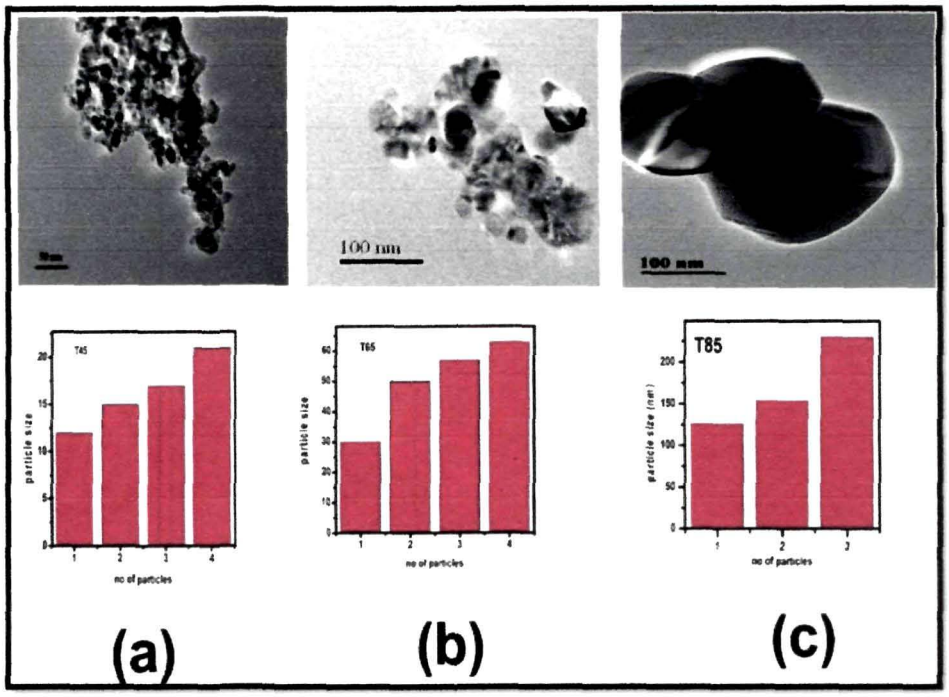

Fig.3.2: Tem images of (a) T45 (b) T65 (c) T85.

3.3. Raman spectra of anatase, rutile and mixed phase TiO_2 nanoparticles.

Raman spectroscopy is further employed in the characterization of crystalline structure of TiO_2 samples. Fig.3.3 shows the Raman spectra of all the samples. Group factor analysis reveals that anatase has six active Raman modes at (A_{1g}+$2B_{1g}$+$3E_g$) [18] and rutile TiO_2 gives four Raman active modes (A_{1g}+B_{1g}+B_{2g}+E_g) [19-21]. In our study in T45 a strong E_g peak appears at 144 cm^{-1} followed by the appearance of low intense peaks at 197 (E_g), 399 (B_{1g}), 513 (A_{1g}+B_{1g}) and 641 cm^{-1} (E_g). All these peaks correspond to the pure anatase phase. For T65 sample E_g peak of anatase remains at 144 cm^{-1} while additional peaks corresponding to the rutile phase appears at 236 cm^{-1}, 448 cm^{-1} , 613 cm^{-1} [22].

In T85 all the Raman peaks are identical to rutile TiO_2. For a perfect crystal the phonon contribution comes from center of the Brilliouin zone satisfying the phonon momentum selection rule, $q \approx 0$ [18]. In semiconductor nanoparticles the phonon selection rule breaks and the phonon momentum distribution increases. The phonon scattering thus involves phonon contribution from the entire Brillouin zone [23,24]. For nanoparticles of diameter (d), the intensity for first order Raman scattering is given by :

$$I(w) = \frac{\int |C(0,k)|^2}{[w - w(k)]^2 + \left(\frac{\Gamma_o}{2}\right)^2} d^3q \qquad \text{----------} \qquad (3.4)$$

Where w(k) is the phonon dispersion curve , r_o is the natural full line width and C (0,k) is the fourier co-efficient of the phonon confinement function and is often in use as:

$$|C(0,k)|^2 = \left(\frac{-k^2 d^2}{16\Pi^2}\right) \qquad \text{----------} \qquad (3.5)$$

Where d is the average size of the nanocrystal. The changes in the Raman peaks are a result of this integration in eqn (3.4) due to changes in grain size [25].

In our study compared to T45 the Eg mode of T65 is slightly red shifted and the fwhm decreases. The phonon confinement model predicts that with the increase in crystallite size the Eg peak is shifted to lower wave numbers and its fwhm and band intensity decreases [26]. Presence of oxygen defects also effects the Raman line , shape and position. The Raman spectra involves vibration of the oxygen atoms only [27]. Temperature treatment changes the local co-ordination of oxygen atoms surrounding Ti^{4+}, and so anatase to rutile phase transformation involves the re-arrangement of TiO_6 octahedra that effects the Raman lines. We have calculated the phonon lifetime via the energy-time uncertainity relation $1/\tau = \Delta E/\hbar = 1/2\pi cr$, [28] where ΔE is the uncertainity in energy, $\hbar$ is the Planck's constant and r is the FWHM of the Raman peaks in cm^{-1}. For T45 and T65 the phonon lifetime using the Eg mode is calculated to be 0.22 ps and 0.57 ps respectively while considering the A_{1g} mode the lifetime for T65 and T85 is found to be 0.10 ps and 0.13 ps respectively. The increased lifetime for T65 is attributed to the generation of

increased defects due to the anatase-rutile contacts. In T85 increase in crystal size adds to the increased phonon distribution further increasing the phonon lifetime [29].

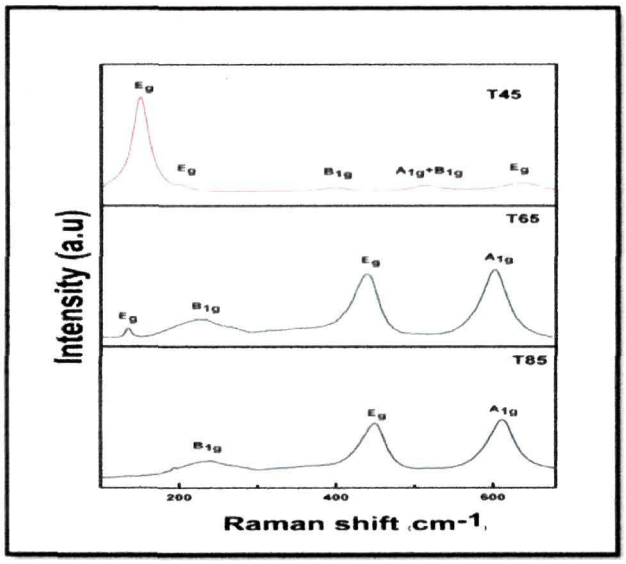

Fig.3.3: Raman spectra of T45, T65, T85

3.4. Surface area analysis of anatase, mixed phase and rutile TiO_2 nanoparticles.

Fig.3.4. displays the typical nitrogen adsorption-desorption isotherm.

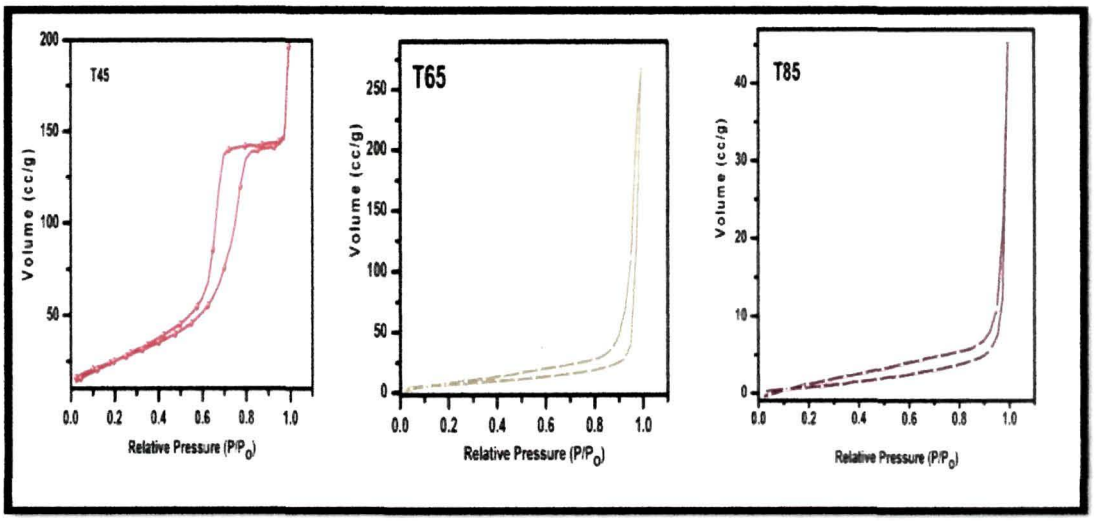

Fig.3.4: Nitrogen adsorption-desorption studies of T45, T65, T85.

From the graph it is observed that the surface area and the pore size distribution exhibits a decreasing trend with the increase in annealing temperatures. The surface area and pore size value of all the samples are given in Table.3.2. The lowering in surface area is attributed to the increase in grain size and particle growth due to high temperature annealing.

Sl.No	Sample	Surface Area (m^2/g)	Pore size (nm)
1	T45	95	31
2	T65	25	5
3	T85	4	3

Table.3.2: Surface area and Pore size distribution of all the samples.

3.5. Absorption spectra, Urbach energy and Band Gap evaluation.

The absorbance curve of all the samples are shown in Fig.3.5

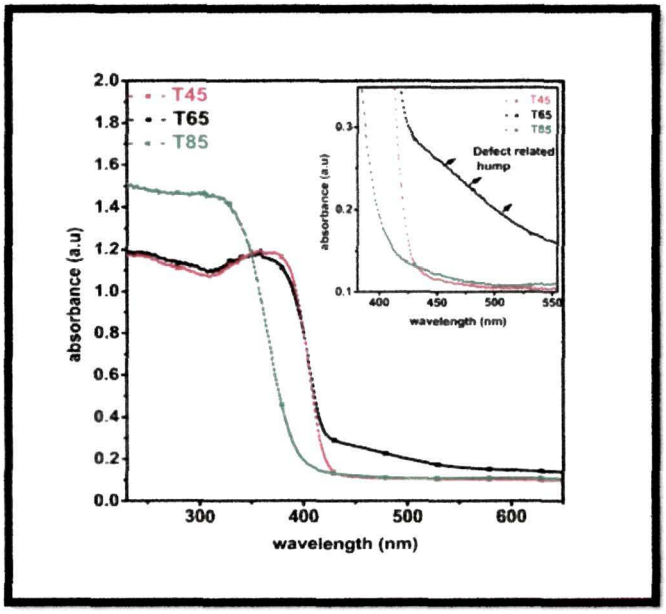

Fig.3.5: Absorbance curve of the samples

The absorption band around 370 nm corresponds to the band to band transition from Ti 3*d* level to O 2*p* levels [30]. Compared to T45, the absorption spectra of the mixed phase sample,T65 shows a hump in the visible region (420-540 nm) (inset,Fig.3.5) coming due to the defects present at the anatase -rutile contacts. For T85 sample an enhancement in the absorption is noticed and this is possibly due to the presence of rutile content that has smaller band gap in comparison to pristine anatase phase [31].

TiO_2 is an indirect band gap material. To quantify the optical band gap, Kubelka-Munk plot is employed. The band gap is evaluated by drawing a line on the linear part of the curve, $[F(R)hv]^{1/2}$ vs hv at $[F(R)hv]^{1/2} = 0$, Fig.3.6.

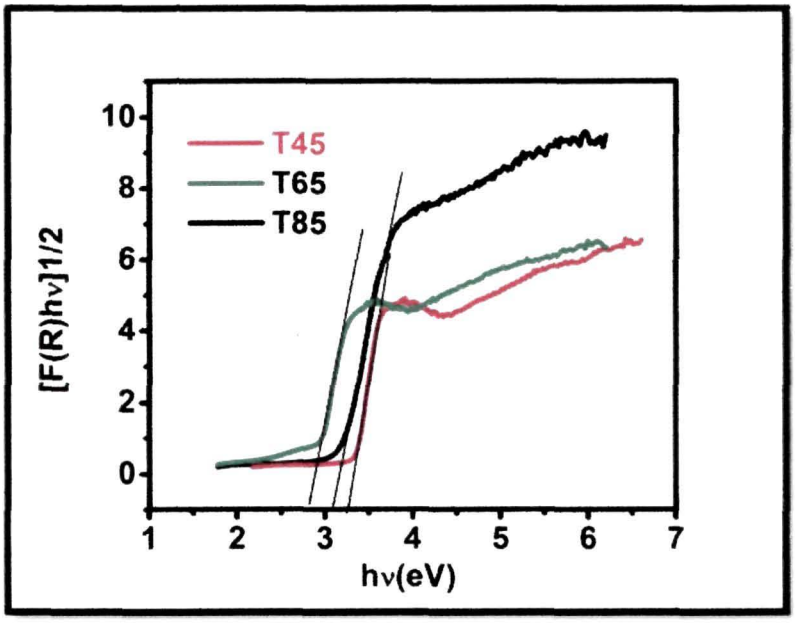

Fig.3.6: Band gap of the samples

The band gap of T45 is slightly higher than that of bulk anatase and this is due to quantum confinement effect. The band gap of T85 matches with the band gap of bulk rutile TiO_2, While T65 has a band gap lower than that of either anatase (3.2 eV) or rutile (3.0 eV) TiO_2. This lowering in the band gap in T65 is due to the presence of defect bands that perturbs the band structure by forming additional states within the band gap in the form of

tails. This tail is referred to as the Urbach tail and the associated energy as the Urbach energy [32]. For the calculation of urbach energy we have plotted ln A (or lnF(R) in DRS mode) vs E (eV), Fig.3.7 (a)-(c).

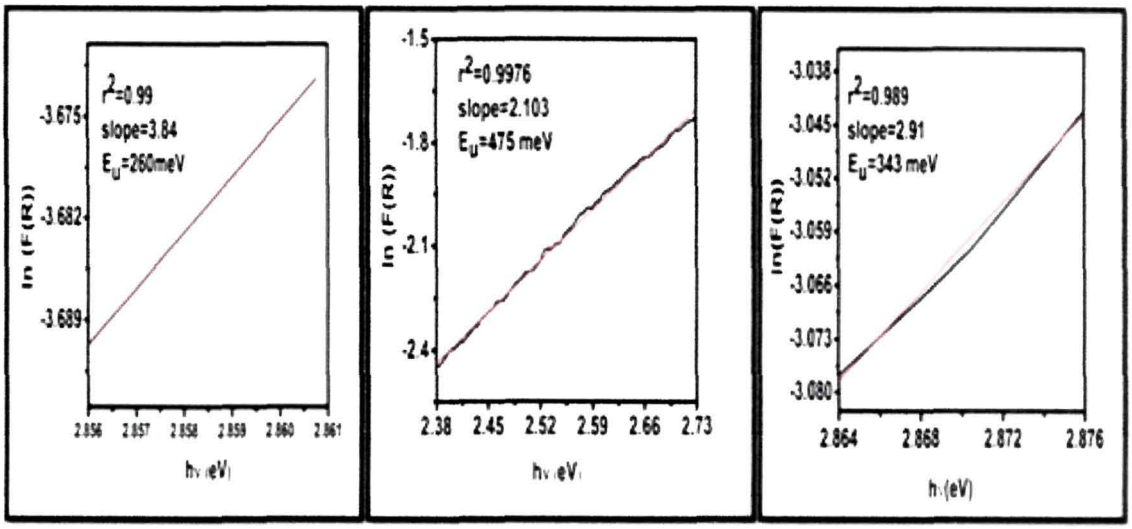

Fig.3.7: Urbach energy of T45, T65, T85.

Table 3.3 gives the band gap and the corresponding Urbach energy of all the samples. The Urbach energy is calculated to be maximum for T65.

Sl.No	Calcination Temp (°C)	Band Gap (eV)	Urbach energy (meV)
1	450 (T45)	3.25	260
2	650 (T65)	2.82	475
3	850 (T85)	3.08	343

Table. 3.3: Band gap and Urbach energy study of the samples calcined at different temperatures

In the TiO_2 nanoparticles Ti^{4+} is surrounded by six oxygen ions forming the TiO_6^{2-} octahedral. High temperature annealing at 650°C alters the arrangement of oxygen ions around Ti^{4+} and generates considerable amount of oxygen vacancies due to breaking of the Ti-O bond. In T65 the anatase and rutile phase being contact with each other the defect by and large localizes at the contact of these two phases. These increases the width of the defect band and in turn increases the Urbach energy. In T85 decrease in oxygen defect density decays the Urbach tail and increases the band gap [33].

3.6. Emission spectra and charge carrier recombination study

Photoluminescence is a very versatile and commonly used tool to disclose the efficiency of charge carrier trapping , immigration and transfer in semiconductors. Fig.3.8 exhibits the PL spectra of the samples at an excitation wavelength of 320 nm (3.87 eV). T45 has an UV emission at 392 nm and is the band edge emission of host TiO_2 arising from X_{1b} transition to Γ_3 [34]. In addition there appears two blue emission peaks at 457 (2.7 eV) and 490 nm (2.5 eV) and one green emission peak at 537 nm (2.37 eV). The peak at 425 nm (2.9 eV) is probably due to the self trapped exciton on the TiO_6 octahedra [1, 35]. However the same peak in rutile TiO_2 is due to recombination of free excitons. The blue emission peak at 490 nm is coming due to the charge transfer transition between from Ti^{3+} to oxygen anion in a TiO_6^{2-} complex associated with oxygen vacancies [36]. Another blue emission peak at 457 nm and green emission peak at 537 nm are due to the color centers associated with oxygen vacancies [37].

The PL emission intensity is contributed by both radiative and non-radiative centres. Radiative recombination increases the emission intensity while non-radiative recombination decreases the intensity. In our study the emission intensity of T65 decreases compared to the T45 sample. The decrease in intensity is due to the presence of defects that act as non-radiative centres. Another reason may be due to the trap to trap relocation of electron until a recombination centre is anticipated. The process restrains the electron-hole recombination and quenches the emission intensity. For T85 sample high temperature annealing removes some of the defects and so the emission intensity increases inferring increase in charge carrier recombination rate compared to T65 sample [38].

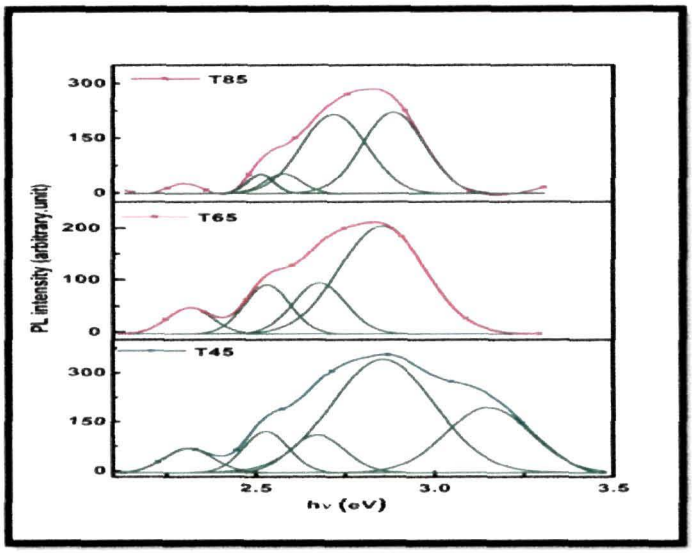

Fig.3.8: PL spectra of the samples with an excitation wavelength of 320 nm.

To have better understanding of the recombination process we have studied the PL decay curve (Fig.3.9) .The curves have been fitted with tri-exp Decay response functions defined by the equation:

$$Y = y_o + A1 * \exp(-\frac{(x - x_o)}{t_1}) + A2 * \exp(-\frac{(x - xo)}{t_2}) + A3 * \exp(-\frac{(x - x_o)}{t_3}) \text{ ---------- } (3.6)$$

Where y_o is the baseline correction, t_1, t_2, t_3 are the decay constants and A1, A2, A3 are the pre-exponential factors. The average decay $<\tau_{avg}>$ time is calculated by using the formula [39].

$$< \tau_{avg} >= \frac{\sum_{i=1}^{i=3} A_i t_i^2}{\sum_{i=1}^{i=3} A_i t_i} \text{ ---------- } (3.7).$$

Using the above equation the average lifetime for T45, T65, T85 are calculated to be 1.99 ns, 2.13 ns and 1.65 ns respectively. T65 has a longer lifetime compared to T45 and T95. The charge carrier lifetime is affected by several factors such as band structure, carrier trapping, mobility of the carriers etc. Anatase TiO_2 being an indirect semiconductor the

conduction band electron and the valence band holes are in different positions in the Brillouin zone [40].The extent of overlapping of the wave function is therefore low. Inclusion of defects within the band gap further lowers the strength of overlapping and increase the lifetime of the charge carriers. Baiju.et.al [41] stated that the charge carriers have a longer lifetime when the anatase and rutile phases are in intimate contact . In case of T85 decrease in lifetime is due to increased recombination process [38].

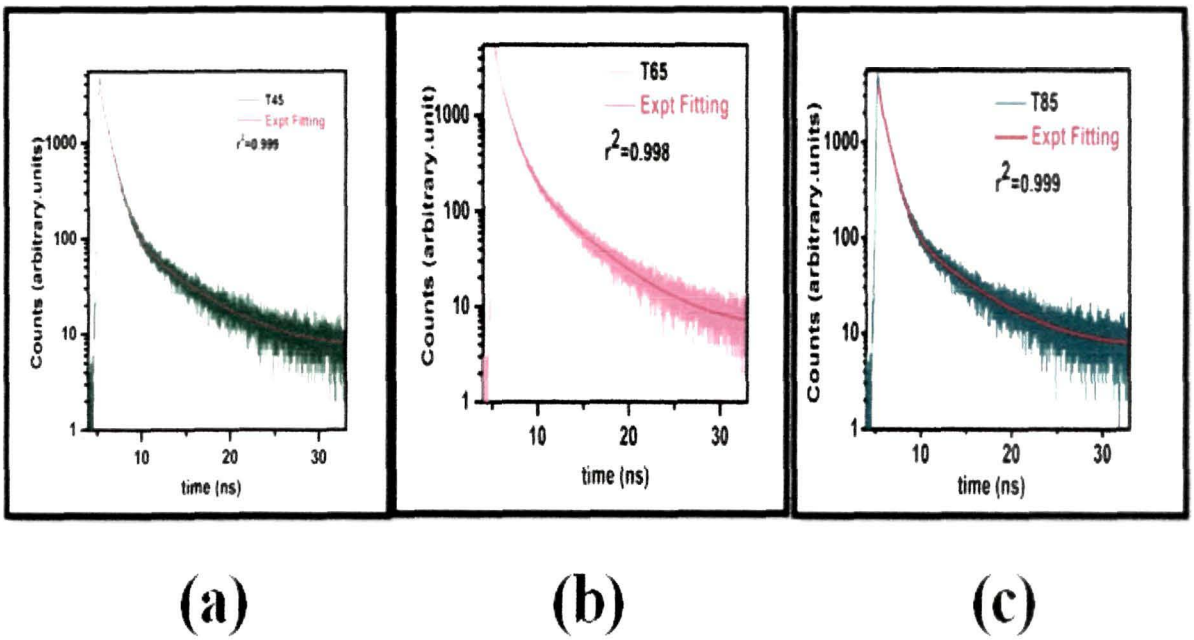

Fig.3.9: Photoluminescence decay spectra

Thus in the present investigation presence of peaks in the visible region, maximum quenching in emission intensity and increased lifetime for T65 samples throws light on the feasibility of the sample to act as a good photocatalytic candidate.

3.7. Photocatalytic activity:

The photocatalytic activity of the samples are evaluated by analyzing the degradation of phenol under visible light.In photocatalysis process after light absorption by host TiO_2 electrons and holes so formed combines with water or OH group and water dissolved oxygen adsorbed on different active sites of the photocatalyst to form the hydroxyl radical

and the super oxide anion. These hydroxyl radical and super oxide anion act as the potential agents in the photocatalytic degradation process.

$$TiO_2 \xrightarrow{hv} e^- + h^+$$

$$OH^- + h^+ \xrightarrow{hv} OH^\bullet$$

$$O_2 + h^+ \xrightarrow{hv} O_2^-$$

$$Phenol + O_2^- \longrightarrow Products$$

$$Phenol + OH^\bullet \longrightarrow Products$$

Fig.3.10 shows the photocatalytic degradation curve. From the graph, T65 is found to exhibit better degradation compared to T45 and T85.

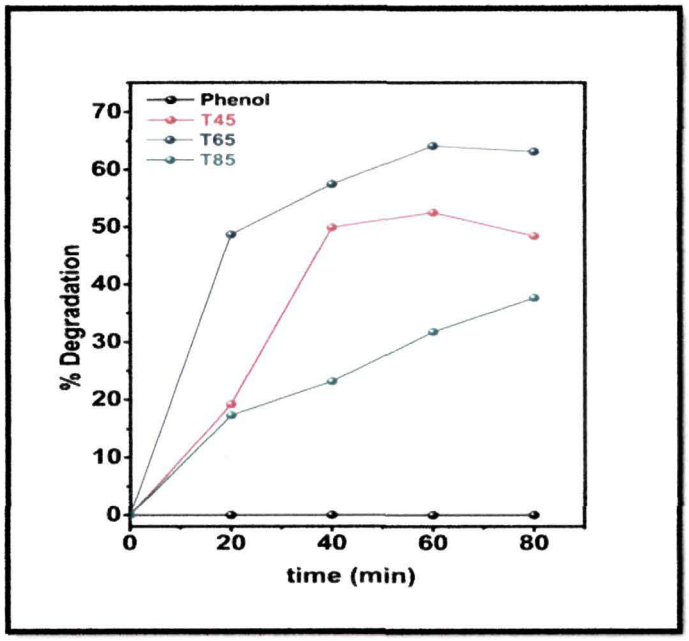

Fig.3.10: Degradation of phenol under visible light irradiation.

Under visible light irradiation the photogenerated electrons rapidly transfer from rutile to lower energy anatase trapping site (Fig.3.11). This leads to a more stable charge separation and in turn contributes to increased photocatalytic activity [2].

It is worth mentioning that although the surface area and pore size in T65 is lower compared to T4 , such high photocatalytic activity is attributed to the intimate anatase-rutile

contacts that generates considerable amount of defects .These defects promote the charge separation and restrain the electron-hole recombination in turn increasing the lifetime of the photo-induced charge carriers as seen from the luminescence decay curve .The generated charge carriers interacts with the phenol before they recombine and hence results in higher degradation activity.

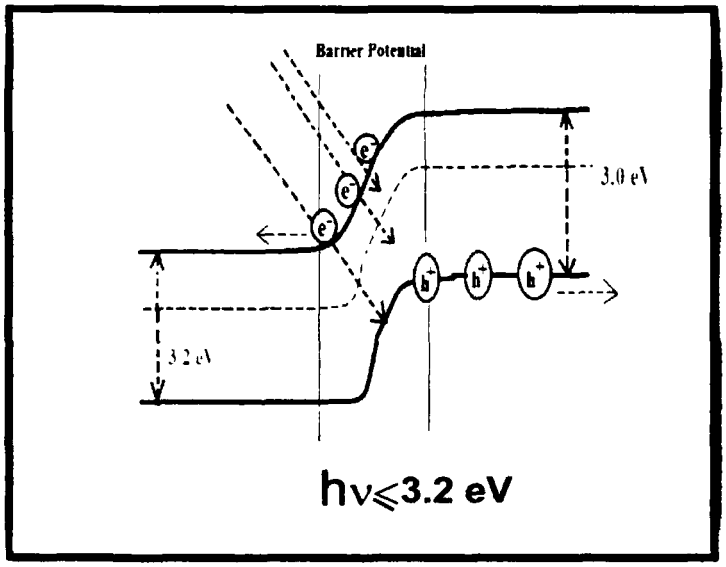

Fig.3.11: Energy band profile with hν< 3.2 eV.

In T85 high temperature annealing removes most of the defects and thereby increases the carrier mobility. The increased carrier mobility induces the increased recombination process and hence lowers the photocatalytic activity [38].

3.8. Conclusion

This Chapter leads to the conclusion that thermal treatment of anatase type titania precursor leads to transformation of anatase to rutile at 650°C. In the photodegradation experiment mixed phase titania (T65) is found to exhibit improved photocatalytic activity compared to pure anatase and pure rutile phase. Such enhancement in the photocatalytic activity is attributed to the formation of defects at the anatase-rutile interface. The presence of these defects lowers the band gap and increases the charge separation thereby , favoring two important criteria for an efficient photocatalytic process

References

[1].Knorr,F.J., et.al. Trap-State Distributions and Carrier Transport in Pure and Mixed-TiO_2: Influence of Contacting Solvent and Interphasial Electron Transfer, *J. Phys. Chem. C* **112** (33), 12786-12794, 2008.

[2].Hurum,D.C., et.al Explaining the Enhanced Photocatalytic Activity of Degussa P25 Mixed-Phase TiO_2 using EPR, *J. Phys. Chem. B* **107** (19),4545-4549, 2003.

[3].Zhou,Z., et.al Photodegradation of Benzoic Acid over Metal-Doped TiO_2, *Ind. Eng. Chem. Res.* **45** (10), 3503–3511, 2006.

[4].Oye,G., et.al Synthesis, functionalisation and characterisation of mesoporous materials and sol–gel glasses for applications in catalysis, adsorption and photonics, *Adv.Colloid and Interface* **123**, 17–32, 2006.

[5].Volkan, M., et.al A sol–gel derived AgCl photochromic coating on glass for SERS chemical sensor application, *Sens. Actuators. B: Chem* **106** (2), 660–667, 2005.

[6].Qiu, G., et.al Recent applications of TiO_2 nanomaterials in chemical sensing in aqueous media, *Sens. Actuators. B: Chem* **160** (1), 875-890, 2011.

[7].Marinel,S., et.al Broadband dielectric characterization of TiO_2 ceramics sintered through microwave and conventional processes, *Ceramic. Int* **39** (1) ,299–306, 2013.

[8].Lin,Y.C., Applying Ag–TiO_2/functional filter for abating odor exhausted from semiconductor and opti-electronic industries *Clean Techn Environ Policy* **15** (2), 359–366, 2013.

[9].So, W.W., et al. The crystalline phase stability of titania particles prepared at room temperature by the sol gel method, *J. Mater. Sci* **36** (17),4299-4305,2001.

[10]. Song,S., et.al. Impacts of Morphology and Crystallite Phases of Titanium Oxide on the Catalytic Oxidation Of Phenol, *Environ. Sci. Technol* **44** (10), 3913–3918, 2010.

[11]. Li,G. H., et.al. The Important Role of Tetrahedral Ti^{4+} Sites in the Phase Transformation and Photocatalytic Activity of TiO_2 Nanocomposites, *J. Am. Chem. Soc* **130** (16), 5402-5403, 2008.

[12]. Spurr, R. A., & Meyers,H. Quantitative Analysis of Anatase-Rutile Mixtures with an X-ray Diffractometer , *Anal. Chem* **29** (5),760-762,1957.

[13]. Pirovanao.,G.V.M et.al Oxygen Vacancies in transition metal and rare earth oxides: current state of understanding and remaining challenges, *Surf .Sci .Report* **62**(6), 219-270, 2007.

[14]. Li, W., et.al Size dependence of thermal stability of TiO_2 nanoparticles, *J. Appl. Phys* **96** (11), 6663-6668, 2004

[15]. Zhang, J., et.al UV Raman Spectroscopic study on TiO_2.I. Phase Transformation at the surface and in the Bulk , *J. Phys. Chem.B* **110** (2),927-935, 2006.

[16]. Rath, H., et al., Effect of thermal annealing on the structure and microstructure of TiO_2 thin films, *Indian J. Phys.* **83** (4), 559-565,2009.

[17]. Baalousha,M., et.al Characterisation of cerium oxide nanoparticles: Part 1 size measurements Environmental toxicology and chemistry, *Environ. Toxicol* **31** (5), 983-993,2012.

[18]. Zhang,W.F., et.al Raman scattering on anatase TiO_2 nanocrystals, *J. Phys. D: Appl. Phys* **33** (8), 912-916, 2000

[19]. Aita,C.R. Raman scattering by thin film nanomosaic rutile TiO_2, *Appl. Phys. Lett.* **90** (21), 213112, 2007.

[20]. Orendorz, A., et.al Phase transformation and particle growth in nanocrystalline anatase TiO_2 films analysed by X-ray diffraction and Raman spectroscopy, *Surf. Sci.* **601** (18), 4390-4394, 2007.

[21]. Mazza.,T.et.al Raman spectroscopy characterization of Rutile TiO_2 nanocrystals, *Phy.Rev* **75** (4), 045416, 2007.

[22]. Narksitipan.S & Thongtem.S Preparation and Characterisation of rutile TiO_2 Films, *J. Ceramic. Process* **13** (1),35-37, 2012.

[23]. Brojčin,M.G.,et.al Infrared study of laser synthesized anatase TiO_2 nanoparticles, *J. Phys. D: Appl. Phys* **38** (9),1415-1420, 2005.

[24]. Mo,S.Di. & Ching,W.Y Electronic and optical properties of three phases of

titanium dioxide : Rutile, anatase and brookite, *Phys. Rev. B* **51** (19),13023-13032, 1995

[25]. Sharma,S., et.al DC magnetization investigations in $Ti_{1-x}Mn_xO_2$ nanocrystalline Powder, *J. Alloy. and Compd* **509** (27) ,7434-7438, 2011.

[26]. Orazem,E.L *Raman spectroscopy on the nanoscale: An investigation of silver triangle arrays, polymer laminates and gold-loaded mesoporous titania films,* Dissertation, University of California at Santa Barbara, U.S, 2007.

[27]. Georgescu,D., et.al Experimental assessment of the phonon confinement in TiO_2 anatase nanocrystallites by Raman spectroscopy, *J. Raman Spect* **43** (7), 876-883, 2012.

[28]. Mali, S., et.al. Hydrothermal synthesis of rutile TiO_2 with hierarchical microspheres and their characterization, *Cryst Engg Comm* **13** (21), 6349-6351, 2011.

[29]. Wang, D., et.al Lattice vibration fundamentals in nanocrystalline Anatase investigated with Raman scattering, *J. Phys.: Condens. Matter* **20** (8), 085212, 2008.

[30]. Devi, L. G. et.al. Enhanced photocatalytic activity of transition metal ions Mn^{2+}, Ni^{2+}, Zn^{2+} doped polycrystalline titania for the degradation of aniline blue under UV/ solar light, *J. Mol. Catal. A, Chem* **328** (1-2) ,44–52, 2010.

[31]. Zhang, Y., et.al Preparation and Photocatalytic Performance of Anatase/Rutile Mixed-Phase TiO_2 Nanotubes, *Catal.Lett* **139** (3-4), 129-133, 2010.

[32]. Lethy, K.J., et.al. Bandgap renormalization in titania modified nanostructured tungsten oxide thin films prepared by pulsed laser deposition technique for solar cell applications, *J. Appl. Phys* **104** (3), 033515, 2008.

[33]. Zhang, H., Effects of thermal treatment under different atmospheres on the spectroscopic properties of nanocrystalline TiO_2, *J. Appl. Phys* **103** (10), 103107, 2008.

[34]. Serpone,N., et.al. Size Effects on the Photophysical Properties of Colloidal Anatase TiO_2 Particles: Size Quantization versus Direct Transitions in This

Indirect Semiconductor, *J.Phys.Chem* **99** (39), 12786-12794, 2008.

[35]. Wan,Y.W., Room-Temperature Synthesis of Single-Crystalline Anatase TiO_2 Nanowires, *Cryst. Growth Des* **10** (4), 1646–1651, 2010.

[36]. Yamada,Y and Kanemitsu,Y Blue photoluminescence of highly photoexcited rutile TiO_2: Nearly degenerate conduction-band effects, *Phys. Rev. B* **82** (11), 113103, 2010.

[37]. Nick,S. Is the Band Gap of Pristine TiO_2 Narrowed by Anion- and Cation-Doping of Titanium Dioxide in Second-Generation Photocatalysts, *J. Phys. Chem. B* **110** (48), 24287-24293, 2006

[38]. Jung, H.S and Kim,H Origin of low Photocatalytic Activity of Rutile TiO_2, *Electron. Matt. Lett* **5** (2), 73-76, 2009.

[39]. Das,K., et.al Morphology Dependent Luminescence Properties of Co Doped TiO_2 Nanostructures, *J. Phys. Chem. C* **113** (33), 14783-14794 ,2009.

[40]. Yamada,Y & Kanemistsu.Y . Determination of electron and hole lifetimes of rutile and anatase TiO_2 single crystals, *Appl.Phys.Lett* **101** (13) , 133907, 2012.

[41]. Baiju,K.V. et.al Correlating Photoluminescence and Photocatalytic Activity of Mixed-phase Nanocrystalline Titania, *Catal.Lett* **130** (1-2), 130-136, 2009.

CHAPTER 4

Exploring the optical, photocatalytic and magnetic property of Ni^{2+} doped TiO_2 nanoparticles

In Chapter 2 we discuss the synthesis procedure of Ni doped TiO_2 nanoparticles. The dopant concentration varying from 0.03 to 0.05 mol. The presence of Ni ions in the host lattice effects the coordination geometry of TiO_2 and thereby influence the physical properties. In this Chapter we will first focus on the modification of TiO_2 nanoparticles due to the added dopant ions. A correlation on the charge carrier recombination and their effect on the photocatalytic degradation of phenol is discussed. In the later part of the chapter the magnetic behavior of the samples are highlighted.

4.1. Effect of Ni doping on optical absorption of TiO_2 nanoparticles

The absorption spectra of undoped and Nickel doped TiO_2 nanoparticles are shown in Fig.4.1. The absorption is obtained from reflectance by Kubelka-Munk equation [1]. The absorption band in the UV region (320-350nm) corresponds to band to band transition from Ti (3*d*) level of titanium (conduction band) to O (2*p*) level of oxygen (valence band). However TiO_2 with different nickel doping levels has a visible light response , ascribed due to typical *d-d* transitions of high spin states of Ni^{2+} ions in the octahedral oxygen co-ordination. The Ni^{2+} ions on substituting Ti^{4+} forms bond with six oxygen atoms. According to the crystal field theory the electrons in the *d* states undergo mutual repulsion and hence splits under the influence of octahedral crystal field of TiO_2 leading to a lower triplet t_{2g} state and a higher energy doublet e_g state. The peak in the visible region (575nm-585nm) is coming from $^3A_{2g}$ to $^3T_{1(g)}(F)$ transition. It has been reported that substitution of Ti^{4+} by d^n metallic ions in the TiO_2 lattice creates allowed energy states in the band gap of TiO_2 and this induces photoactive transitions in the visible region [2]. Hence this type of dramatic optical response clearly indicates that Ni^{2+} ions are substituting Ti^{4+} in the octahedral TiO_2 environment. Thus the UV-Vis spectroscopy is a very important tool to understand the substituting effect of the dopant ion on the host lattice and also its

co-ordination environment therein.

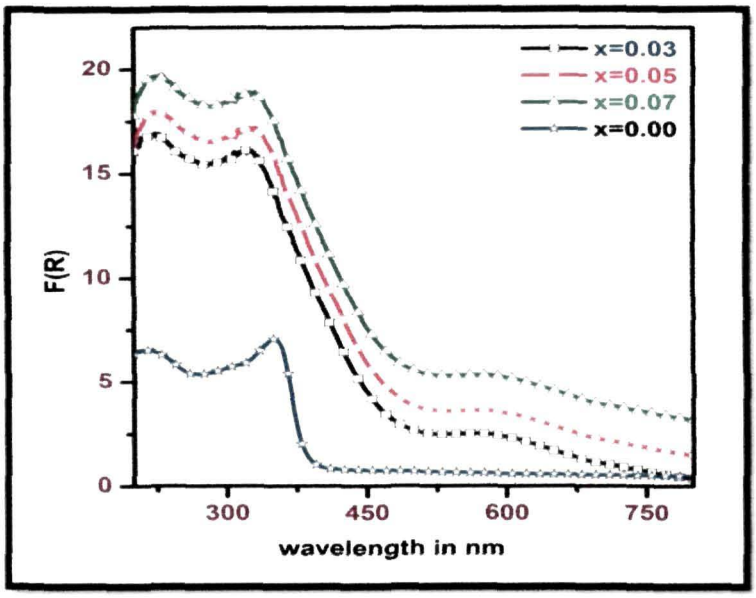

Fig.4.1: Absorption spectra of all the samples.

From UV-vis spectroscopy it is understood that Ni^{2+} forms *d* states in between valence band and conduction band of TiO_2. These states effect the band gap of pure TiO_2. Pure TiO_2 nanoparticles have a band gap of 3.29 eV little bigger than reported value, which may be due to quantum confinemnet effect [2]. This band gap is due to phonon assisted indirect transition from Γ to M in the Brillouin zone [3]. The effective band gap of TiO_2 is reduced to 3.02, 2.96, 3.00 eV on incorporation of 3%, 5%, 7% Ni respectively. The narrowing in band gap after nickel doping is attributed to the charge transfer transitions between the metal ion *d* electrons and the conduction or valence band of TiO_2. However , increase in band gap at 0.07 mol is attributed to the Burstein-Moss effect [4].

4.2. Photoluminescence spectra associated with Ni^{2+} and structural defects.

Fig.4.2 shows the photoluminescence (PL) spectra of pure and Ni doped TiO_2 nanoparticles excited at 320 nm. Gaussian fitting is performed for one of the emission curves (r^2=0.998) for clear observation of the position of different emission peaks. The emission peaks are found to be located at 395, 425, 451 , 488 , 537 nm. The UV emission peak is the near band

edge emission peak [5,6]. According to literature the peak at 425 nm may be ascribed to self trapped excitons located on the TiO_6 octahedra [7,8], while the peaks at 451 nm and 537 nm are ascribed to O_v related trap states [9]. The signature of peak at 488 nm is due to charge transfer transition from Ti^{3+} to oxygen anion in a TiO_6^{2-} complex associated with oxygen vacancy [10].

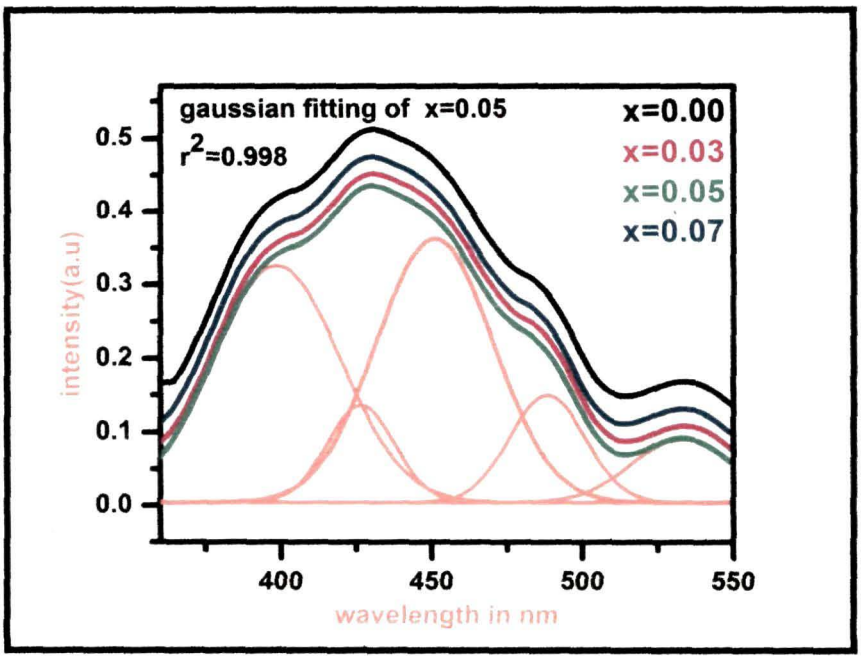

Fig.4.2: (a) Photoluminescence spectra with an excitation wavelength of 320 nm.Gaussian fitting for x=0.05 (r^2=0.998)

From the PL spectra it is understood that doping is neither introducing Ni^{2+} related peak nor is shifting the peak position, only lowering in the emission intensity is noticed. Lowering of emission intensity with increase in dopant concentration infers creation of some non-radiative centers.

To understand the charge carrier recombination process we have studied the luminescence decay spectra of all the samples. Fig.4.3. shows the luminescence decay curve of the samples recorded with an excitation wavelength of 340 nm. The experimental curves have been fitted with tri exponential response functions [11]

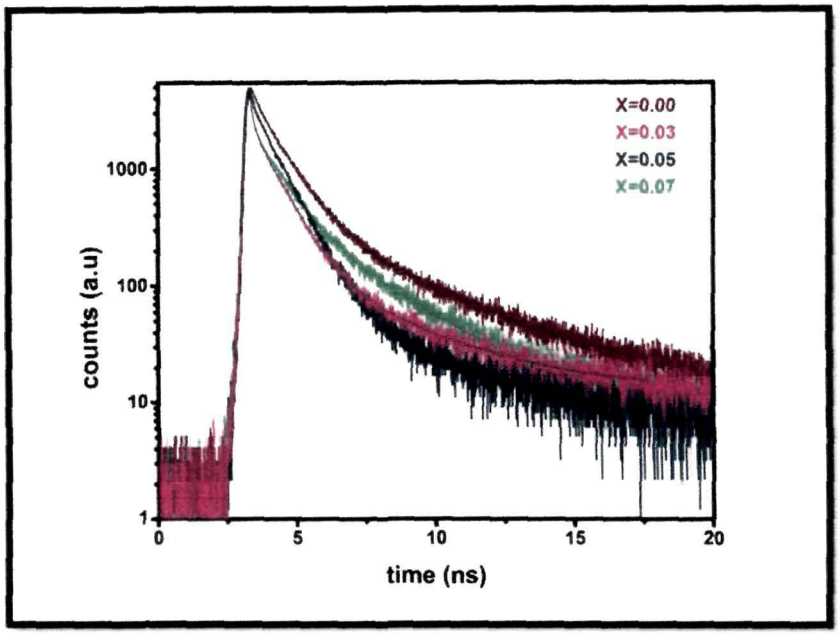

Fig.4.3: Photoluminescence decay curve

The average decay $<\tau_{avg}>$ time is calculated by using the formula

$$<\tau_{avg}> = \frac{\sum_{i=1}^{i=3} A_i \tau_i^2}{\sum_{i=1}^{i=3} A_i \tau_i} \qquad \text{----------(4.1)}$$

In the photoluminescence process the incoming photon results in the formation of electron and holes in the conduction band and valence band respectively. A fraction of the photo-generated charge carriers combine radiatively and gives rise to the near band-edge emission. The fast component τ_3 is due to this near band edge relaxation [11]. The τ_1 component is due to recombination in the shallow traps. The rest of the charge carriers undergo relaxation in the deep trap levels related to oxygen vacancies giving the longer lifetime τ_2 component. There are reports where people have doped transition metal ions in

TiO_2 and found that the *d* states of these metals effectively separate the electron-hole pairs and impart them longer life time for taking part in photocatalytic activity [12]. The oxygen vacancies with trapped electrons act as charged defects. These charged defects interact with the mobile electrons and scatter them thereby decreasing their mobility.

Sample	Decay lifetimes (ns)			Pre-exponential functions			Average time (ns)	Goodness of fit parameter
	τ_1	τ_2	τ_3	A1	A2	A3		
X=0.00	1.2	7.8	0.03	.985	.013	.002	1.71	1.005
X=0.03	1.5	8	0.04	0.965	0.011	0.004	1.86	1.127
X=0.05	2.3	8.8	0.01	0.953	0.012	0.001	1.99	1.118
X=0.07	1.3	7.9	0.04	0.983	0.011	.003	1.72	1.070

Table. 4.1: Best fitted parameters of Multiexponential Components

4.3. Energetics of charge Trapping/Detrapping and photoreactivity in Ni doped TiO_2 nanoparticles.

The photocatalytic properties of TiO_2 are derived from the formulation of photogenerated charge carriers that occur upon the absorption of light. During the process oxygen vacancies and dopant induced defects can become the centers to trap the charge carriers and delay the recombination rate by the following process:

$M^{n+} + e^-_{cb} \rightarrow M^{(n-1)+}$ electron trap

$M^{n+} + h^+_{vb} \rightarrow M^{(n+1)+}$ hole trap.

The energy level for $M^{n+}/M^{(n-1)+}$ lies below the conduction band edge and the energy level for $M^{n+}/M^{(n+1)+}$ above the valence band edge [13]. Introduction of energy levels in the band gap induces red shift and visible light absorption through a charge transfer between dopant and conduction band (or valence band) or a *d-d* transition in the crystal field.

Although it is widely accepted that the photoreactivities of doped TiO_2 are related to the dopant trap site, it is often neglected that for the initiation of photoreactivities the trapped charge carriers must be transferred to the interface. In this framework, the energetic of the charge release and migration in the lattice site is evenly significant as well as the charge-trapping energetics [13].

The efficiency of photodecomposition is affected by several factors such as preparation method, doping concentration, energy level of the dopant within the TiO_2 lattice and the distribution of the dopant in the particle. In Fig.4.4 the photocatalytic degradation of phenol is studied under visible light. The doped samples show much higher photodecomposition activity compared to pure TiO_2.

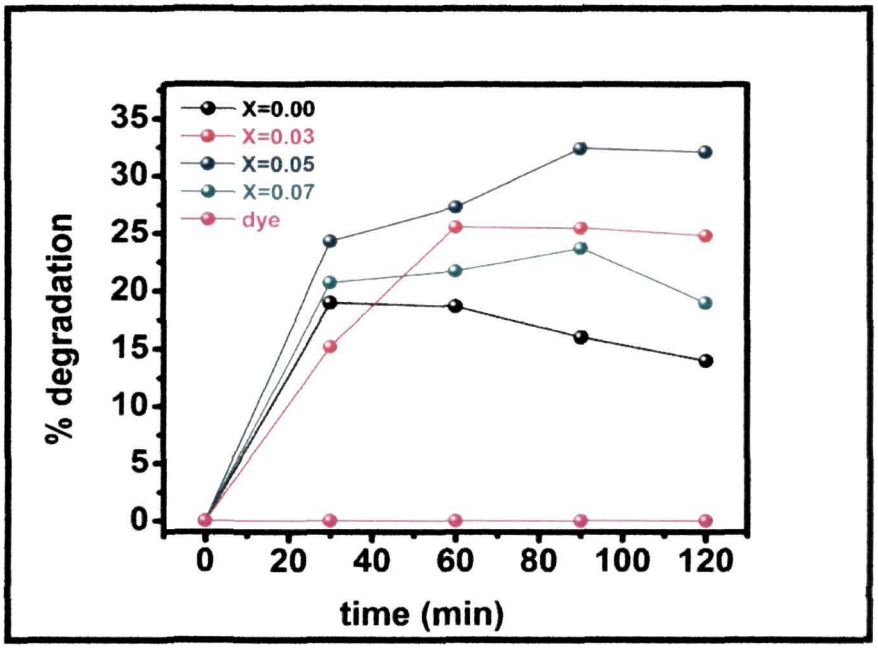

Fig.4.4: Photocatalytic degradation curve

The photocatalytic activity reaches a maximum value when the concentration is 0.05 mol, and again decreases for 0.07 mol of Ni^{2+}. Such high photoactivity may be co-rrelated to the narrow band gap of nickel doped TiO_2 powders that permits photoelectric effect to generate more charge carriers to improve the photocatalyst activity. However the decrease in

activity for x=0.07 mol may be attributed to the thickness (W) of the space charge layer that is inversely proportional to the dopant concentration [13]. Above the optimum dopant concentration W becomes less than the penetration depth of light. Under such circumstances charge carriers undergo recombination very easily making fewer electron and holes to interact with the dye. Moreover at high concentration there is also the possibility that charge carriers may undergo multiple trapping on its way to the surface, due to which their mobility decreases and they undergo recombination before they reach the surface. Hence the net result is that at high dopant concentration the charge carriers act as recombination centre and degrades the photocatalytic activity.

4.4. Magnetic property study

To clarify the doping effect of Ni^{2+} on the magnetic properties of TiO_2 we carried out the room temperature magnetic field dependent magnetization (M-H) measurement of all the samples. Fig.4.5 shows the M-H curve of all the samples. As it is seen pure TiO_2 is diamagnetic in nature.

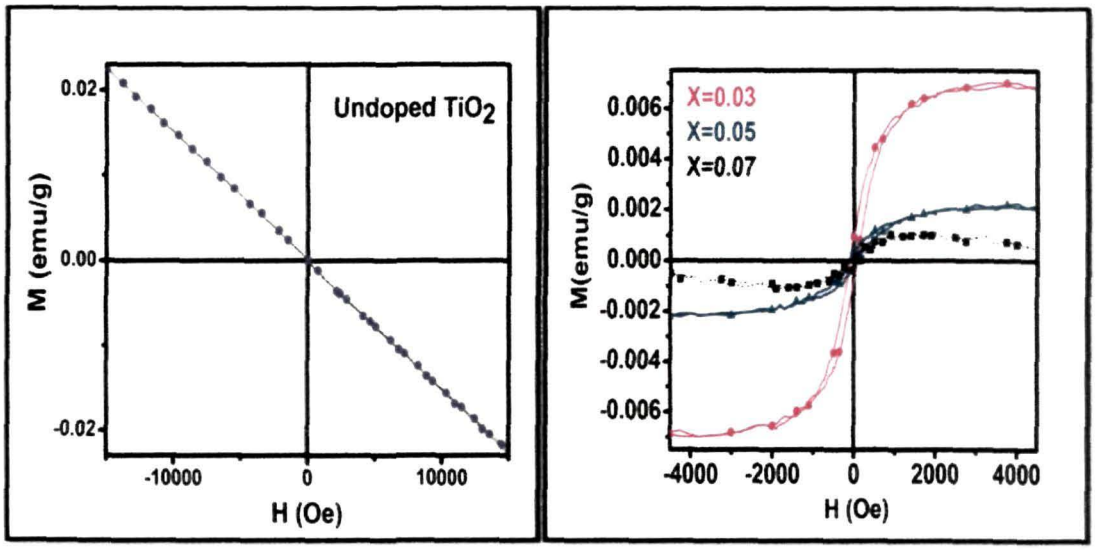

(a) **(b)**

Fig.4.5: Room temperature ferromagnetism of (a) undoped and (b) doped samples

Addition of nickel ions impart magnetism in the otherwise non magnetic TiO_2. There are many reports on ferromagnetism in pure TiO_2 oxide thin films without any foreign impurities. Most of these papers have attributed magnetism due to the presence of sufficient number of oxygen vacancies [14]. The absence of magnetism in our sample indicates non-availability of sufficient number of oxygen vacancies required to induce magnetism. In contrast incorporation of nickel ions generates adequate number of oxygen vacancies and these oxygen vacancies undergo strong exchange interaction with neighbouring nickel ions and imparts magnetism. The magnetization data collected for the sample shows weak ferromagnetic ordering. For 0.03 mol Ni concentration the saturation magnetization is found to be 0.0068 emu/g whereas for 0.05 and 0.07 mol the values are 0.0020 emu/g and 0.00051 emu/g respectively. The saturation magnetization decreases with the increase in dopant concentration. Fig.4.6 presents the Arrot-Belov-Kouvel (ABK) plot for 0.03, 0.05 and 0.07 mol Ni doped TiO_2 nanoparticles. ABK plot signifies the presence of ferromagnetic interaction in a system and measures the spontaneous magnetization [14]. In ABK plot, M^2 is plotted against H/M and the spontaneous magnetization is measured from the intercept of the linear fitting of the curve on Y-axis [14].

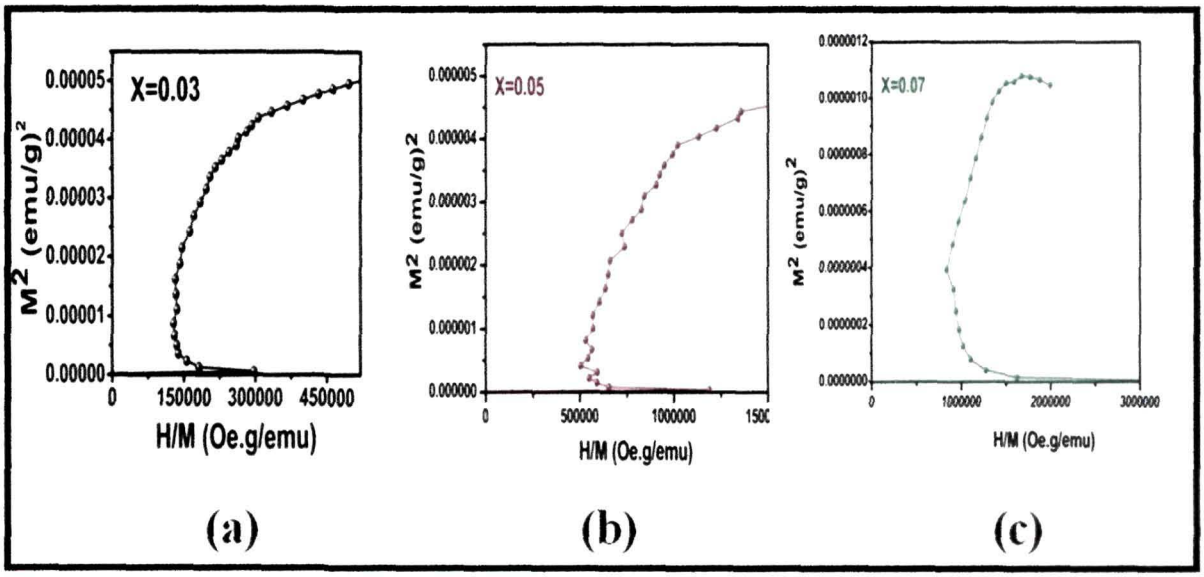

Fig.4.6: ABK plot in order to determine the spontaneous magnetization

The spontaneous magnetization of 0.03, 0.05 and 0.07 mol Ni^{2+} doped TiO_2 are 3.2×10^{-5} emu/g, 2.1×10^{-6} emu/g, 2.4×10^{-7} emu/g respectively. Decrease in the spontaneous magnetization indicates that some antiferromagnetic super-exchange interaction takes place within the neighboring Ni^{2+} ions through O^{2-} ions that leads to reduction of the average moment per Ni^{2+} ions.

The origin of observed ferromagnetism in these nanaoparticles can arise from a number of possibilities, such as NiO , Ni metal, Ni_2O_3 and intrinsic property of doped nanomaterial [15] . Of these Ni_2O_3 is weakly ferromagnetic [16]. NiO in bulk shows ferromagnetism with T_N =520 K [15] and superparamagnetic at nanocrystalline scale [15]. Although Ni metal is ferromagnetic in nature but the nanoparticles are synthesized in air using isopropanol , where Ni metal is unable to exist [15]. Furthermore XRD, XPS , Raman cannot detect the presence of these oxide phases. This infers that the observed ferromagnetism is not due to the presence of these impurity phases. Therefore we can infer that the observed ferromagnetism is intrinsic in nature. The saturation magnetization of our sample is quite low. This is probably because of the weak coupling of Ni^{2+} with the host lattice. A diversity of theories such as Ruderman-Kittel-Kasuya-Yosida (RRKY) and F center bound magnetic polaron or BMP theory is used to understand the mechanism of observed ferromagnetism [17-18]. RRKY theory is mostly applicable in case of metallic system with large number of delocalized free electrons while BMP theory is applicable in case of semiconducting or insulating system with localized free electrons [17]. From the photoluminescence spectra it is inferred that the visible emission peaks are mostly associated with oxygen vacancies. With the increase in dopant concentration, there is an increase in oxygen vacancy with the simultaneous increase in the number of F center. In our system as the electrons are localized in the oxygen vacancy centers, nearby Ni^{2+} F center mediated BMP will be more applicable rather than RRKY. BMP is formed when the electrons locally trapped by the oxygen vacancy interacts the electrons in the *d* shell of Ni^{2+} ions within the diameter of the hydrogen like orbit of F- center [17-18]. Thus large number of F centers and Ni^{2+} overlaps with each other increasing the size of BMP and hence the observed magnetization. The magnetization however decreases for 0.05 and 0.07 nickel

concentrations. Actually when TiO_2 is doped with Ni^{2+}, it is possible that entire Ni^{2+} ions may not be able to bind with oxygen vacancy to form BMP. Some of the nickel ions may bind with oxygen ions forming Ni^{2+}-O^{2-}-Ni^{2+} bonds or some may be associated with other Ni^{2+} ions pairing up themselves. Hence the reduction of magnetization in our system with the increase in dopant concentration may be due to Ni^{2+}-O^{2-}-Ni^{2+} super exchange interaction or due to Ni^{2+}-Ni^{2+} interaction. These interaction leads to anti parallel alignment of the spins and therefore enhance the antiferromagnetic interaction resulting in the effective reduction of magnetization.

4.5. Conclusion

The results can be summarized as follows:

1. In summary it can be concluded that Ni doping tunes the optical property of TiO_2 nanoparticles and enhances the photocatalytic degradation efficiency. PL spectra reveals maximum quenching for x=0.05 mol and at this concentration we are getting maximum photocatalytic activity. However, increased dopant concentration at 0.07 mol degrades the photocatalytic activity. Thus 0.05 mol is the optimum dopant concentration to get better photocatalytic activity.

2. We have observed that the doped samples exhibit ferromagnetic ordering and the ferromagnetism is intrinsic in nature. The magnetism is explained on the basis of BMP theory. The nickel ions which are isolated and form coupled pairs without any oxygen vacancies displays antiferromagnetic interaction and thereby degrades the magnetization as observed with the increasing dopant concentration.

References

[1]. H.Deng, J. M. Hossenlopp, Combined X-ray Diffraction and Diffuse Reflectance Analysis of Nnaocrystalline Mixed Sn (II) and Sn (IV) Oxide Powders, *J. Phys. Chem. B* **109** (1) , 66-73, 2005.

[2]. Kormann, C., et.al Preparation and Characterization of Quantum- Size Titanium dioxide , *J. Phys.Chem* , **92** (18), 5196-5201, 1998.

[3]. Hamberg, I., et.al. Band-gap widening in heavily doped In_2O_3 ,, *Phys. Rev. B* **30** (6) , 3240-3249, 1984.

[4].Fu, C., et.al Theoretical study on the electronic and optical properties of Ce^{3+} doped TiO_2 photocatalysts, *Chem.Phys.Lett* **494** (1-3), 117-122, 2010.

[5].Reddy, B.S., et al. EPR and optical absorption spectral studies of Mn^{2+} ions doped in in potassium thiourea bromide single crystals, *J. Mol. Struct.* **751** (1-3), 161-167, 2005.

[6].Walsh, A., et al. Origins of band-gap renormalization in degenerately doped semi-conductors, *Phys. Rev. B* **78** (7), 075211, 2008.

[7].Preclikova, J., et al. Nanocrystalline titanium dioxide films: Influence of ambient conditions on surface- and volume-related photoluminescence, *J. Appl. Phys* **108** (11), 113502, 2010.

[8].Liu, J., et al. Structure and photoluminescence study of TiO_2 nanoneedle texture along vertically aligned carbon nanofiber arrays, *J. Phys. Chem. C* **112** (44), 17127-17132, 2008.

[9].Kisch, H., et al. A low band gap, nitrogen modified titania visible light photocatalyst, *J. Phys. Chem. C* **111**(30), 11445-11449, 2007.

[10]. Das, K., et al. Morphology dependent luminescence properties of Co doped TiO_2 nanostructures , *J.Phys. Chem. C* **113** (33), 14783-14792, 2009.

[11]. Paul,S.,et.al Effect of manganese doping on the optical property and photocatalytic activity of nanocrystalline titania: Experimental and theoretical investigation, *J.Alloys and Comp.* **583**, 578-586, 2014.

[12]. Das,K., et.al Morphology Dependent Luminescence Properties of Co doped TiO_2

nanoparticles, *J. Phys. Chem C* **113** (33) , 14783-13792, 2009

[13]. Choi, W., et.al The Role of Metal Ion Dopants in Quantum-Sized TiO_2: Correlation Between Photoreactivity and Charge Carrier Recombination Dynamics, *J. Phys. Chem* **98** (51), 13669-13679,1994.

[14]. Choudhury,B & Choudhury,A. Room temperature ferromagnetism in defective TiO_2 nanoparticles: Role of surface and grain boundary oxygen vacancies, *J.Appl .Phys*. **114** (20), 203906, 2013.

[15]. Iqbal, J., et.al Oxygen-vacancy-induced green emission and room-temperature ferromagnetism in Ni-doped ZnO nanorods. *New, J.Phys* **11**, 063009, 2009.

[16]. Lin,Y., et.al. The dependence of Ni-Fe bioxide composites nanoparticles on the $FeCl_2$ solution, *Chem.Cent.J.* **6** (1), 1-7, 2012.

[17]. Coey, J.M.D., et al. Donor impurity band exchange in dilute ferromagnetic oxides, *Nat Mater.* **4** (2), 173-179, 2005.

[18]. Coey, J. M. D., et al. Ferromagnetism in Fe-doped SnO_2 thin films, *Appl. Phys. Lett.* **84** (8), 1332-1334, 2004.

CHAPTER 5

Effect of Manganese doping in tailoring Optical and Photocatalytic properties of TiO_2 nanoparticles and the role of oxygen vacancies in paramagnetic to ferromagnetic transition.

Mn doped TiO_2 nanoparticles was prepared employing a low cost simple sol-gel method. The details of the synthesis procedure has been discussed in Chapter 2. Unlike most of the 3*d* transition metal ion dopant , manganese doped TiO_2 has generated considerable interests as a photocatalyst showing optical response in the visible region and as oxide based dilute magnetic semiconductor showing ferromagnetism at room temperature [1-3]. The phase structure and particle size of the prepared nanoparticles characterized by XRD, RAMAN and HRTEM are discussed in Chapter 2. In this chapter we will first discuss the changes in the absorption and luminescence properties of the nanoparticles after doping. Mn 3*d* states act as a electron trapping states .To justify the creation of these trap states that has some strong correlation in contributing to enhanced photocatalytic activity, we will focus on theoretical calculation based on density functional theory using VASP Software. In the later part of the chapter we will discuss the magnetic properties of the nanoparticles under two different annealing atmospheres.

5.1. Absorption edge shifting to the visible region and understanding the carrier re-combination process.

Optical absorption spectra of the undoped and manganese doped TiO_2 powder recorded in the wavelength region of 200-800 nm is shown in Fig 5.1. The absorbance is found to be minimum for undoped TiO_2 and increases with the increase in manganese concentration. Pure TiO_2 exhibits an absorption peak at 310 nm coming due to transition of electrons from the upper part of the valence band (VB) to the lower part of the conduction band (CB) [4]. Addition of manganese ions in the host lattice add tail states in the visible region. The peak

at (583 nm) is due to $^4T_{1g}$ (G) $\rightarrow$ $^6A_{1g}$ (S) transition [5]. In the anatase phase Ti^{4+} is surrounded by six oxygen ions forming the TiO_6^{2-} octahedra . When Mn^{2+} ions substitutes Ti^{4+} it forms bond with six oxygen atoms. According to the crystal field theory the electrons in the *d* orbital of the manganese ions will experience repulsive forces from the electrons of the surrounding six oxygen atoms. The interaction results in splitting of the *d* orbital to ground state and several excited states, showing the aforestated *d-d* electronic transitions.

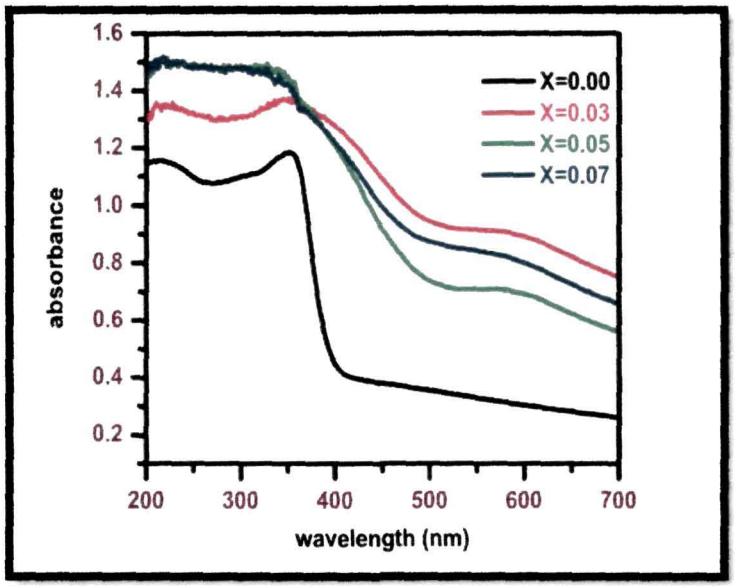

Fig.5.1: Absorbance spectra of all the samples

The band gap of the sample is calculated by extrapolating $[F(R)hv]^{1/2}$ vs hv at $[F(R)hv]^{1/2} = 0$,Fig 5.2(a). Pure TiO_2 shows a blueshift in the band gap (3.43 eV) compared to its bulk counterpart (3.2 eV) due to quantum confinement effect. In chapter 2 calculation of the grain size reveals a decreasing trend with the increase in dopant concentration and hence a blue shift in the band gap is expected. But in the present investigation it is seen that the effective band gap is reduced to 3.01, 2.69, 2.34 eV on incorporation of 3%, 5%, 7% Mn respectively.

The energy band gap of a semiconductor is affected by strain, defects, charge

impurities, grain boundary disorder [6] and particle size confinement [7]. XRD study reported in Chapter 2 reveals increase in strain with the increase in doping concentrations. Fig.5.2 shows variation in the band gap as a function of the lattice strain. A linear decrease in band gap with increase in strain is noticed. Presence of tensile strength results in lattice expansion [8]. Due to such expansion more and more Ti^{4+} ions are replaced by Mn^{2+}. In addition the ionic radii of Mn^{2+} (0.82 Å) being larger than Ti^{4+} (0.61 Å) [9] the TiO_2 lattice must expand in order to accommodate the increasing number of manganese ions. Such lattice expansion enhances mixing of the orbitals and thereby results in the decrease of band gap [10]. A similar decrease in band gap with increase in strain has also been reported for ZnS films prepared by thermal deposition techniques [11] and titania modified tungsten oxide thin films prepared by pulsed laser deposition techniques [10].

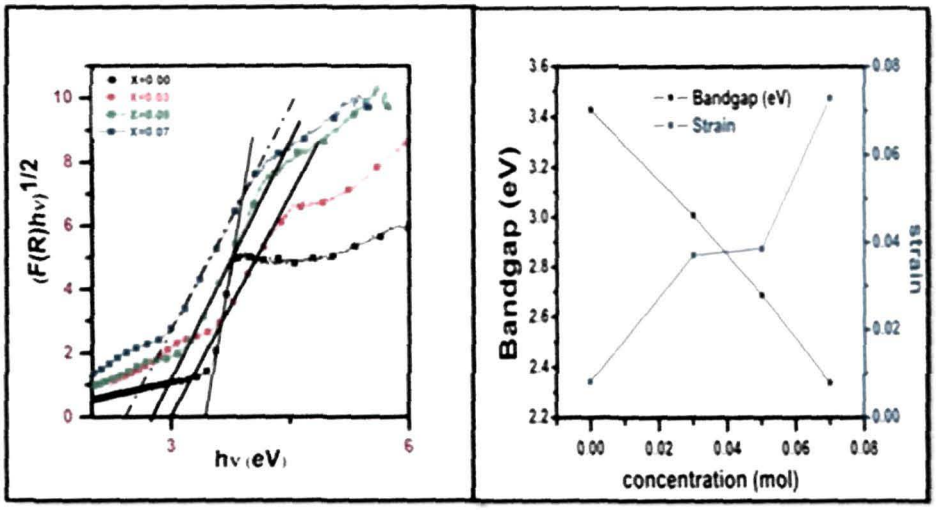

Fig.5.2: (a) Band gap calculation of doped and undoped TiO_2 nanoparticle (b) Variation in band gap, strain with dopant concentration.

Band gap narrowing in TiO_2 due to manganese ion incorporation also points to band gap renormalization effect [10]. According to this effect addition of extra electrons due to

doping leads to an upward shift of the valence band maximum (VBM) and downward shift of the conduction band minimum (CBM) due to stronger hybridization of the electrons of the *d* orbital of the manganese ions with the host conduction band electrons [12]. In doped semiconductor the band structure is perturbed by the presence of impurities. The impurities results in the formation of additional states within the band gap in the form of tails .The strength of the band tail is often characterized by Urbach energy [10]. For the calculation of urbach energy we have plotted ln A (or lnF(R) in DRS mode) vs E (eV). The reciprocal of the slopes of the linear portion below the optical band gap gives the urbach energy. The Urbach energy for each sample is shown in Fig 5.3 (a-d).

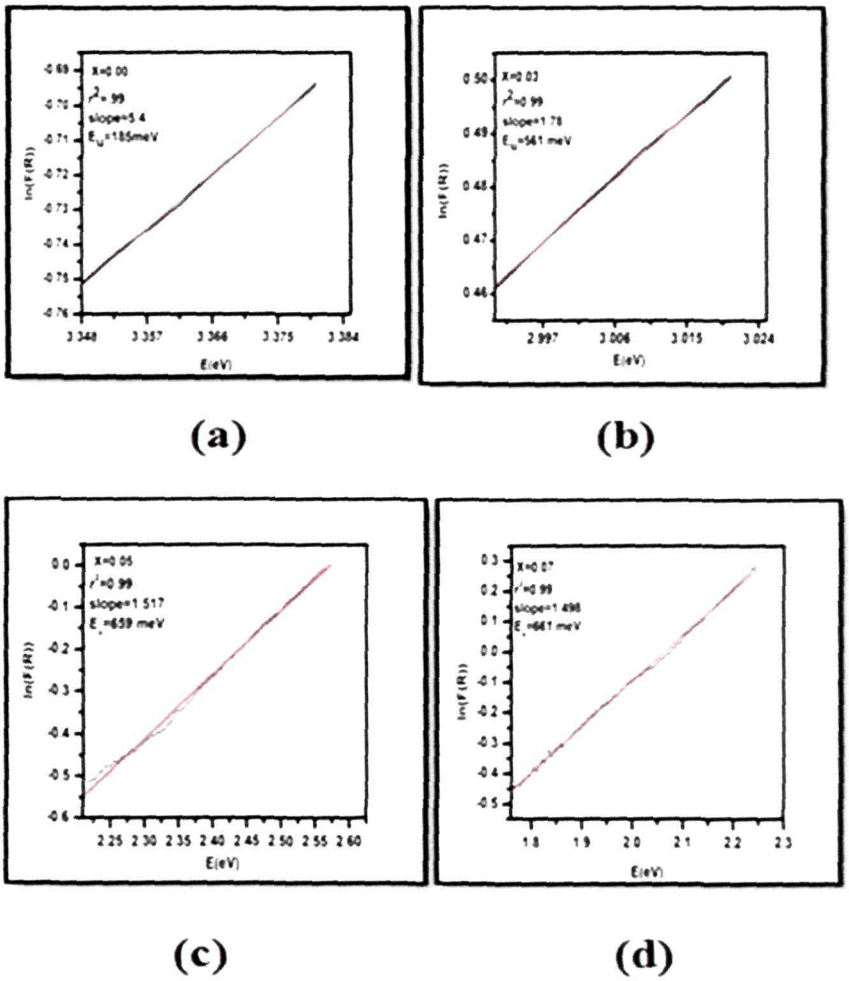

Fig.5.3: Urbach energy of all the samples.

Lethy.et.al reported that the wideness in the Urbach energy with increase in dopant concentration is contributed by dopant impurities, oxygen defects, grain boundary defects [10]. In the present investigation the Urbach energy values calculated for pure and 3%, 5%,7% Mn doped TiO_2 are found to be 185, 561, 659, 669 meV respectively. Thus as the band gap decreases the magnitude of the defect energy increases. The analysis clearly supports formation of sub-band states in between valence and conduction band. Increase in the doping level increases the number of defect levels below the conduction band in such a manner that the band gap shifts in the forbidden gap on one hand and the effective band gap is lowered on the other hand. Although increase in dopant concentration decreases the particle size but there is no increase in band gap due to quantum confinement effect as expected, and this is due to the presence of defect states in the forbidden gap.

The photoluminescence spectra of pure and Mn doped TiO_2 nanoparticle is shown in Fig.5.4 (a). In order to obtain the emission spectra the samples are excited at 320 nm. For clear observation of the emission peaks we have done Gaussian fitting (r^2=0.998) of the emission peaks , Fig.5.4 (b).

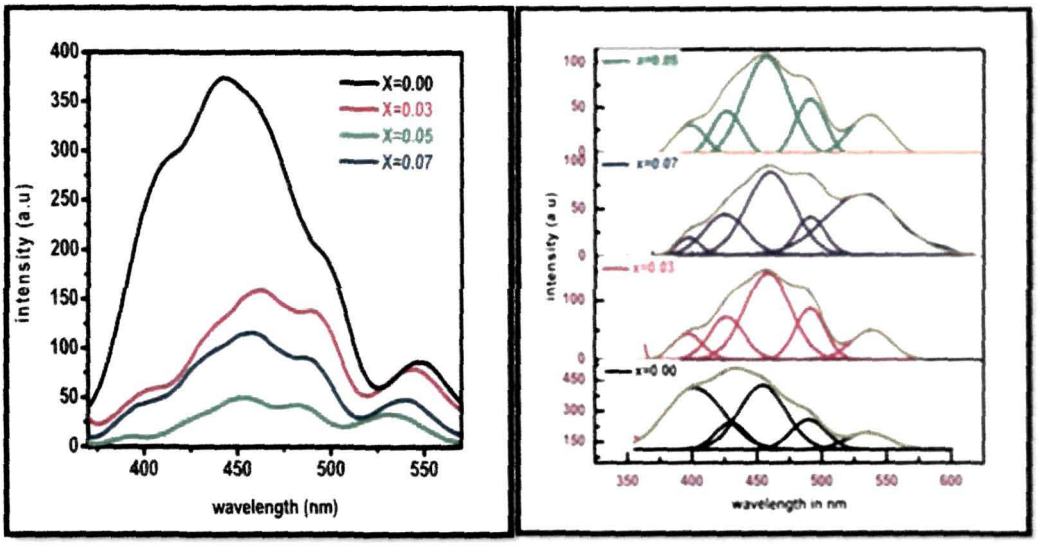

(a) **(b)**

Fig. 5.4: (a) Photoluminescence spectra (b) Gaussian fitting to show various peak positions (r^2=0.998).

All the emission spectra exhibits one UV emission peak at 392 nm (3.16 eV), one violet emission peak at 425 nm (2.9 eV), two blue emission peaks at 457 (2.7 eV) and 490 nm (2.5 eV) and one green emission peak at 537 nm (2.37 eV). The peak in the UV region is the band edge emission peak of host TiO_2 [13]. Commonly PL spectra of anatase TiO_2 are characterized by three types of peak : self trapped excitons, oxygen vacancies and surface states [14]. The peak at 425 nm is probably due to self trapped exciton on the TiO_6 octahedra [15,16]. The blue emission peak at 490 nm is coming due to the charge transfer transition from Ti^{3+} to oxygen anion in a TiO_6^{2-} complex associated with oxygen vacancies [17]. Another blue emission peak at 457 nm and green emission peak at 537 nm are due to the color centers associated with oxygen vacancies [18]. A very interesting feature is the emissivity of TiO_2 in the UV region. The intensity is considerably less compared to visible region which is even more less in the doped samples. Anatase TiO_2 consists of interconnected TiO_6 octahedra , each octahedra is in contact with eight more neighboring atoms by four edge and four corner sharing atoms. The octahedron is highly distorted. Addition of manganese ions in the lattice introduces more distortion due to difference in the ionic radii of Ti^{4+} and Mn^{2+} [19]. Introduction of dopant ion thereby distorts the structural quality and band structure of host lattice by forming large number of defects. These defects are responsible for enhanced visible emission intensity of the material compared to UV emission [19]. A close analysis of Fig.5.4 (b) indicates that the peak positions in case of doped samples are slightly red shifted compared to the undoped one , indicating band gap narrowing caused by doping which is in consistent with the band gap calculation from the UV-Vis spectra [20]. Another important feature is the quenching in emission intensity noticed for all the doped samples. This quenching in emission intensity is attributed to the presence of oxygen vacancies that act as non-radiative centers.

To further understand the recombination process of the photogenerated charged carriers time resolved photoluminescence measurements were taken. Fig 5.5 shows the PL decay curve of the samples (x=0.00, x=0.05) recorded with an excitation wavelength of 320 nm. The experimental curves have been fitted with tri exponential response functions [21]. The best fitted parameters of A_i and t_i (i=1,2,3) for pure TiO_2 and Mn^{2+} doped TiO_2 are listed in Table.5.1.

The average decay $<\tau_{avg}>$ time is calculated by using the formula [19]

$$<\tau_{avg}> = \frac{\sum_{i=1}^{i=3} A_i t_i^2}{\sum_{i=1}^{i=3} A_i t_i} \quad \text{----------(5.1)}$$

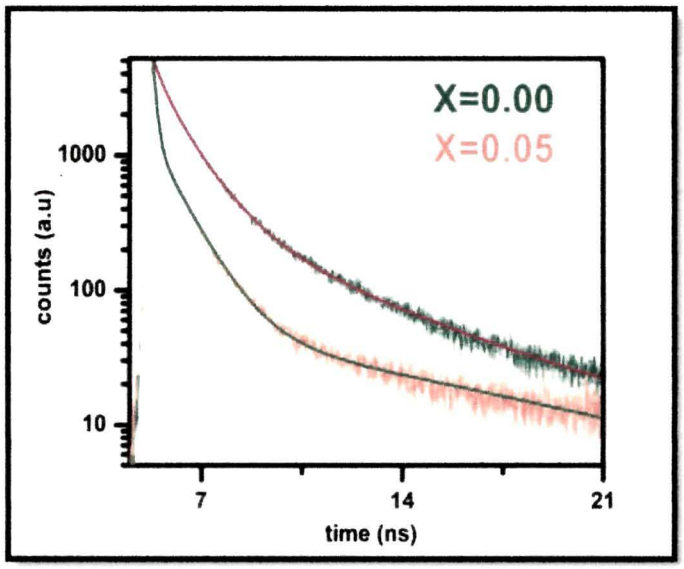

Fig.5.5: Photoluminescence Decay curve .

Sample	Pre-exponential functions			Decay life time			Goodness of fit parameter
	A1	A2	A3	τ_1	τ_2	τ_3	
X=0.05	54.496	2735.51	13091.72	8.396	1.042	.155	.997
X=0.00	3773.64	129.95	5330.45	.998	6.788	.180	.998

Table. 5.1: Best fitted parameters for x=0.00 and x=0.05 mol Mn doped TiO_2 nanoparticles

Using equation 5.1 undoped TiO_2 is calculated to have an average life time of 1.75 ns while for 5% Mn^{2+} doped TiO_2 it is 2.28 ns. Thus the lifetime of doped TiO_2 is longer compared to undoped one. The electrons and holes in undoped TiO_2 are confined within a very small region, the extent of overlapping of the wavefunction is more leading to faster

recombination [20]. But in case of doped samples introduction of the dopant states into the mid gap of TiO_2 restrains the degree of overlapping of the charge carriers thereby imparting them longer lifetime. In undoped TiO_2 electrons from the conduction band after relaxation in the defect state directly transits to the valence band undergoing faster recombination with the holes. But in doped samples due to the presence of oxygen vacancies electrons donot directly jump to the VB to combine with the holes. Manganese doping introduces some energy levels of *d*-states splitted by crystal field near about oxygen and Ti^{3+} related trap states. Therefore compared to pure one in doped system trap to trap transition of electron takes place from the defect levels to Mn *d* states. The electrons relaxes in these *d* states from where they transit to the ground state . The process imparts moderately longer lifetime of the charged carriers in the doped sample.

5.2. Theoretical Study

$Ti_{16}O_{32}$ and $Ti_{15}MnO_{32}$ supercell are tested with spin polarized calculation. Band structure and total density of states (TDOS) are calculated for both the systems as shown in Fig.5.6 (a-b) and Fig.5.7 respectively.

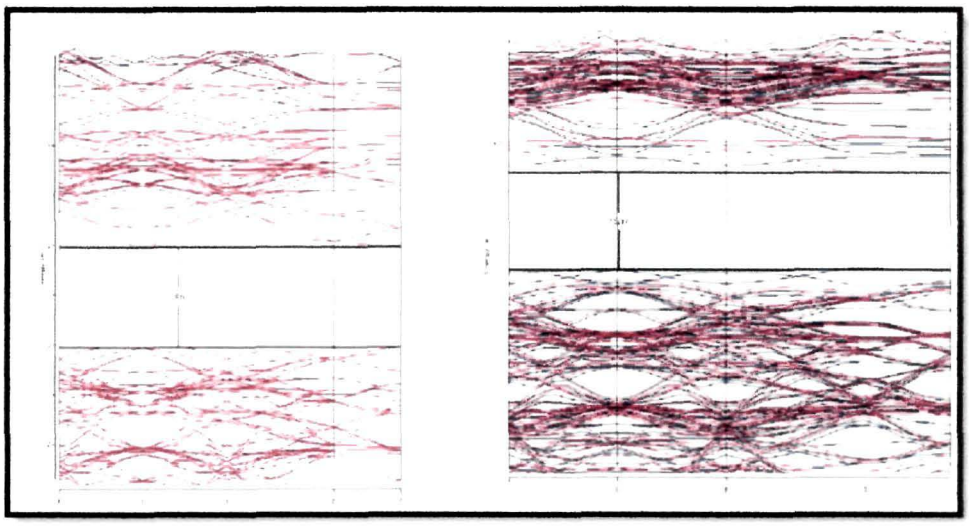

(a) **(b)**

Fig.5.6: (a) Band structure of pristine and (b) Mn doped TiO_2 supercell

Standard DFT calculation though could not determine the actual band gap but still we can frame out the changes in band gap of Mn doped TiO_2 system with respect to pristine TiO_2 system. It is observed from the band structure that the band gap is reduced after Mn doping.

The DOS sketch shows that Mn create levels above the V.B. and also a coupling between Mn 3*d* and Ti 3*d* levels is observed in the C.B. region. These coupling suggest transfer of electrons from Mn 3*d* to Ti 3*d* levels. Presence of Mn ions in the host lattice therefore not only reduces the effective band gap but also provides metastable state in the form of Mn 3*d* levels for V.B. electrons to relax during the transition of electrons from top of the V.B. to the bottom of the C.B. As a result the energy required to excite electrons for photocatalysis is lower in Mn doped TiO_2 compared to undoped TiO_2 [22]. These states can be termed as electron trapping centre that enhances the photocatalytic needs [23].

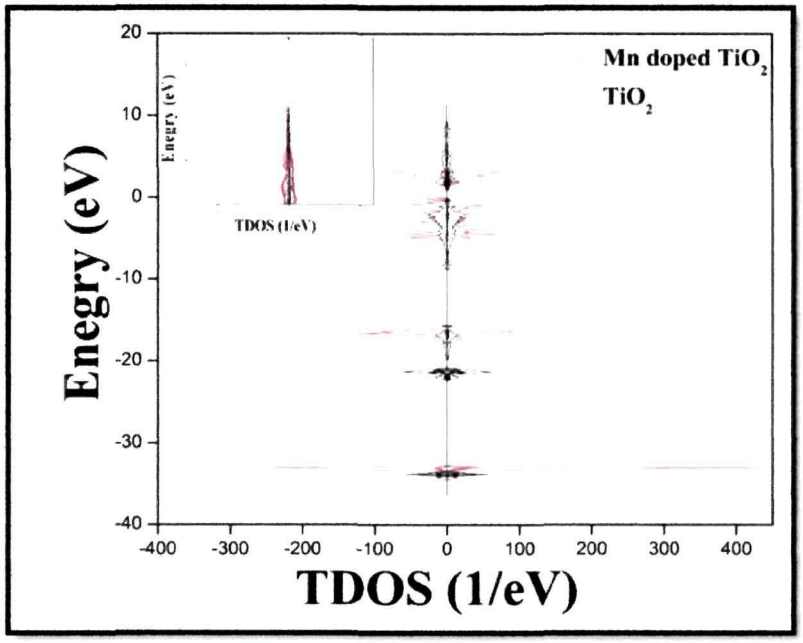

Fig.5.7: TDOS of pristine and Mn doped TiO_2.

5.3. Photocatalytic Activity:

The photocatalytic activity is studied on aqueous phenol. As the phenol solution is prepared in water, so in contact with the photocatalyst surface the water or hydroxyl group and

water dissolved oxygen are adsorbed on its various active sites. The oxygen vacancy centers detrapps effortlessly and reposite the electrons and holes on the surface of TiO_2. The adsorbed oxygen on the surface by accepting an electrons gets reduce to superoxide radical while the surface hydroxyl group translates into hydroxyl radical [24]. These superoxide and hydroxyl radical are the potential oxidizing agents for efficient degradation of phenol. The phenol solution with the catalyst loading was irradiated with visible light and the results are depicted in Fig.5.8. It is seen that undoped TiO_2 exhibits the lowest phenol degradation under visible region, while the degradation increases on increasing manganese content upto 0.05 mol and thereafter again decreases at 0.07 mol of Mn^{2+}. Undoped TiO_2 has maximum absorption in the UV region , so illumination of this catalyst under visible light does not produce sufficient number of electrons and holes for phenol degradation. On manganese doping , due to presence of Mn^{2+} *d* states the absorption edge is shifted to the visible region, the band gap is narrowed allowing maximum absorption of light in the visible region. The dopant cation related trap states and oxygen vacancies restrains the recombination rate of photogenerated electrons and holes and enhances the photocatalytic activity of TiO_2.

From Fig.5.8 it is seen that the degradation rate of the samples for x=0.03 very slowly increases on increasing the irradiation time. The degradation being nearly equal to that of undoped TiO_2. However for TiO_2 with x=0.05 mol the degradation is very fast upto 60 min and maximum degradation is obtained at this concentration. In the present investigation emission intensity is quenched maximum at x=0.05 mol , indicating efficient separation of charge carriers and increased lifetime of the charge carriers further supported by luminescence decay curve. Both these factors contribute to enhanced photocatalytic activity at this concentration, indicating inherent relationship between photoluminescence and photocatalytic activity. But this is not applicable for all samples under all environment . Xiao.et.al [25] in his study with Sm^{3+} doped TiO_2 reported that samples showing stronger PL exhibits stronger photocatalytic activity. But in our case x=0.05 mol is showing lowest luminescence intensity and maximum photocatalytic activity. For the manganese concentration of 0.07 mol, the photocatalytic activity decreases. The decrease in activity

can be correlated to the thickness of the space charge layer (W) that is inversely proportional to the dopant concentration (N) [26]. Due to increase in dopant concentration above an optimum level the thickness of the space charge layer becomes less than the penetration depth of light. Under such circumstances the charge carriers undergo recombination effortlessly, making available fewer number of electrons and holes to interact with phenol. From the degradation curve it is seen that the degradation rate increases with the increase in irradiation time upto 60 min, while increase in irradiation time upto 80 min shows a slight decrease . Although longer irradiation time generates larger number of charged carriers due to the availability of more number of charge carriers, but these charge carriers after a certain point of time travels to the surface region and cover it up. The negatively charged surface prevents the active species (oxygen anion and the hydroxyl radical) accountable for phenol degradation and eventually decreases the degradation rate of the catalyst.

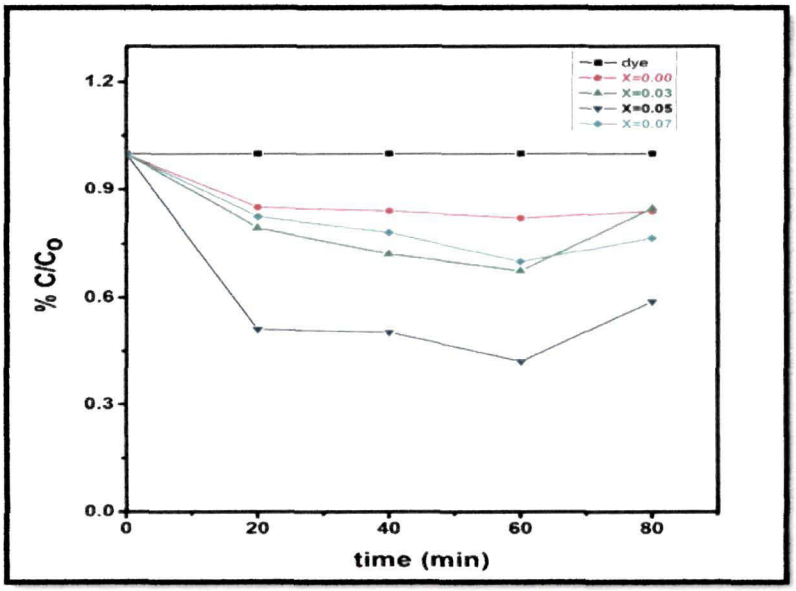

Fig.5.8: Degradation curve of phenol under visible Light.

5.4. Magnetic Measurments

Room temperature magnetic measurements (M-H) of the entire samples are carried out in the field range of ± 10 kOe. Fig.5.9 (a) shows the room temperature magnetic behavior of

undoped and Mn doped TiO_2 nanopowder annealed in air. Undoped TiO_2 shows diamagnetic behavior whereas Mn doped TiO_2 shows paramagnetism. With the increase in Mn concentration the saturation magnetization is found to decrease. This is believed to be due to strong Mn^{2+}-Mn^{2+} or Mn^{2+}-O^{2-}-Mn^{2+}antiferromagnetic interaction [27]. At lower dopant concentrations the magnetization comes from the isolated Mn^{2+} ions. However, at higher dopant concentration the average distance between the Mn^{2+} ion decreases and the Mn^{2+} ions are now paired up. The pairing takes place nearest to the oxygen ligands bonded to the Mn^{2+} ions. A strong antiferromagnetic super-exchange interaction prevents ferromagnetic alignment of the magnetic spins, resulting in decrease in magnetization. The magnetic behavior of the samples is also monitored at 10 K, Fig.5.9 (b). Paramagnetism is retained by the samples even at this low temperature. However, as compared to room temperature measurement the samples exhibit higher magnetization at 10 K. This is expected to be due to decrease in the thermal randomization of the magnetic spins. Decrease in the randomization results in the alignment of large population of frozen magnetic spins along field direction and thus, a higher magnetization is observed in the samples.

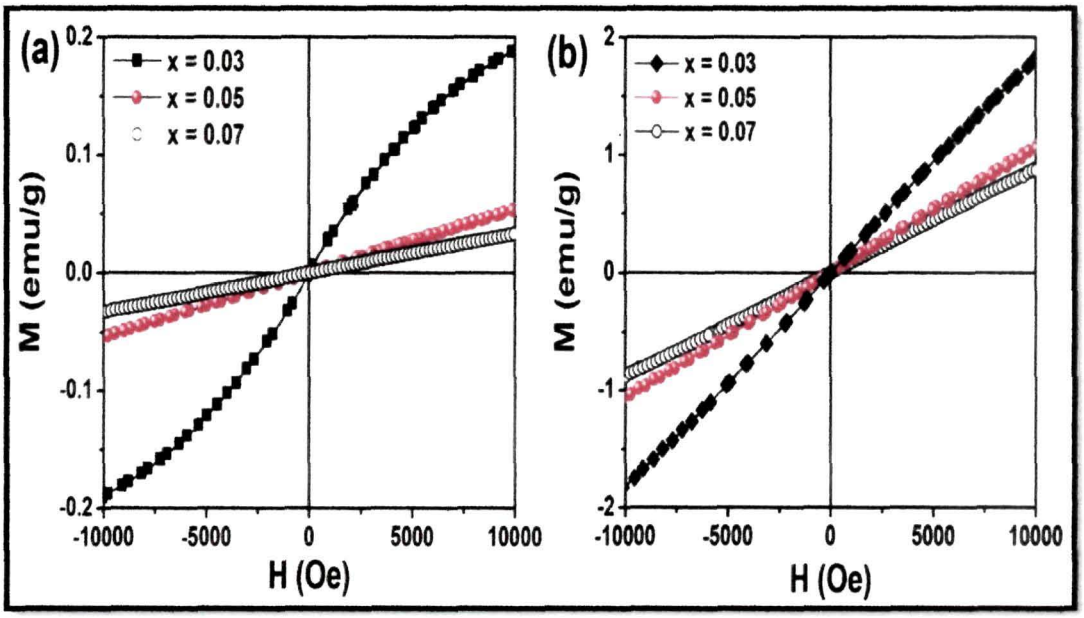

Fig.5.9: M-H curves of Mn doped TiO_2 nanoparticles at (a) Room temperature and (b) 10K.

Synthesis condition, morphology and existence of defects have a profound effect on the magnetic properties of doped TiO_2 nanoparticles. Bhattacharya.et.al [28] synthesized Mn doped TiO_2 nanoparticles by one pot RAPET technique (reaction under autogenic pressure at elevated temperature) and reported ferromagnetic behavior upto 1%. However, with the increase in dopant concentration upto 5% and 7 % the system showed paramagnetic behavior. Peng et al. [29] observed ferromagnetism in Mn doped TiO_2 nanoparticles prepared by a simple sol-gel method. Sellers and Seebauer reported room temperature ferromagnetism in Mn doped TiO_2 nanopillars prepared by atomic layer deposition method [30]. In our technique paramagnetic nature of the samples is observed. This nature is mainly attributed to the presence of oxygen vacancies. From the XRD and Raman study we have seen that doping generates oxygen vacancies and shifts the peak positions. In many previous reports it has been stated that dopants with the assistance of oxygen vacancies can promote ferromagnetism [31]. In the present study the observed paramagnetism indicates that the numbers of oxygen vacancies are not sufficient enough to couple with Mn^{2+} ions and bring ferromagnetism in the samples.

For further confirmation of the magnetism in the system, temperature dependent magnetic measurements (M-T) are carried out for all the samples. Fig.5.10 a-c shows the susceptibility (χ) vs. temperature (T) curves in the temperature range of 10-300 K at an applied field of 200 Oe. The zero field cooling (ZFC) and field cooling (FC) curves are completely overlapped upto 320 K and the nature of the curves follow the Curie-Weiss behavior of paramagnetism. The temperature dependent susceptibility (χ_0) curves were fitted with modified Curie-Weiss law:

$$\chi = \chi_0 + \frac{C}{T-\theta} \quad \text{---------- (5.2)}$$

Where χ_0 is diamagnetic susceptibility, C is Curie constant and θ is Curie-Weiss temperature. The Curie-Weiss fitting gives the following results: For 0.03 mol doping $\chi_0 = 1.63\times 10^{-4}$, C=0.53019, θ= -1.75; For 0.05 mol doping $\chi_0 = 1.2\times 10^{-2}$, C=1.066, θ= -2.48, For 0.07 mol doping $\chi_0 = 7.8\times 10^{-4}$, C=0.82, θ= -3.12. The small negative value of Curie-

Weiss (CW) temperature indicates presence of antiferromagnetic interaction in the system. As compared to 0.03 mol and 0.05 mol Mn, the value of θ is higher at 0.07 mol. The large negative value of θ confirms large antiferromagnetic interaction among the dopant ions at higher doping level. Thus, presence of both paramagnetic and antiferromagnetic interactions has been projected to affect the results of both M-H and M-T measurement curves.

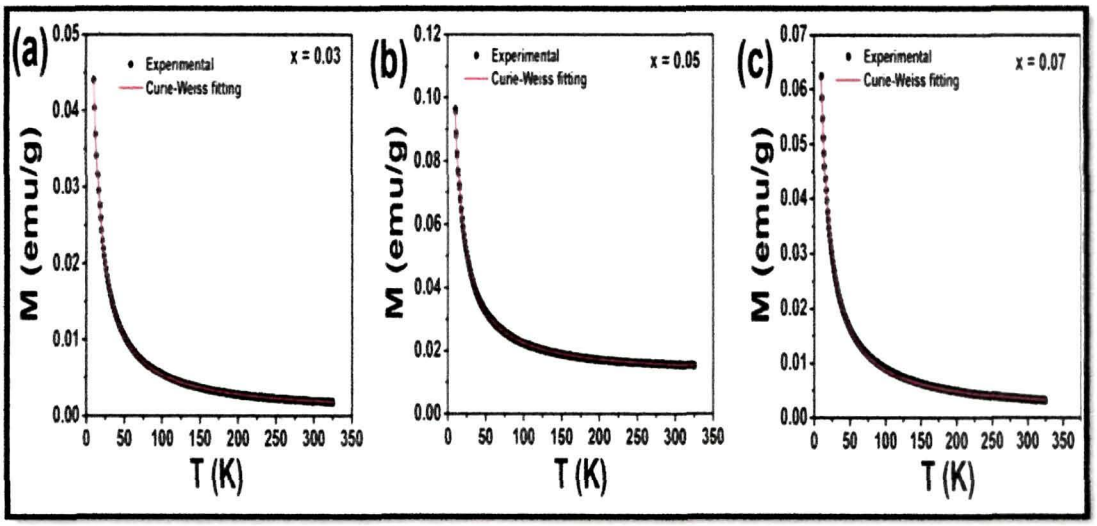

Fig.5.10: Susceptibility (χ) vs. temperature (T) curves (a) 0.03 mol (b) 0.05 mol (c) 0.07 mol Mn doped TiO_2 nanoparticles.

We have mentioned that oxygen defects play a prominent role in ferromagnetism. In order to verify whether additional oxygen defects in the system could promote ferromagnetism or not, we have calcined pure and one of the Mn doped samples (Mn = 0.07 mol) under vacuum. Room temperature M-H curves of the samples are displayed in Fig.5.11(a). Surprisingly, diamagnetic TiO_2 and paramagnetic Mn doped TiO_2 are both displaying ferromagnetism on heating under vacuum. Theoretical studies have shown that oxygen vacancies can cause a change in the band structure and can contribute to ferromagnetism [32]. Ferromagnetism in undoped TiO_2 is likely due to the ferromagnetic exchange interaction among the localized electron spins present in oxygen vacancies [33]. To confirm if some metal impurities like Co, Fe are assisting in the magnetic behavior of vacuum

annealed undoped TiO_2 nanoparticles, we have done the ICP (Inductively Coupled Plasma) analysis of the sample. For ICP analysis the sample was first digested completely in small volume of concentrated HNO_3 by heating the solution for certain time. The digested solution was then diluted to make known volumes of clear solution and then taken for ICP analysis. The amount of Co is found to be 0.000001 g/L and that of Fe is 0.000002 g/L. The amount of these metal impurities is too low. Hence, the magnetic behavior due to these impurities can be ruled out.

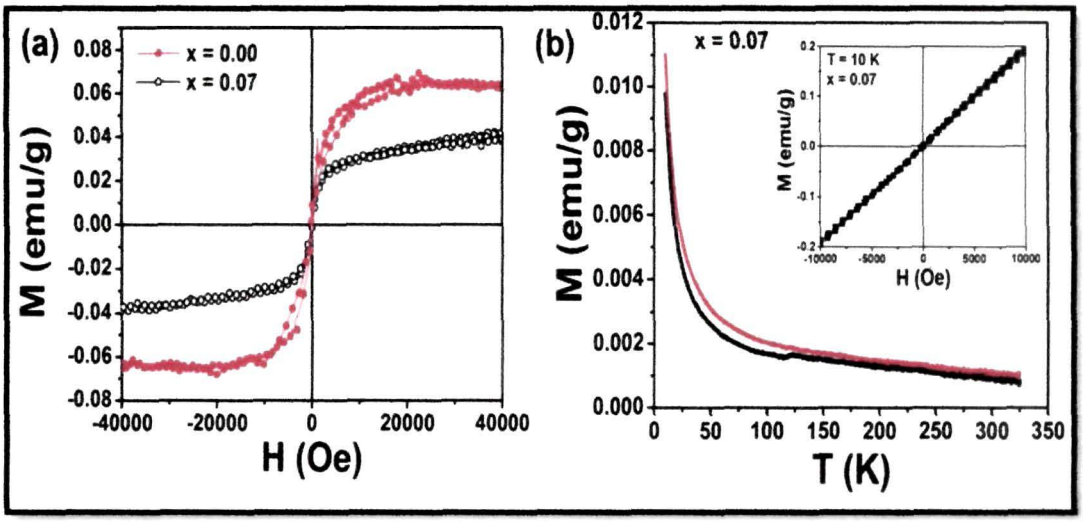

Fig.5.11: (a) Room temperature M-H curve of vacuum annealed undoped TiO_2 and 0.07 mol Mn doped TiO_2 nanoparticles.(b) M-T curve of Mn doped TiO_2 (0.07 mol) with inset showing the paramagnetic nature of the sample at 10 K.

Fig.5.11 (b) shows the M-T curve of vacuum annealed 0.07 mol Mn doped TiO_2 nanoparticles. The ZFC curve shows a small kink at a temperature of 122 K. The presence of this kink may be attributed to two main factors: First, as we have annealed the sample under vacuum it is possible that some ferromagnetic oxygen vacancy clusters might show this blocking moment [34]. Second possibility is the presence of some secondary oxide phases of Mn. Had the kink been due to the oxygen vacancy clusters the magnetization of the sample should have increased as compared to the magnetization of vacuum annealed

undoped TiO_2. But in our study we have seen that as compared to undoped TiO_2, the magnetization in Mn doped TiO_2 is reduced. This reduction in magnetization might be associated with the presence of some antiferromagnetic manganese oxide phase. The various antiferromagnetic oxide phase of Mn such as Mn_2O_3, MnO_2 have Neel temperature (TN) less than 100 K [35]. In our study the small hump in the M-T curve appears at 122 K. So the characteristic peak corresponding to the Neel temperature of Mn_2O_3, MnO_2 can be ruled out. From the literature we have found that the peak at 122 K corresponds to the Neel temperature of the antiferromagnetic oxide phase of MnO [36]. It is worth mentioning that we have also carried out the diffraction and Raman spectra analysis of the vacuum annealed undoped TiO_2 and 0.07 mol Mn doped TiO_2 nanoparticles. Unlike the air annealed samples (reported in Chapter 2), the intensity of the diffraction peaks in vacuum annealed samples are very much reduced. and the samples have very poor crystallinity, Fig.5.12(a).

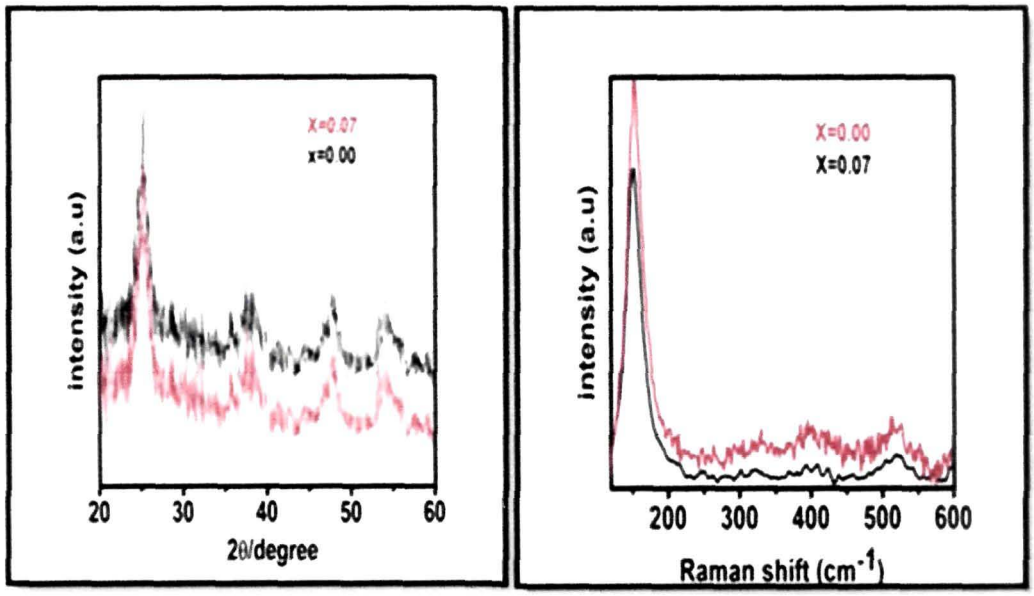

Fig.5.12: Vacuum annealed (a) XRD pattern (b) Raman spectra of undoped and Mn doped TiO_2 nanoparticles.

The diffraction peaks are broadened indicating formation of more oxygen vacancies and defects in vacuum annealed samples. In the Raman spectra of the vacuum annealed samples , Fig.5.12 (b), the Eg peak which is very prominent in case of the corresponding air annealed counterparts now becomes very broad and the intensity of these peaks are also lowered. These notable features signify the presence of increased oxygen vacancies [37]. Presence of the oxygen vacancies effects the Ti-O and Ti-O-Mn bond. Due to the poor crystalline nature of the vacuum annealed samples and also due to the presence of oxygen vacancies, the Raman scattering from the TiO_6 octahedra polarize less number of O^{2-} ions and thus a weak signal and broad peak is anticipated in the Raman spectra [38].

The presence of antiferromagnetic MnO phase as mentioned above is not detected in these XRD or Raman spectra, however the presence of this phase cannot be completely ruled out due to its small amount that is below the detection limit of the instruments [39]. Actually the M-T measurements are very responsive to the presence of any antiferro, or ferromagnetic oxide. The presence of any magnetic oxide phase is immediately marked by the presence of a kink in the curve. Further in our study it is seen that there is a steep increase in the magnetization of the curves below 30 K to 10 K. The increase in magnetization in the range of 30 K-10 K is owing to the presence of isolated paramagnetic spins of Mn^{2+} in the system. Furthermore, we have performed M-H measurement of the 0.07 mol doped samples at 10 K. The curve shows typical paramagnetic behavior and complements the nature of the M-T curve at around 10 K (shown in the inset of Fig.5.11(b)). Therefore, presence of high density of oxygen vacancies is a requisite for observing RT ferromagnetism. The main problem in the doped sample is the possibility of precipitation of secondary phases of dopants which reduces the magnetization of the system, as observed in present case. The magnetic nature of the samples studied so far depicts that presence of both ferromagnetic and anti ferromagnetic interactions is contributing to the magnetic nature of the samples. The ferromagnetism is coming due to the oxygen vacancies. In the system it is also possible that some O^{2-} ions may also be present. The doped ions couple with this doubly charged oxygen anions (Mn^{2+}-O^{2-}-Mn^{2+}) and contributes to the antiferromagnetic interactions due to which a reduction in the

magnetization is anticipated as compared to undoped vacuum annealed TiO_2.

Oxygen vacancies therefore have a profound function to play in contributing to the ferromagnetic ordering in the sample. In the air annealed samples, although oxygen vacancies affect the lattice structure of the system, the density of these oxygen vacancies, however, are not enough to undergo strong ferromagnetic exchange interaction. In undoped TiO_2, since there are no added impurities, the ferromagnetism is supposed to be intrinsic. On the other hand, in Mn doped TiO_2 the vacancies promote ferromagnetism or the vacancies may couple with nearest Mn^{2+} ions to impart ferromagnetic behavior in the system. But, the unavoidable formation of antiferromagnetic MnO phase stand as an obstacle in realizing high magnetization in the system.

Different theories have been put forwarded to explain ferromagnetism in doped semiconductor nanoparticles. Double exchange, superexchange, Rudermann-Kittel-Kasuya-Yosida (RKKY) and bound magnetic polaron (BMP) are some of the theories to explain ferromagnetism [40-42]. The first three theories are carrier mediated and mostly applicable in metallic system and the ferromagnetic ordering is not long range. However, bound magnetic polaron (BMP) theory, proposed by Coey et al., is applicable in insulating system with localized carriers [41]. According to the Bound Magnetic Polaron theory the oxygen vacancy with single trapped electron (F^+ center) behaves like a $1s$ hydrogenic type orbital. This F center may couple with the nearest Ti or Mn $3d$ orbital and form bound magnetic polaron. When the size of the bound magnetic polaron becomes large enough to percolate through the lattice, long range ferromagnetism could be realized. In undoped TiO_2 the formation of oxygen vacancies might be taking place between F center of oxygen and Ti $3d^1$ band of Ti^{3+} at the bottom of conduction band of TiO_2. In the bound magnetic polaron they undergo *s-d* exchange interaction and promote ferromagnetism. However, in the doped system the BMP formation and *s-d* exchange interaction takes place between F center of defects and Mn $3d^5$ orbital. Since there are no added magnetic impurities in the undoped TiO_2, the ferromagnetism is expected to be intrinsic. But in Mn doped TiO_2 there is a competing ferromagnetic (due to oxygen vacancy) and antiferromagnetic (due to MnO) interaction.

The oxygen anions undergo super exchange interactions with Mn^{2+} ions (Mn^{2+}-O^{2-}-Mn^{2+}) and the final outcome is the reduction in magnetization of Mn doped TiO_2 sample.

5.5. Conclusion

We can summarise our results into the following points:

1. Mn doping shifts the absorption spectra of TiO_2 to the visible region. Analysis based on lattice strain, Raman spectra, Urbach parameter suggests strong lattice distortion in the host due to doping. A remarkable red shift in the band gap transition is noticed due to band gap renormalization effect. Doping quenches the luminescence intensity by creating some non-radiative centers and increases the average lifetime of the charge carriers due to their longer relaxation time on the defect and dopant sites. Using density functional theory the presence of the defect states due to manganese incorporation has further been confirmed. The photocatalytic activity is significantly enhanced on doping and maximum degradation is obtained for dopant concentration of 0.05 mol.

2. Mn doped TiO_2 samples display complete paramagnetic behavior at room temperature as well as at 10 K. There is persistence of antiferromagnetic ordering in all the samples as exemplified from the negative Curie-Weiss temperature in the temperature dependent magnetization measurement. The observed paramagnetism is expected to be appearing owing to the presence of isolated magnetic spins of Mn^{2+} in the system. Increased Mn^{2+} -Mn^{2+} direct exchange interaction and Mn^{2+}-O^{2-}-Mn^{2+} superexchange interaction are believed to be contributing towards antiferromagnetism. Ferromagnetism is observed when the pure and doped (x=0.07 mol) samples are heat treated under vacuum condition. Ferromagnetism in pure TiO_2 nanoparticles is owing to the presence of oxygen defects. Although Mn doped TiO_2 exhibits ferromagnetism, the magnetization is less than that of pure TiO_2. This is likely due to the formation of secondary MnO

phases in the Mn doped TiO_2 samples. Therefore, Mn doping degrades the ferromagnetic ordering of TiO_2.

References

[1].Deng,Q.R., et.al Mn-doped TiO_2 nanopowders with remarkable visible light photocatalytic activit, *Material Lett* **65** (13),2051-2054, 2011.

[2].Duan.J., et.al Mn-doped ZnO nanotubes; from facile solution synthesis to room temperature ferromagnetism, *Cryst. Eng. Comm* **14** (12), 1330-1336, 2012.

[3].Binas.V.D., et.al Synthesis and photocatalytic activity of Mn-doped TiO_2 nanostructured powders under UV and visible light, *Appl. Catal. B: Environment.* **113**, 79-86, 2012.

[4].Mo, S and Ching,W.Y . Electronic and optical properties of three phases of titanium dioxide: Rutile, anatase, brookite, *Phys Rev Condens Matter* **51** (19), 13023-13032, 1995.

[5]. Reddy.B.S., et.al EPR and optical absorption spectral studies on Mn^{2+} ions doped in potassium thiourea bromide single crystals, *J. Mol. Struc.* **751** (1), 161-167, 2005.

[6].Dow,J. D & Redfield ,D. Toward a unified theory of Urbach's rule and exponential absorption edge, *Phys. Rev. B* **5** (2), 594-610, 1972.

[7].Wang,Y.G., et.al Photoluminescence study of ZnO prepared by thermal oxidation of Zn metallic films air, *J. Appl. Phys* **94** (1), 354-358, 2003.

[8]. Nishikawa, Y., et.al Tensile Strain in Si Due to Expansion of Lattice Spacings in CeO_2 Epitaxially Grown on Si (111), *J. Electrochem. Soc* **151** (9), 202-205, 2004.

[9].Sharma,S., et.al. DC magnetization investigation in $Ti_{1-x}Mn_xO_2$ nanocrystalline powders, *J.Alloy and Compd*, **59** (27), 7434-7438, 2011.

[10]. Lethy,K.J ., Bandgap renormalization in titania modified nanostructured tungsten oxide thin films prepared by pulsed laser deposition technique for solar cell application, *J.Appl.Phys* **104** (3), 033515, 2008.

[11]. Prathap,P., et.al Thickness effect on the microstructure , morphology and optoelec tronic properties of ZnS films, *J.Phys.Condens. Matter* **20** (3), 035205, 2008.

[12]. Walsh,A., et.al Origin of band-gap renormalization in degenerately doped semi Conductors, *Phys.Rev.B* **78** (7), 075211, 2008.

[13]. Serpone,D., et.al Size effects on the Photophysical Properties of Colloidal Anatase

TiO_2 Particles: Size Quantization versus Direct transition in This Indirect Semi Conductor, *J.Phys.Chem* **99**(45),16646-16654,1995.

[14]. Lei,Y., et.al Fabrication, characterization and photoluminescence properties of highly ordered TiO_2 nanoarrays, *J. Phys. Chem.* **99** (45), 16646-16654, 1995.

[15]. Knorr,F.J., et.al Trap-state distribution and carrier transport in pure and mixed-phase TiO_2 : influence of coating solvent and interfacial electron transfer, *J.Phys Chem.C* **112** (113), 12786–12794, 2008.

[16]. Wan,Y.W , et.al Room temperature Synthesis of Single-Crystalline Anatase TiO_2 Nanowires, *Cryst. Growth and Design* **10** (4), 1646-1651, 2010.

[17]. Yu,J.C., et.al Effects of F^- doping on the Photocatalytic Activity and Microstruc tures of Nanocrystalline TiO_2 powders, *Chem. Mater* **14** (9) ,3808-3816, 2002.

[18]. Serpone, N Is the band Gap of Pristine TiO_2 Narrowed by Anion and Cation Dop ing of Titanium Dioxide in Second Generation Photocatalysts, *J.Phys.Chem B* **110** (48), 24287- 24293, 2006.

[19]. Das,K., et.al Morphology dependent Luminescent Properties of Co doped TiO_2 Nanoparticles, *J.Phys.Chem.C* **113** (33) ,14783-14792, 2009.

[20]. Santara,B., et.al Signature of strong ferromagnetism and optical properties of Co doped TiO_2 nanoparticles, *J.Appl.Phys* **110** (11),114322,2011.

[21]. Paul,S., et.al Effect of manganese doping on the optical property and photocatalytic activity of nanocrystalline titania: Experimental and theoretical investigation, *J. Alloys and Comp.* **583**, 578-586, 2014.

[22]. Khosravi, A.A., et.al Green luminescence from copper doped zinc sulphide quantum Particles, *Appl.Phys.Lett* **67**(18), 2702-2704, 1995.

[23].Yalcin.Y., et.al Fe^{3+} doped TiO_2: A combined experimental and computational ap-proach to the evaluation of visible light photocatalytic activity, *Appl.Catal.B* **99** (3- 4), 469-477, 20210.

[24].Li.M., et.al Electronic structure and photocatalytic activity of N/Mo doped anatase TiO_2, *Catal. Commun* **29**,175-179, 2012.

[25]. Xiao.Q., et.al Characterisation and photocatalytic activity of Sm^{3+} doped TiO_2 na-

nocrystalline TiO_2 prepared by low temperature combustion method, *J.Alloys and Compd* **450** (1-2), 426-431, 2008.

[26]. Devi.G.L., et.al Enhanced photocatalytic activity of transition metal ions Mn^{2+}, Ni^{2+}, and Zn^{2+} doped polycrystalline titania for the degradation of Aniline Blue under UV/ solar light, *J.Mol Catal.A Chem* **328** (1-2), 44-52, 2010.

[27]. Li., H.M., et.al Coexistence of antiferromagnetic and ferromagnetic in Mn-doped anatase TiO_2 nanowires, *J.Central South Univ* **17** (2),239-243, 2010.

[28]. Bhattacharyya .S., et.al One-pot fabrication and magnetic studies of Mn-doped TiO_2 nanocrystals with an encapsulating carbon layer, *Nanotech* **19**(49),1-8, 2008.

[29]. Peng.D., et.al Structure, room-temperature magnetic and optical properties of Mn doped TiO_2 nano powders prepared by the sol-gel process, *Chin.Phys.B* **19** (11), 118102, 2010.

[30]. Sellers,M. C.K & Seebauer,E.G. Room temperature ferromagnetism in Mn- doped TiO_2 nanopillar matrices, *Mat. Lett* **114** (1), 44-47, 2014.

[31]. Choudhury.B, , et.al Effect of oxygen vacancy and dopant concentration on the magnetic properties of high spin Co^{2+} doped TiO_2 nanoparticles, *J.Magnetism and Magnetic Mater.* **323** (5), 440- 446, 2011.

[32]. Min.W., et.al First principles study of the electronic structure and magnetism of oxygen -deficient anatase TiO_2 (0 0 1) surface, *Appl. Surf.Sci* **292**, 475- 479, 2014.

[33]. Batakrushna.S., et.al Evidence of oxygen vacancy induced room temperature ferromagnetism in solvothermally synthesized undoped TiO_2 nanoribbons, *Nanoscale* **5** (12), 5476-5488, 2013.

[34]. http://www.qdusa.com/sitedocs/appNotes/mpms/1014-210.pdf

[35]. Xu,L.M., et.al Enhancement of ferromagnetic upon thermal annealing in plasma as sisted MBE grown mixed-up Mn- doped insulating TiO_2 thin films, *Appl. Phys. A.Mater. Sci .Process* **92** (2) , 361-365, 2008.

[36]. Lee.Y.C., et.al Size-driven magnetic transitions in monodisperse MnO Nanocrystals, *J. Appl. Phys* **107** (9), 09E124, 2010.

[37]. Xu.J.P., et.al Effect of annealing ambient on the ferromagnetism of Mn-doped anatase TiO_2 films, *J.Phys.D:Appl.Phys* **40** (16) ,4757-4760, 2008.

[38]. Choudhury.B and Choudhury. A Room temperature ferromagnetism in defective TiO_2 nanoparticles: Role of surface and grain boundary oxygen vacancies , *J.Appl. Phys* **114** (20),203906, 2013.

[39]. Sharma.S., et.al Room temperature ferromagnetism in Mn doped TiO_2 thin films: Electronic structure and Raman investigations, *J. Appl.Phys* **109** (8), 083905, 2011.

[40]. Lu,Z.L., The origins of ferromagnetism in Co-doped ZnO single crystalline films : From bound magnetic polaron to free carrier-mediated exchange interaction *Appl. Phys.Lett.* **95** (10), 102501, 2009.

[41]. Coey.J.M.D., et.al Donor impurity band exchange in dilute ferromagnetic oxides , *Nat. Mater* **4** , 173-179, 2005.

[42]. Coey.J.M.D., et.al Ferromagnetism in Fe-doped SnO_2 thin films, *Appl. Phys. Lett.* **84** (8) ,1332-1334, 2008.

CHAPTER 6

Investigation of the changes in the various properties of TiO_2 nanoparticles by gadolinium doping

The synthesis procedure of Gd doped TiO_2 nanoparticles have been described in chapter 2. Structural and morphological characterization with the help of XRD, Raman and TEM confirmed that the prepared nanoparticles are in anatase form. XPS spectra revealed that the gadolinium ions are in the trivalent state. Incorporation of Gd ions is expected to modulate the electronic structure of the material and thereby enhance the photocatalytic properties of the material. In this chapter we will mainly focus on the changes in the optical properties and photocatalytic activities of the nanoparticles on incorporation of different concentrations of gadolinium. The dependence of the magnetic properties on the different concentration of gadolinium will also be discussed.

6.1 Optical property study

6.1.1. UV-Vis and Photoluminescence spectra analysis

The influence of Gd concentration on the absorption of TiO_2 nanoparticles, measured at room temperatures is shown in Fig.6.1. The absorption band edge of the TiO_2 nanoparticle is 340 nm which is in the UV region. The effect of Gd ions on the optical properties of TiO_2, is revealed by shifting of the absorption band towards the visible region. This shifting is most likely due to the transition of electrons from the valence band to the 4*f* levels of Gd. The observation is in accordance with the absorbance spectra of other rare earth doped TiO_2 nanoparticles [1].The photoluminescence spectra owing to the recombination of charge carriers is a useful tool to explore the effectiveness of charge carrier trapping, migration, alteration and separation of charge carriers [2]. Fig.6.2a shows the PL spectra of samples with an excitation wave length of 320 nm. Undoped TiO_2 shows near band edge emission peak at 398 nm. Addition of Gd^{3+} ions results in the loss of

oxygen atoms and generation of free electrons. The electrons that are trapped in the oxygen vacancy results in the formation of F center or color centers. Depending on the number of trapped electrons, these centers are referred as F (two electrons), F^+ (one electron) and F^{2+} (devoid of electrons). The emission peaks at 490 nm and 535 nm are attributed respectively to the transition from the oxygen vacancies with two trapped electrons and one trapped electron to the valence band of TiO_2 [3].

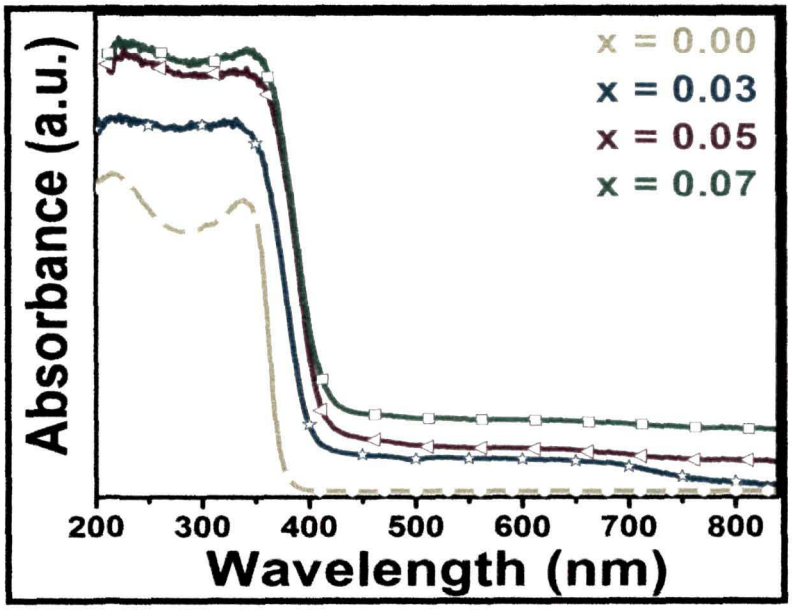

Fig.6.1: Absorption spectra of all the samples

Another peak at 429 nm is attributed to self trapped excitons (STE) originated by interactions of conduction band electrons localized on the Ti 3*d* orbital with holes present in the O 2*p* orbital of TiO_2 [4]. For clear observation of the emission peaks we have done Gaussian fitting (r^2= 0.99), Fig.6.2b. A close analysis of the intensity of the band edge emission peak reveals that the intensity of this peak is reduced with the addition of gadolinium ions. This reduction in the intensity is attributed to the band gap narrowing introduced by the formation of *f* states of the gadolinium ions. Fig.6.3 shows variation of band gap with the increase in dopant concentration. In the photoluminescence process the electrons in the conduction band gets trapped into the oxygen vacancies via non-radiative

process and than recombines with the photogenerated holes in the valence band accompanied by fluorescence emission.

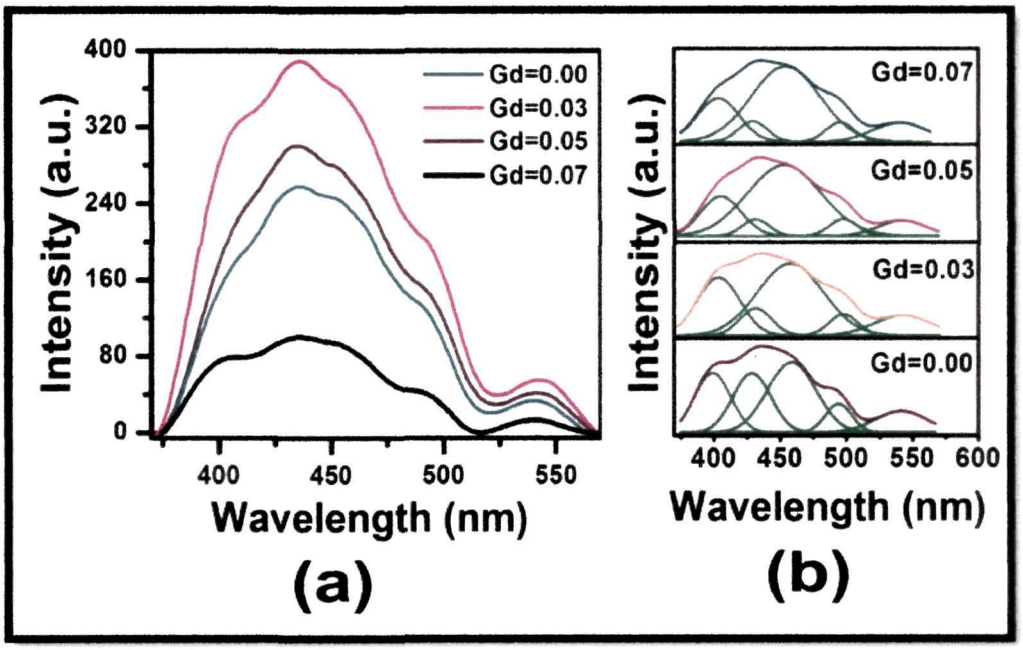

Fig.6.2: (a) PL spectra of the samples with λ_{ex} = 320 nm (b) Gaussian fitting of the peaks

In the PL spectra no Gd^{3+} ions related emission peaks are observed. Only changes in the emission intensity are noticed after doping. The emission intensity increases on incorporation of 0.03 mol and 0.05 mol Gd and thereafter there is sudden quenching of intensity on incorporation of 0.07 mol Gd. At lower dopant concentration the interactions between ions are too weak to have an effect on the energy levels of each dopant ion. But as the dopant concentration increases the distance between the ions decreases and the density of defects increases. The emission energy is now transferred from one ion to another ions or to another defects and the energy is dissipated non-radiatively resulting in the reduction of emission intensity.

We have calculated the average shortest distance (known as the critical distance) between ions at which the emission energy transfer occurs, using the equation [5]

$$R_C = 2\left(\frac{3V}{4\pi\pi_c N}\right)^{1/3} \quad \text{---------- (6.1)}$$

V= volume of the unit cell = a^2c= 0.133 nm^3, where a= 0.3784 nm; c= 0.9420 nm. x_c = critical concentration of the dopant (= 0.07), N = Number of Z ions in the unit cell, R_c= the critical transfer distance. Putting the values the critical distance (R_c) for 0.07mol is calculated to be 0.9682 nm. Therefore, Gadolinium doping is responsible for the red shift of the absorption band edge and band gap narrowing owing to the introduction of *f* states. These *f* states can largely delay the electron-hole recombination rate and contribute to the enhancement of the photocatalytic activity.

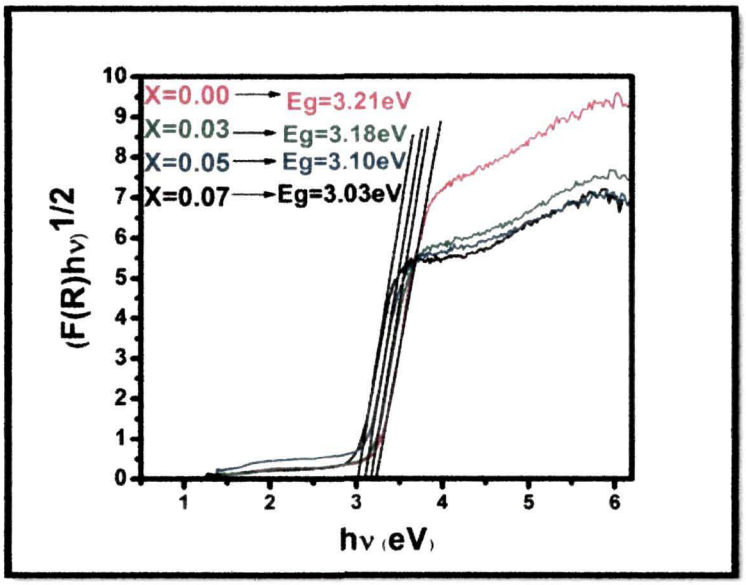

Fig.6.3: Band gap analysis of the samples from Kubelka Munk Plot

6.2. Theoretical Study

To understand the electronic structure of Gd doped TiO_2 theoretical study is carried out considering two supercells Ti_8O_{16} and Ti_7GdO_{16} along with spin polarized calculation. Density of states (DOS) is calculated for both the systems as shown in Fig.6.4(a)-(b)

respectively. Although standard DFT calculation may not determine the actual band gap, it could frame out the changes in optical properties of Gd doped TiO_2 system with respect to pristine TiO_2 system. Fermi level in DOS is considered at 0 eV. If we compare the TDOS (Total Density of States) of Gd doped TiO_2 and TiO_2 , we observe presence of states near the Fermi level in Gd doped TiO_2 while in pure TiO_2 there are no such levels near the Fermi level. Our interest is to identify the atoms responsible for the states near the Fermi level in Gd doped TiO_2 and hence plotted PDOS (Partial Density of States) for Gd, Ti and O as shown in Fig. 6.4 b.

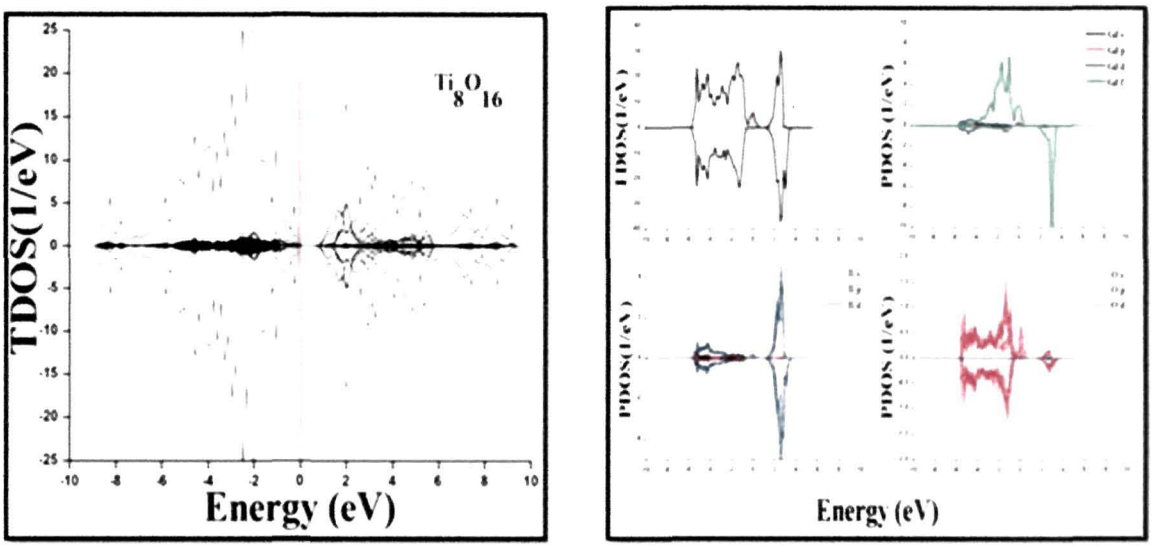

Fig.6.4 (a) TDOS (Total Density Of State) of Undoped TiO_2.(b) TDOS and PDOS (Partial density of states)

PDOS plots shows that Gd 4*f* state is the most prominent near the Fermi level whereas Ti and O have lesser impact. We have also observed that other states of Gd i.e., *s*, *p* and *d* has almost no contribution in comparison to the *f* state. This very much indicates that *f* state of Gd is the key factor to tune the optical property of TiO_2. On the other hand *d* and *p* states

are the most effective states for Ti and O near the Fermi level respectively. The formation of these states near the Fermi level is due to the instability in structure as the system (TiO_2) is suffering from foreign entity (Gd). The irregular bonding and unstable charge transfer among Gd, Ti and O leads to the splitting of states near the Fermi level. The instability in charge transfer occurs after substitution of Ti^{4+} ion by Gd^{3+} ion. A weak hybridization is observed among Gd 4*f*, O 2*p* and Ti 3*d* states below the Fermi level. Chen et.al [6] found that the Gd doping in TiO_2 does not produce any states near the Fermi level. But in our case we have observed a prominent Gd 4*f* state at and above Fermi level. These states might act as trapping state. Illumination of a solid with UV/Vis light excites electrons to the conduction band leaving holes behind in the valence band. During the period of this photo excitation process few electrons move to the conduction band while few others are trapped in the levels created due to Gd 4*f* state. These trapped electrons easily migrate to the surface and react with the atmospheric O_2 molecules to convert it to superoxide (O_2^-) radicals [7].These superoxide radicals act as a potential candidate in the photocatalysis process.

6.3. Photocatalytic Activity

Using aqueous phenol as the targeting medium the visible light photocatalytic activity of undoped and Gd^{3+} ion doped TiO_2 nanoparticles were studied. Prior to the photocatalyst addition the phenol solution was irradiated for 20, 40, 60 and 80 min. No appreciable self degradation was seen as evident from the degradation curve Fig.6.5. Pure TiO_2 has a very low visible light photoactivity due to its large band gap. The photocatalytic activity has been found to be largely improved on incorporating gadolinium ions. Under visible light irradiation electrons are excited from the valence band to the conduction band. Gadolinium dopant in TiO_2 can effectively scavenge electrons and prevent their recombination with holes due to the existence of half filled *f* orbitals of the gadolinium ions. The presence of these *f* orbitals have been supported with the help of DFT based calculations as mentioned above. The Gd^{3+}ions with half filled *f* orbitals are very stable. When these Gd ions trap electrons the electronic configuration is largely destroyed and their stability decreases, the trapped electrons are easily transferred to the oxygen molecules adsorbed on the surface of

the catalysts, and the Gd^{3+} ions return to the original stable half-filled electronic structure. This in turn promote charge transfer and proficiently disperse the electrons and holes by superficially trapping the electrons [8].

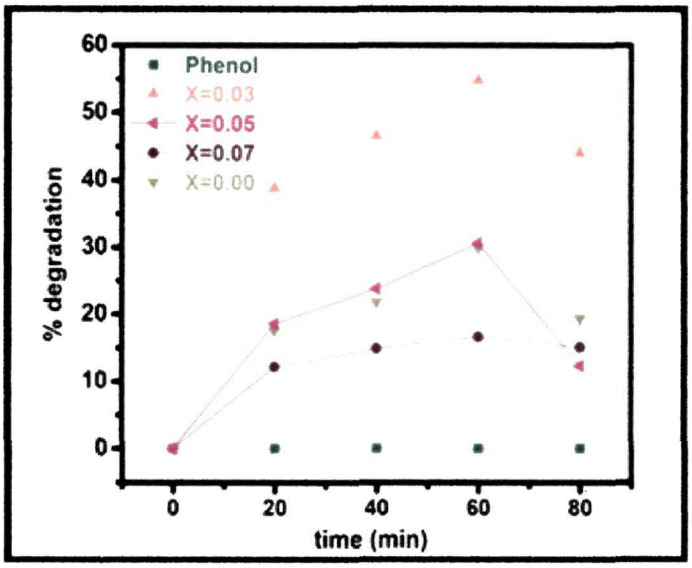

Fig.6.5: Degradation curve under visible-light illumination

$$Gd^{3+} + e^- \rightarrow Gd^{2+}$$
$$Gd^{2+} + O_{2adbs} \rightarrow Gd^{3+} + O_2^{\bullet}$$
$$Gd^{3+} + h^+ \rightarrow Gd^{4+}$$
$$Gd^{4+} + OH^- \rightarrow Gd^{3+} + OH^{\bullet}$$

Fig.6.6 shows the schematic illustration of the photocatalytic activity of Gd doped TiO_2 nanoparticles. The mechanism of trapping and detrapping can be represented with the following mechanisms:

The Gd^{4+} can also trap conduction band electron or Gd^{2+} can trap valence band hole to retain half filled electronic structure of Gd^{3+}.

$$Gd^{4+} + e^- \rightarrow Gd^{3+}$$
$$Gd^{2+} + h^+ \rightarrow Gd^{3+}$$

The enhanced photocatalytic activity is owing to the presence of half filled orbitals of the gadolinium ions that serve as shallow trap for the charge carriers to accelerate interfacial charge transfer process [9]. The processes not only accelerate interfacial charge transfer but also enhance the generation of highly reactive oxidative species like superoxide and hydroxyl radicals.

$TiO_2/Gd^{3+} \xrightarrow{h\nu} e^- + h^+$

$OH^* + h^+ \xrightarrow{h\nu} OH^*$

$O_2 + e^- \rightarrow O_2^-$

$Phenol + O_2^- \rightarrow Products$

$Phenol + OH^* \rightarrow Products$

Due to difference in charge state, substitution of Gd^{3+} ions leads to creation of oxygen vacancies. These oxygen vacancies promote the adsorption of O_2 molecules and favors the adsorbed oxygen to arrest the photoelectrons simultaneously producing free radicals [10].The presence of these oxygen vacancies has been testified from the XPS (Chapter 2) and the photoluminescence spectra. In the photoluminescence process oxygen vacancies and defects bind the photoinduced electrons to form free or binding excitons so that PL signal can easily occur , the larger the amount of oxygen vacancies, the stronger the PL intensity. But in the photocatalytic process these oxygen vacancies and defects become centers to capture the photo induced electrons so that the recombination of photoinduced electrons and holes is effectively inhibited. In our work the photoluminescence intensity has been found to be maximum at 0.03 mol dopant concentration and at this concentration we are getting higher photocatalytic activity. Thus the results demonstrates certain kind of correlation between the photoluminescence process and photocatalytic activity, the stronger the PL intensity the larger the content of oxygen vacancies and defects , the higher the photocatalytic activity .Further the surface area of the nanoparticle has a profound role to enhance the photocatalytic activity. In chapter 2 we have seen that introduction of the dopant ion causes a considerable increase in surface area and a decrease in pore size , thus favoring the criteria for enhanced photocatalytic activity.

After 60 minutes, the degradation curve shows a decrease in the degradation trend.

Although longer irradiation period produces higher number of charge carriers but only limited number of them reaches the semiconductor liquid interface region for dye degradation, the rest undergo volume recombination dominating the reaction in accordance with the equation [11].

$$K_R \propto \exp \frac{-2R}{a_o} \quad \text{---------- (6.2)}$$

Here K_R is the rate of recombination , R is the distance separating the electron and the hole pair, a_o is the hydrogenic radius of the wave function of the charge carriers. The recombination rate increases due to the decrease in the number of the trap sites. Thus it is seen that after 60 min of irradiation and production of charge carriers on the surface of Gd doped TiO_2 nanoparticles, the rate of recombination is dominated to the rate of other reactions in the solution [11].

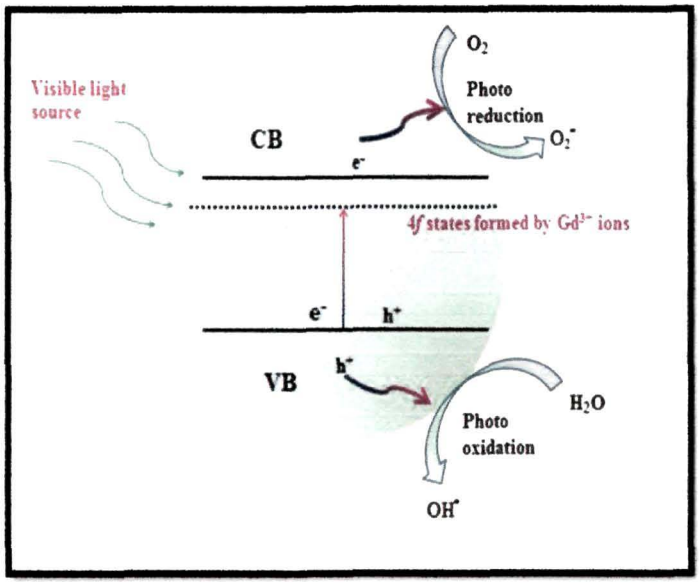

Fig.6.6: Schematic illustration of the photocatalytic process by Gd doped TiO_2 nanoparticles

Dopant concentration also has some important influence in regulating the photocatalytic

reaction rate. In the degradation curve it is observed that dopant concentration of 0.07 mol is showing the lowest photocatalytic activity. On this basis it is surmised that there exists an optimum dopant concentration in the TiO_2 matrix to protract the separation of photogenerated charge carriers. The decrease in the activity can be correlated to the thickness of the space charge layer that is inversely proportional to the dopant concentration. The thickness of the space charge layer is affected by dopant concentration according to the equation [11]

$$W = \left(\frac{2\varepsilon\varepsilon_o V}{eN_d}\right)^{1/2} \quad \text{---------- (6.3)}$$

W is the thickness of the space charge layer. ε and ε_o are the dielectric constants of the semiconductor and vacuum. With the increase in the dopant concentration the thickness of the space charge layer becomes less than the penetration depth of light and this greately increases the electron hole recombination rate. In addition at this higher concentration charge carriers undergo multiple trapping. This behavior decreases the mobility rate as a result of which they are absorbed before they can reach the surface. This behavior has been attributed to an increased recombination rate with dopant concentration due to the concomitant decrease in the average distance between the trap sites [12].

6.4. Magnetic property Study

Fig. 6.7 illustrates the M-H curves of 0.03, 0.05 and 0.07 mol Gd doped TiO_2 nanoparticle in the magnetic field range of ±15 kOe. The curves manifests typical behavior of paramagnetism. The magnetization increases by a small amount with increase in Gd upto 0.05 mol. The magnetization of 0.07 mol is less than that of 0.05 mol. The observed paramagnetism might be due to the presence of isolated Gd^{3+} ions, whereas decrease in magnetization is most likely due to the presence of antiferromagnetic interaction in the system. While incorporating Gd into TiO_2, room temperature ferromagnetism with high magnetization is expected in the system. The notion behind this expectation is that Gd is ferromagnetic in nature with persistence of ferromagnetic ordering upto ~289 K [13]. The electronic configuration of Gd^{3+} is [Xe] $6s^2 5d^1 4f^7$ with 7 unpaired electrons in the $4f$ shell.

These unpaired $4f$ electrons polarize the $6s$ and $5d$ valence electrons resulting in magnetic moment of 7.63 μ_B/Gd^{3+} [14]. However, due to shielding of the $4f$ shell by $6s5d$ valence shell electrons, the interaction of the unpaired spins with the outermost ligands or other Gd^{3+} is expected to be weak. These non-interacting and localized magnetic spins of Gd^{3+} induce only paramagnetic moment [13,14].

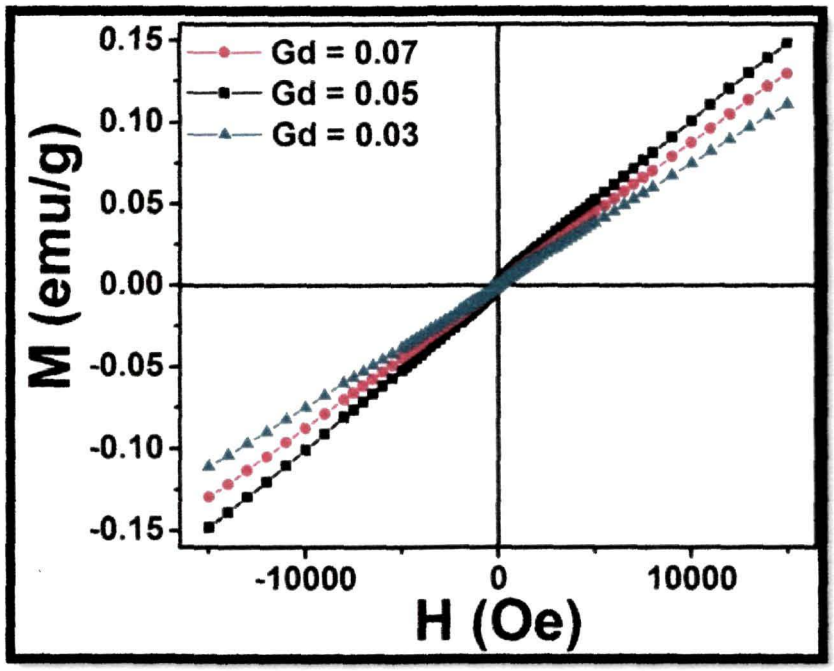

Fig.6.7: Room temperature M-H curves of Gd doped TiO_2 nanoparticles.

Paramagnetism at room temperature has been reported in pure Gd_2O_3 as well as in Gd doped oxide semiconductors such as TiO_2, SnO_2, ZnO, etc [13-18]. Opera, *et al.* in his work on Gd doped ZnO reported ferromagnetism and attributed it to the intra-ion $4f$-$5d$ exchange interaction followed by inter-ion $5d$-$5d$ coupling mediated by charge carriers [19]. In Gd doped ZnO films , Ney et al. [20] reported paramagnetic behavior of the samples with magnetic moment of 7.63 μ_B/Gd^{3+} with a small lattice distortion, the results are in agreement with the first-principles density-functional theory calculations. They detected presence of secondary oxide phases of Gd_2O_3 or other antiferromagnetic phase of

Gd^{3+} contributing to the reduction in the paramagnetic behavior [20]. Adhikari *et al.* in Gd doped SnO_2 observed absence of ferromagnetism due to surface spin effect and enhanced Gd-O-Gd interactions [17]. Magnetic properties of rare earth doped (RE=Nd, Sm, Gd, Tb, Er and Dy) CeO_2 have been investigated by Dimri *et al.* [21]. The origin of magnetism in this sample is attributed to the presence of oxygen vacancies created due to the rare-earth dopants [21]. Wang *et al.* studied the magnetic property of pure and Gd doped HfO_2 and reported very weak ferromagnetism in the sample, attributing it to either impure target materials or signal from the substrates [22].

To support the M-H curve of the samples and for further confirmation of the nature of magnetism in the system, we carried out temperature dependent magnetic measurements (M-T) for 0.03 mol and 0.07 mol Gd doped TiO_2. Fig.6.8a-b shows the susceptibility (χ) *vs.* temperature (T) curves in the temperature range of 10-300 K at an applied field of 200 Oe. The zero field cooling (ZFC) and field cooling (FC) curves are completely overlapped upto 300 K and the nature of the curves follow the Curie-Weiss behavior of paramagnetism.

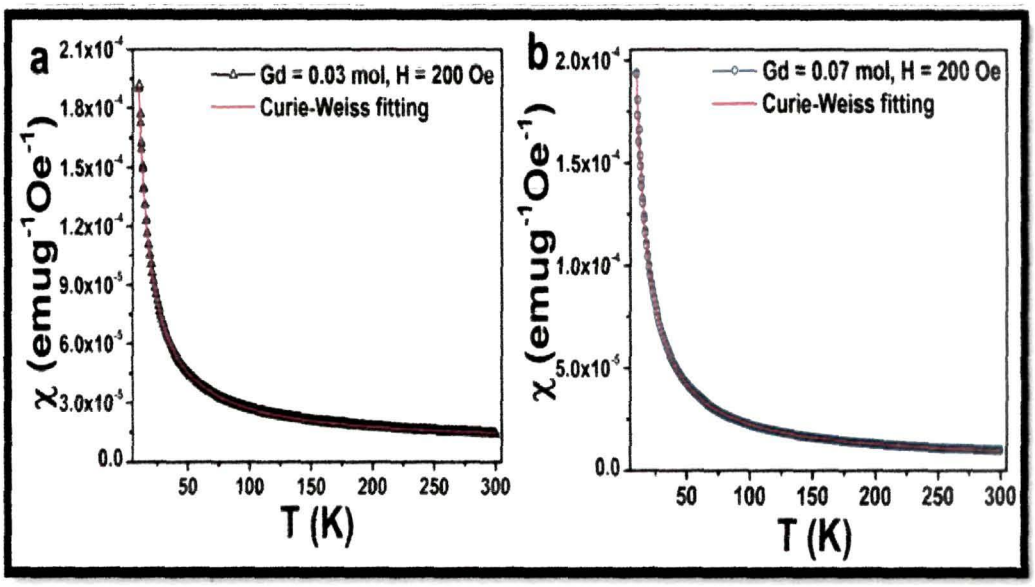

Fig.6.8: Susceptibility (χ) vs. temperature (T) curves (a) 0.03 mol and (b) 0.07 mol doped TiO_2 nanoparticles.

The rise in magnetization at low temperature is because of the decrease in thermal

randomization of fluctuating magnetic spins present in isolated Gd^{3+} ions. The temperature dependent susceptibility (χ) curves were fitted with modified Curie-Weiss law

$$\chi = \chi_0 + \frac{C}{T-\theta} \quad \text{----------} \quad (6.4)$$

Where χ_0 is diamagnetic susceptibility, C is Curie constant and θ is Curie-Weiss tempera ture. For 3 mol % Gd doped TiO_2 the Curie-Weiss fitting gives the following results, χ_0 = 8.37×10^{-6}, C = 0.0018, θ = (-) 0.2044. For 0.07 mol Gd doped TiO_2 the fitted values for χ_0, C and θ are 2.96×10^{-6}, 0.0019 and (-) 0.3025 respectively.

The small negative value of Curie-Weiss temperature indicates persistence of antiferromagnetic interaction in the system. As compared to 0.03 mol Gd, the value of θ is higher at 0.07 mol. The large negative value of θ confirms large antiferromagnetic interaction among dopant ions at higher doping level. Therefore, from the results of M-H and M-T presence of both paramagnetic and antiferromagnetic phases are anticipated in the system. From the XRD and Raman analysis it is seen that with the increase in doping concentration a large number of Gd^{3+} resides on the surface. Higher doping level decreases the separation among Gd^{3+} ions. During discussion on PL it is mentioned that the distance between Gd^{3+} ions is 0.9731 nm when Gd^{3+} doping level is 0.07 mol. The Gd^{3+} ions at this distance apart may undergo superexchange interaction with each other via O^{2-} ions, thereby resulting in the antiparallel alignment of the magnetic spins of Gd 4*f* shell present in the nearest neighbor. The antiferromagnetic interaction gets stronger at 0.07 mol and as a result of this the Curie-Weiss temperature is more negative at 0.07 mol than at 0.03 mol.

The magnetic measurements of 0.03 and 0.07 mol Gd doped TiO_2 has also been studied at 10 K ,Fig.6.9. and at magnetic field of ±45 kOe. It is observed that even at 10 K and at such a high applied field the nanoparticles of Gd doped TiO_2 failed to show any ferromagnetic ordering. The magnetic curves are nearly linear with magnetic field exhibiting the characteristic of paramagnetism. However, unlike the linear M-H curves of the samples measured at room temperature, the magnetic curves at 10 K are trying to get

the shape of hysteresis. But the magnetization is not saturated even at 45 KOe. The slight bent noticed in the M-H curve is likely due to the minimization of the thermal randomization of the magnetic spins at 10 K. Further the magnetization at 0.07 mol is found to be slightly higher as compared to 0.03 mol. The higher magnetization at this concentration might be due to decrease in the thermal randomization and contribution of large numbers of localized non-interacting magnetic spins of Gd^{3+}.

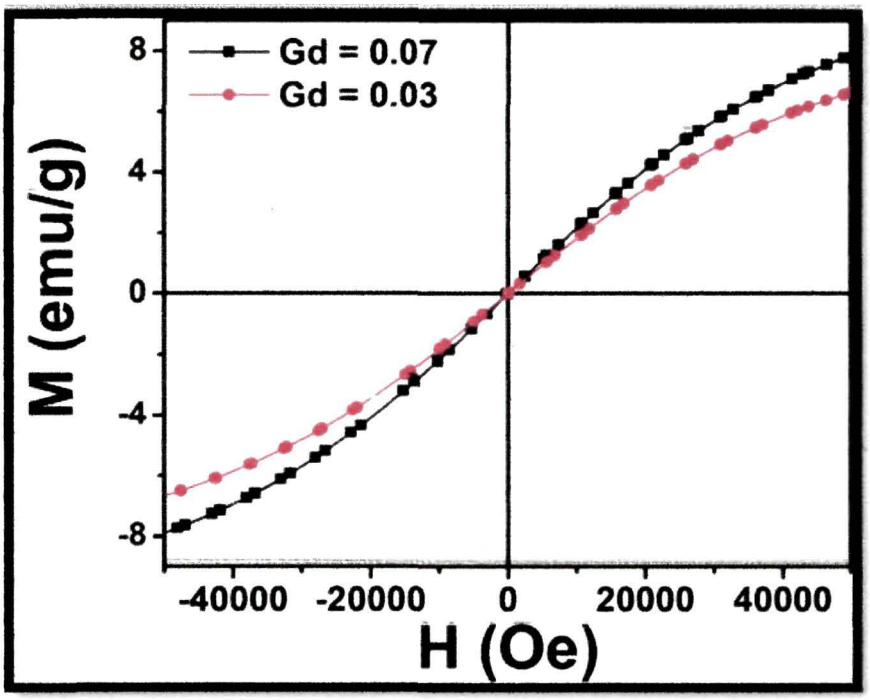

Fig.6.9: M-H curves of 0.03 mol and 0.07 mol Gd doped TiO_2 measured at 10 K.

6.5. Conclusion

1. In summary it can be said that Gadolinium doping has affected the optical properties of TiO_2 nanoparticles. Owing to the presence of gadolinium ions, there is a substantial increase in the surface area. The PL spectra depicts increased peak in tensity at 0.03 mol Gd ions and at this concentration the samples display maximum photcatalytic activity. Using density functional theory the *f* states generated due

to the presence of gadolinium ions in the host matrix are identified and these states are believed to contribute to the enhanced photocatalytic activity.

2. Magnetic study of the samples depicts paramagnetic nature at room temperature and as well as at 10 K. It is observed that due to shielding of $4f$ shell of Gd^{3+} ions by $6s5d$ shell the direct exchange interaction of these Gd^{3+} ions with other Gd^{3+} ions is weak. These non-interacting and localized magnetic spins of Gd^{3+} induce only paramagnetism. The high magnetization exhibited by the samples at 10 K is due to minimization of the thermal randomization of the magnetic spins. Antiferromagnetic interaction persists at 0.03 mol and it gets stronger at 0.07 mol. Antiferromagnetism appears due to strong superexchange interaction of Gd^{3+} ions via O^{2-} ions.

References

[1].Fang,T., et.al Raman spectroscopy: A New Approach to Measure the Percentage of Anatase TiO_2 Exposed (001) Facets, *J. Phys. Chem.* C **116** (13),7515−7519, 2012.

[2].Wang,E., et.al Improved visible light photocatalytic activity of titania doped with tin and nitrogen, *J. Mater. Chem* **21**(1), 144-150, 2011.

[3].Serpone,N., et.al Size effects on the Photophysical Properties of Colloidal Anatase TiO_2 Particles: Size Quantization versus Direct transition in This Indirect Semiconductor, *J.Phys.Chem* **99**(45),16646-16654,1995.

[4].Wu,Wy., et.al Room temperature synthesis of single crystalline anatase TiO_2 nanowires, *Cryst. Growth Des.* **10** (4), 1646-1651,2010.

[5].Wang.D., et.al Concentration quenching of Eu^{2+} in $SrO.Al_2O_3:Eu^{2+}$ phosphor, *J,Lumin* **97** (10),1-6, 2002.

[6].Chen,W., et.al Electronic properties of anatase TiO_2 doped by lanthanides. A DFT+U study, *Physica.B* **407** (6), 1038-1043, 2012

[7].Chetri,P., et.al Structural, optical, photocatalytic properties of TiO_2/SnO_2 core-shell nanocomposites: An experimental and DFT investigations, *Chem. Phys. Chem* **434** , 1-10, 2014.

[8]. Khataee,A.R., et.al., Kinetic Modeling of Liquid Phase Photocatalysis on Supported TiO_2 Nanoparticles in a Rectangular Flat-Plate Photoreactor, *Ind.Eng.Chem .Res* **49** (24), 12358-112364, 2010.

[9].Xu,A.W., .et.al The preparation, Characterisation, and their Photocatalytic Activities of Rare-earth- Doped TiO_2 Nanoparticles, *J.Catal* **207** (2), 151-157, 2002.

[10]. Liqiang,J., et.al Review of photoluminescence performance of nano-sized semiconductor materials and its relationship with photocatalytic activity, *Sol Energ Mat Sol C.* **90** (12) ,1773-1787, 2006.

[11]. Devi,LG., et al Influence of Mn^{2+} and Mo^{6+} dopants on the phase transformations of TiO_2 lattice-and its photocatalytic activity under solar illumination, *J.Catal.*

A: Chem. **328** (1-2), 44-52,2010

[12]. Karakitsou ,K. E &Verykios ,X. E. Effects of altervalent cation doping of titania on its performance as a photocatalyst for water cleavage, *J.Phys.Chem* **97** (6), 1184-1189, 1993.

[13]. Wong,H.T., et.al. Magnetic and luminescent properties of multifunctional GdF_3:Eu^{3+} nanoparticles, *Appl. Phys. Lett.* **95** (2),022512, 2002.

[14]. Petersen,M., et.al Structural, electronic and magnetic properties of Gd investi gated by DFT+U methods: bulk, clean and H-covered (0001) surface, *J. Phys.: Con dens. Matter* **18** (30), 7021- 7043, 2006.

[15]. Jacobsohn.,L.G., et.al Multifunction Gd_2O_3: Eu nanocrystals produced by solution combustion synthesis: Structural, luminescent, and magnetic characterization, , *J. Appl. Phys.* **103** (10), 104303, 2008.

[16]. Hafez,H.S., et.al. Hydrothermal preparation of Gd^{3+} doped Titanate Nanotubes: Magnetic Properties and Photovoltaic performance, *Int.J.Photoenergy* **2009**, 240402, 2009.

[17]. Adhikari,R., et.al Gd doped SnO_2 nanoparticles: Structure and Magnetism , *J. Magn. Magn. Mater* **322** (22), 3631-3637,2010.

[18]. Ghsosh,S., et.al Defect Driven Magnetism in Luminescent n/p Type pristine and Gd substituted SnO_2 Nanocrystalline thin films, *Appl. Mater. Interfaces* **4** (4) , 2048–2056, 2012.

[19]. Oprea ,O., et.al Photoluminescence , Magnetic Properties and Photocatalytic Ac tivity of Gd^{3+} doped ZnO Nanopartciles, *Dig J Nanomater Bios* **7** (4) ,1757-1766, 2012.

[20]. Ney,V., et.al Structural and magnetic analysis of epitaxial films of Gd doped ZnO, *Phys. Rev B* **85** (23), 235203-235207, 2012.

[21]. Dimiri,M.C., et.al Ferromagnetism in rare earth doped cerium oxide bulk samples *Phys. Status Solidi A* **209**(2), 353–358, 2012.

[22]. Wang, J., et.al Structure and magnetic properties of pure and Gd doped HfO_2 thin Films, *App. Phys* **99** (8), 08M117, 2006 .

CHAPTER 7

Extending photocatalytic activity of TiO_2 nanoparticles to visible region of illumination and the study of magnetic property of Er doped TiO_2 nanoparticles.

Erbium is a member of the lanthanide rare earth series and possess 11 electrons in the *4f* shell. In the trivalent charge state the *4f* electrons are shielded from the host environment by completely filled *5s* and *5p* electronic shells [1]. Er doped TiO_2 nanocrystals are mainly used for optical applications [2-3]. Bouzidi.et.al [4] reported optical laser application of Er doped SnO_2 nanoparticles. In this chapter we will first present a detail discussion on the optical properties of Er doped TiO_2 nanoparticles. Then we will discuss the photocatalytic activity of the samples using visible light. In the later part of the chapter we will focus on the magnetic properties of the materials. The synthesis procedure of the material has already been discussed in Chapter-2. The structural and morphological features are studied with X-ray diffraction (XRD), Raman spectroscopy and transmission electron microscope. The elemental composition verified with the help of EDX spectra shows signature of Er, Ti, O as constituent elements in the doped samples. X-ray photoelectron spectroscopy reported in Chapter 2 establishes the +3 oxidation state of the Erbium ions.

7.1. Shifting of absorption peak to visible region and delay of charge carrier recombination process.

7.1.1. Doping effect on absorbance spectra and Band gap of TiO_2 nanoparticles

The absorbance spectra of all the samples are shown in Fig.7.1. The absorption band edge of TiO_2 nanoparticles appears at 340 nm. Incorporation of Erbium ions in the TiO_2 lattice shifts the absorption edge to the visible region. The spectra of Er doped TiO_2 nanoparticles shows 5 distinct absorption peaks at 446, 492, 521, 543, 656 nm corresponding to the transition of Er^{3+} from ground state $^4I_{15/2}$ to the excited state $^2F_{3/2}$, $^2F_{7/2}$, $^2H_{11/2}$, $^4S_{3/2}$, $^4F_{9/2}$ respectively [5,6]. As compared to undoped TiO_2 the absorbance of the doped samples are increased and this behavior is attributed to the creation of some intermediate energy levels

in the band gap of TiO_2 that makes them more susceptible in the visible region.

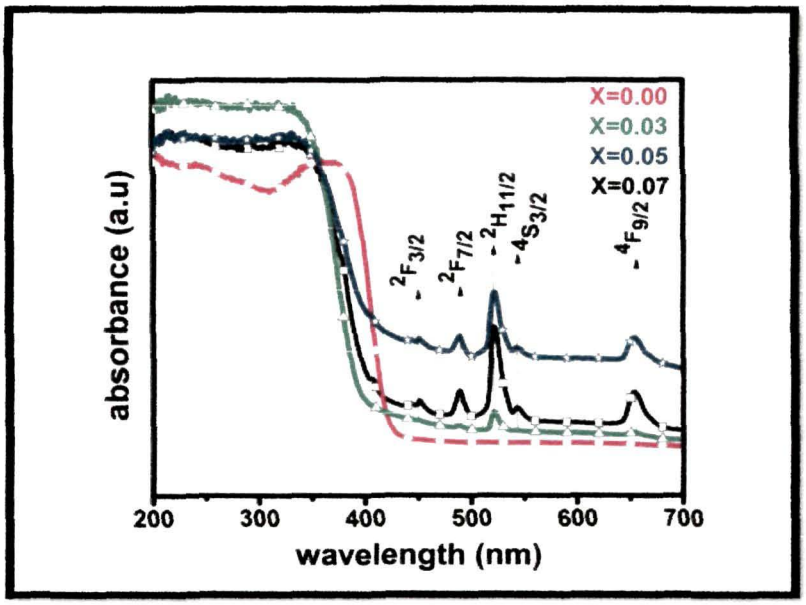

Fig.7.1: Absorbance spectra of all the samples.

The band gap of the samples are calculated by drawing a line on the linear part of the curve $[F(R)h\nu]^{1/2}$ vs hν at $[F(R)h\nu]^{1/2} = 0$. Fig.7.2 shows the band gap of undoped and Er doped TiO_2 nanoparticles. Pure TiO_2 nanoparticles show a blueshift (3.3 eV) in the band gap compared to its bulk counterpart (3.20 eV) due to quantum confinement effect. But as dopant concentration increases the band gap value decreases upto 0.05 mol and than increases at 0.07 mol of Er^{3+}. The narrowing in band gap after erbium doping is due to the formation of Er 4*f* and oxygen defect levels beneath the conduction band minimum [7]. In pure TiO_2 electronic transition takes place from valence band to conduction band. However upon Er doping the electrons are not directly excited to the conduction band, the unoccupied 4*f* levels and oxygen defects capture the electrons. These subband states of Er^{3+} and oxygen defects are responsible for the band gap reduction in TiO_2. Further it is speculated that at dopant concentration of 0.07 mol there is a slight increase in the band gap as compared to 0.05 mol. This increase in the band gap at this concentration is attributed to the Burstein-Moss effect [8].

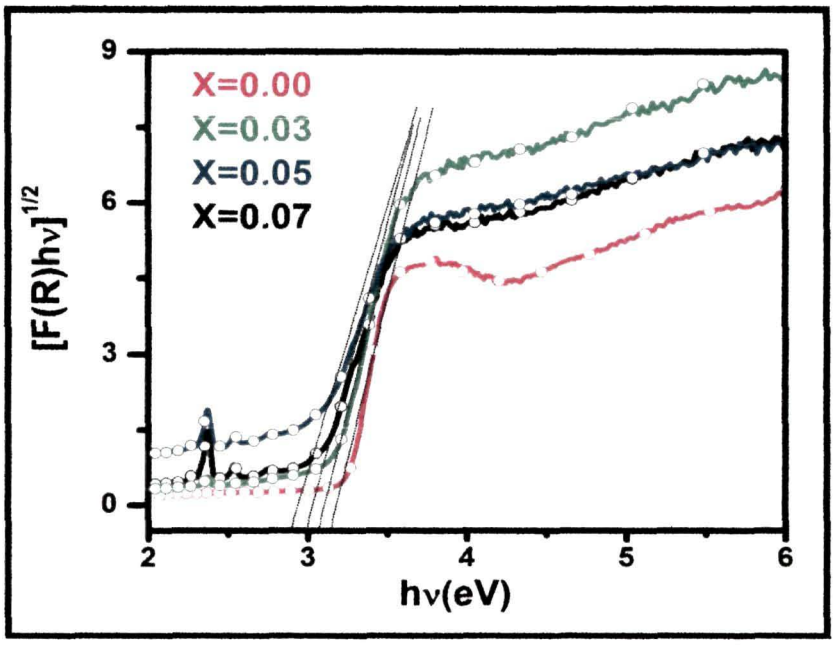

Fig.7.2: Band gap calculation of undoped and doped sample

7.1.2 Photoluminescence spectra analysis

Fig.7.3 shows the emission spectra of pure and Er doped TiO_2 nanoparticles at an excitation wavelength of 320 nm. The asymmetry in PL emission peaks infers that the observed luminescence is superposition of different types of defect related emissions. The UV emission peak at 392 nm is owing to the phonon assisted indirect transition from edge (X) to the center (Γ) of the Brilliouin zone , X_{1b} to Γ_3 [9]. The defect emission peaks ranging from 429 nm to 538 nm are strong in case of doped samples while it is reverse in case of undoped TiO_2. The peak at 429 nm is attributed to self trapped excitons (STE) originated by interactions of conduction band electrons localized on the Ti *3d* orbital with holes present in the O *2p* orbital of TiO_2 [10]. In the doped samples we observe a peak shifting from 429 nm to 436 nm and this is due to incorporation of additional defect states. The peak at 462 nm is attributed to the surface oxygen vacancies. The low intensity visible peak centered at 538 nm originates from the radiative recombination of electrons via intrinsic defects [11]. The signature of peak at 489 nm is due to charge transfer transition

from Ti^{3+} to oxygen anion in a TiO_6^{2-} complex associated with oxygen vacancy [12].

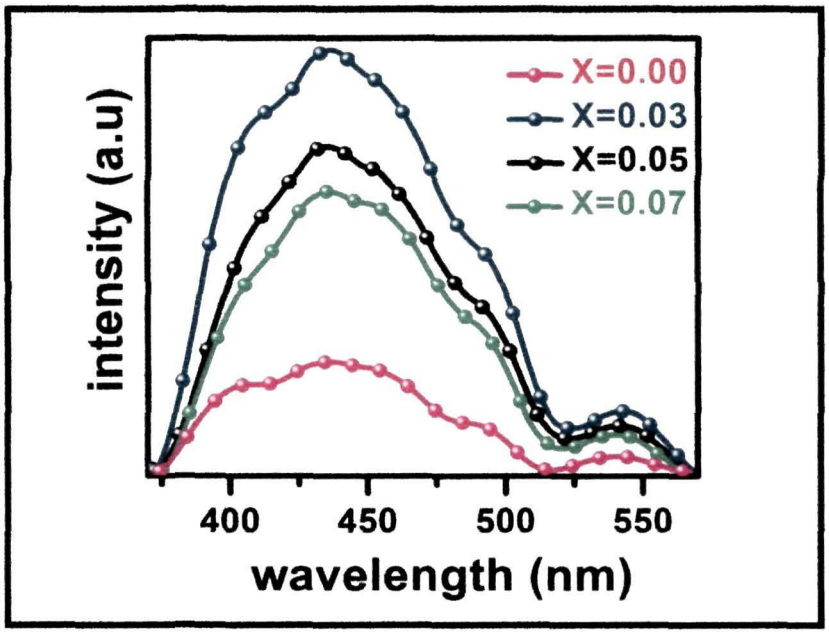

Fig.7.3: Photoluminescence spectra of the samples with an excitation wavelength 320 nm.

Optically excited rare earth doped semiconductors suffer from the so called concentration quenching effect [13]. According to this effect the emission intensity of the semiconductors decreases with increase in dopant concentration. The probability for concentration quenching effect depends on the distance between the dopant ions [13]. At low dopant concentration the interactions between the dopant ions are too weak to have an effect on the energy levels of each dopant ion. But as the dopant concentration increases the distance between the ions and the defects decreases. Decrease in the distance increases the interactions between the ions forming quenching centers. Further from the spectra it is speculated that compared to undoped TiO_2 the emission intensity of the doped TiO_2 samples is greatly enhanced inferring that the emission energy of TiO_2 is consumed for the excitation of Er^{3+} ions [14]. The host TiO_2 lattice therefore not only proves an ideal host for well dispersed and highly accommodated concentration of Er^{3+} but also function as a good sensitizer to proficiently absorb light and transfer energy to Er^{3+}. Based on Frindell.et.al

[15] model the energy transfer mechanism in Er doped TiO_2 nanoparticles can be surmised as follows: after light absorption in the band gap of TiO_2 and subsequent relaxation to the defect states the excited electrons are transferred to the various crystal field states of the Er^{3+} ion. This energy transfer process is illustrated in the Schematic model, Fig.7.4. The PL emission intensity is contributed by both radiative and non-radiative recombination. Radiative recombination increases the PL intensity while non-radiative recombination reduces it. In our study the emission intensity of the doped sample decreases with the increase in Erbium concentration. Actually with the increase in Er concentration the electrons jump form one *f* state to another and forms some quenching centers. The electrons after passing through channel of dopant and defects, ultimately finds recombination centre and emit light. But in the process the time period to undergo recombination process increases and in turn quenches the emission intensity.

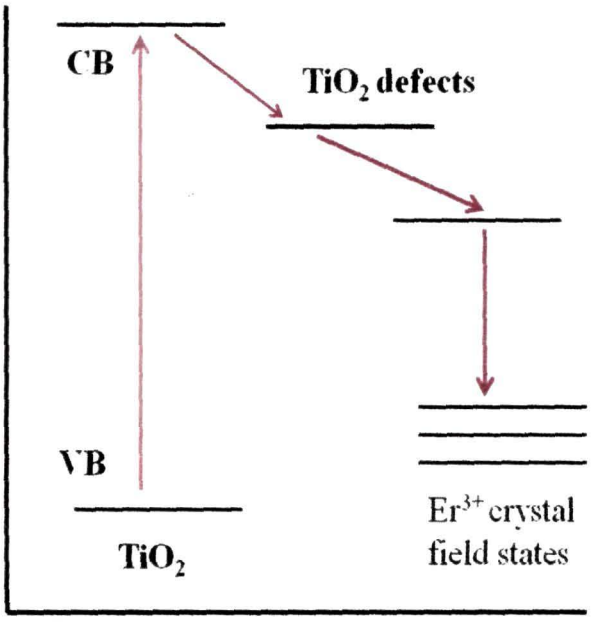

Fig.7.4: Schematic showing the energy transfer process.

However, in the photoluminescence spectra we have not observed any Er^{3+} related emission peaks. It is possible that weak Er^{3+} ion emission peaks might be embedded in the

signal from a strong, deep-level emission [16]. Addition of metals and/or transition metals increases the number of surface defects and the surface area and surface defects play an important role in the photocatalytic activity of metal oxides [16].

7.2. Photocatalytic activity study

For the photocatalytic degradation charge separation is the rate determining step. The photocatalytic behavior of pure and Er^{3+} doped TiO_2 nanoparticles are investigated by observing the decomposition of phenol in aqueous solution. Fig.7.5 shows the photocatalytic degradation curve.

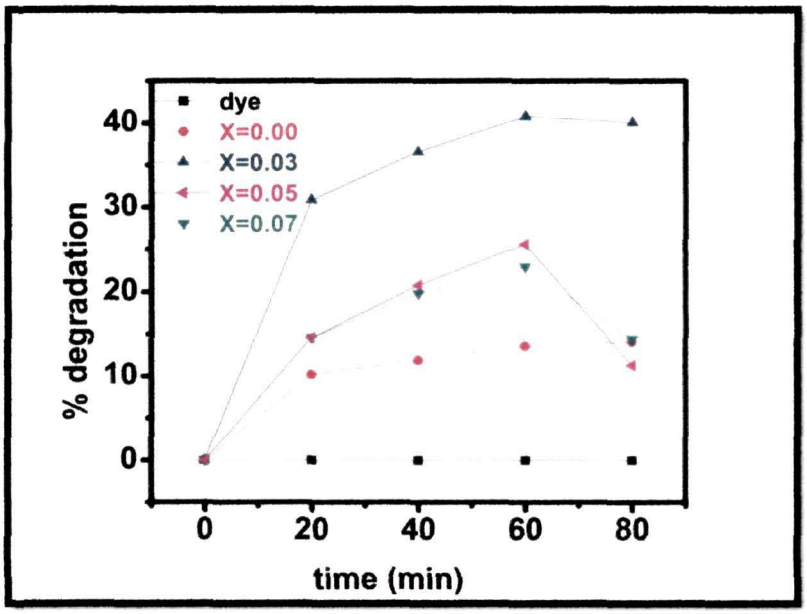

Fig.7.5: Photocatalytic degradation curve of all the samples

No degradation of phenol is observed in the absence of neither photocatalyst nor illumination. The rare earth doped TiO_2 photocatalyst display higher ability to phenol degradation as compared to pure TiO_2.

During the photocatalysis process the absorption of light by the photocatalyst leads to the excitations of electrons from valence band to the conduction band, thus generating electron-hole pairs. Incorportion of Er ions leads to the formation of sub-band gap states

below the conduction band of the semiconductor [23]. The electrons are excited from the valence band to the Er 4*f* level by visible light. Oxygen molecules dissolved in the suspension capture the electrons in the conduction band while the holes in the valence band are captured by OH^- or H_2O species absorbed on the surface of the catalyst to produce the hydroxyl radical. The process may be summed up with the help of the following reactions:

$$TiO_2/Er^{3+} \xrightarrow{hv} e^- + h^+$$
$$OH^\bullet + h^+ \xrightarrow{hv} OH^\bullet$$
$$O_2 + e^- \rightarrow O_2^-$$
$$\text{Phenol} + O_2^- \rightarrow \text{Products}$$
$$\text{Phenol} + OH^\bullet \rightarrow \text{Products}$$

The mechanism of photo-induced charge carriers controlling the variation in PL intensity has some strong correlation with the photocatalytic activity. According to Fig 7.3 and 7.5 it is found that the order of the photocatalytic activity is same as that of PL intensity, namely the stronger the PL intensity the higher the photocatalytic activity. During the process of PL oxygen vacancies and defects bind the photoinduced electrons so that PL signal can easily occur and the larger the content of oxygen vacancies the stronger the PL. In the photocatalytic process oxygen vacancies and defects become the centers to capture the photoinduced charge carriers so that the recombination process is delayed and the average lifetime is increased. Presence of Er ions enhances the fluorescence emission and resulted in increased generation of electron-hole pair concentration.

However, from the photocatalytic experiment it is speculated that the photocatalytic effect is not increasing monotonically as the doping amount is increased, the effect began to decrease when the Er concentration is increased upto 0.05 mol. This phenomena is mainly due to the fact that when the rare earth ion concentration is increased upto a certain level, the light penetrated into TiO_2 past the space charge layer, and the efficient separation of the light generated electron-hole pair is suppressed. There is thus an optimal concentration of the dopant ion at which the thickness of the space charge layer and light penetration is same [16]. Further , increase in concentration of rare-earth ions on the surface of TiO_2 increases

the recombination rate of electron-hole pair in turn reducing the photocatalytic activity.

7.3. Magnetic property study of the samples.

Room temperature magnetic measurements of the samples are carried out in the range of ±15 kOe. Fig.7.6a-b shows the room temperature magnetic behavior of undoped and Er doped TiO_2 nanopowders. Undoped TiO_2 shows diamagnetic (Fig.7.6a) behavior whereas Er doped TiO_2 (Fig. 7.6b) shows paramagnetism.

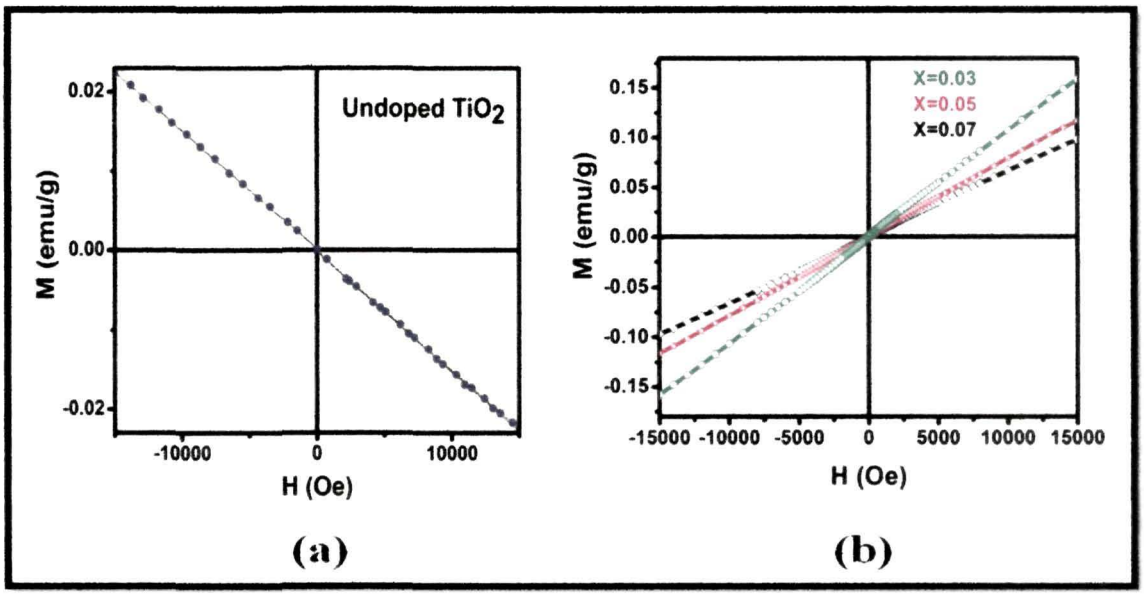

Fig.7.6: Room temperature M-H curves of (a) undoped (b) Er doped TiO_2 nanoparticles.

With the increase in Er concentration the saturation magnetization is found to decrease. This is believed to be due to strong Er^{3+}-Er^{3+} or Er^{3+}-O^{2-} -Er^{3+}antiferromagnetic interaction [17]. At lower dopant concentrations the magnetization comes from the isolated Er^{3+} ions. However, with the increase in dopant concentration the average distance between the Er^{3+} ion decreases and the Er^{3+} ions are now paired up. The pairing takes place nearest to the oxygen ligands bonded to the Er^{3+} ions. A strong anti-ferromagnetic super-exchange inter-action prevents the ferromagnetic alignment of the magnetic spins and thereby results in the reduction of the magnetization. Erbium being ferromagnetic in nature incorporation of Er

ions in the TiO_2 matrix is expected to bring, room temperature ferromagnetism with high magnetization. The electronic configuration of Er^{3+} is [Xe] $4f^{11}$ with 11 unpaired electrons in the $4f$ shell. These $4f$ electrons are shielded from the host environment by completely filled $5s$ and $5p$ electronic shells. Because of this shielding the interaction of these unpaired spins with the outermost ligands or other Er^{3+} is expected to be weak. These non-interacting and localized magnetic spins of Er^{3+} induce only paramagnetic moment. Paramagnetism has been reported in Er_2O_3 [18] and Er^{3+} doped SnO_2, ZnO etc [19,20], Dimiri.et.al reported magnetic properties of rare earth doped (RE=Nd, Sm, Gd, Tb, Er and Dy) CeO_2 [21]. The magnetism in their system was attributed to the presence of oxygen vacancies created due to addition of rare-earth dopants [21]. Qi.et.al studied magnetism in Er doped ZnO nanoparticles [22]. Presence of both ferromagnetic and paramagnetic phases was detected in their samples. The ferromagnetism was found to be decreased with the increase in Erbium concentration and the magnetic behavior was mainly attributed to the substitution of Zn^{2+} by Er^{3+} ions.

For further confirmation of the nature of magnetism in the system, we carried out temperature dependent magnetic measurements (M-T) for 0.03 mol and 0.07 mol Er doped TiO_2. Fig.7.7a-b shows the susceptibility (χ) *vs.* temperature (T) curves in the temperature range of 10-300 K at an applied field of 200 Oe. The zero field cooling (ZFC) and field cooling (FC) curves are completely overlapped upto 300 K and the nature of the curves follow the Curie-Weiss behavior of paramagnetism. The temperature dependent susceptibility (χ) curves were fitted with modified Curie-Weiss law-

$$\chi = \chi_0 + \frac{C}{T-\theta} \quad \text{----------} \quad (7.1)$$

Where χ_0 is diamagnetic susceptibility, C is Curie constant and θ is Curie-Weiss temperature that represents the magnetic exchange interaction between the localized spins. For 3 mol % Er doped TiO_2 the Curie-Weiss fitting gives the following results, $\chi_0 = 3.013\times10^{-6}$, $C = 0.0016$, $\theta = (-)\ 3.4266$. For 0.07 mol Er doped TiO_2 the fitted values for χ_0, C and θ are 2.86×10^{-6}, 0.0014 and (-) 3.789 respectively. The negative value of Curie-Weiss temperature indicates existence of antiferromagnetic interaction in the system. As

compared to 0.03 mol Er, the value of θ is higher at 0.07 mol.At this concentration Er^{3+} ions undergo superexchange interaction with each other via O^{2-} ions. This results in the antiparallel arrangement of the magnetic spins of Er 4*f* shell present in the nearest neighbor The large negative value of θ confirms increased anti-ferromagnetic interactions on increasing the Er content to 0.07 mol. Hence, from the results of M-H and M-T it is anticipated that presence of both paramagnetic and antiferromagnetic interactions contributes to the magnetic behavior of the doped samples.

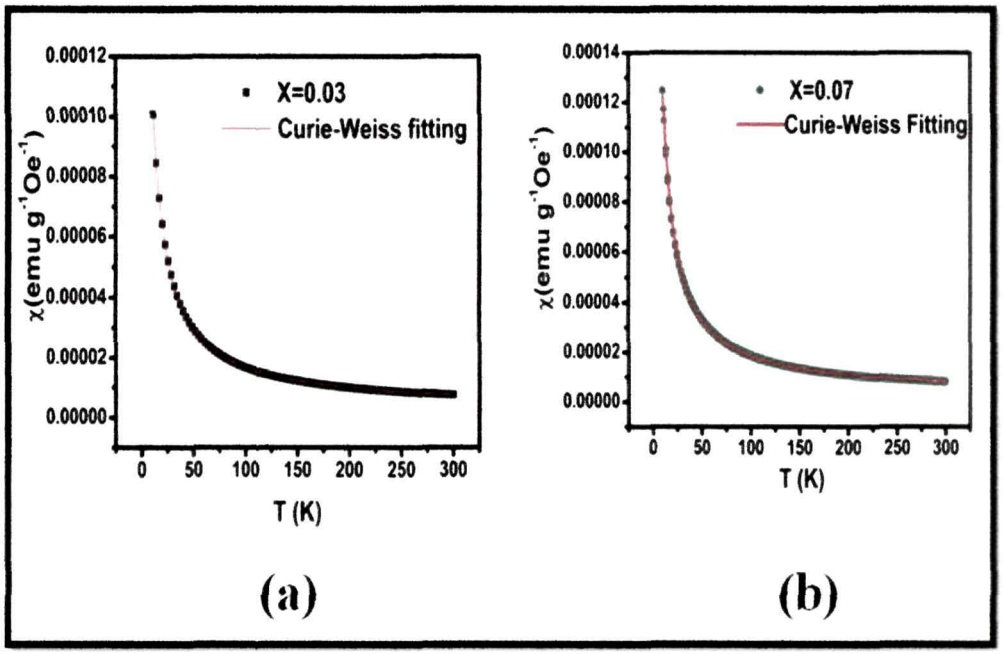

Fig.7.7 : Susceptibility (χ) vs. temperature (T) curves (a) 0.03 mol and (b) 0.07 mol Er doped TiO_2 nanoparticles.

The magnetic behavior of the samples is also monitored at 10 K , at an applied magnetic field of ± 45 kOe, Fig.7.8. Paramagnetism is retained by the samples even at this low temperature. Unlike the linear M-H curves of the samples measured at room temperature, the magnetic curves at 10 K tries to get the shape of hysteresis. There is a small bent in the M-H curve and this is possibly due to the minimization of the thermal randomization of the

magnetic spins at 10 K. It is further noticed that there is enhancement of magnetization in 0.07 mol as compared to 0.03 mol Er doped TiO_2 nanoparticles. This is possibly due to the decrease in the thermal randomization and contribution of large numbers of localized non-interacting magnetic spins of Er^{3+}.

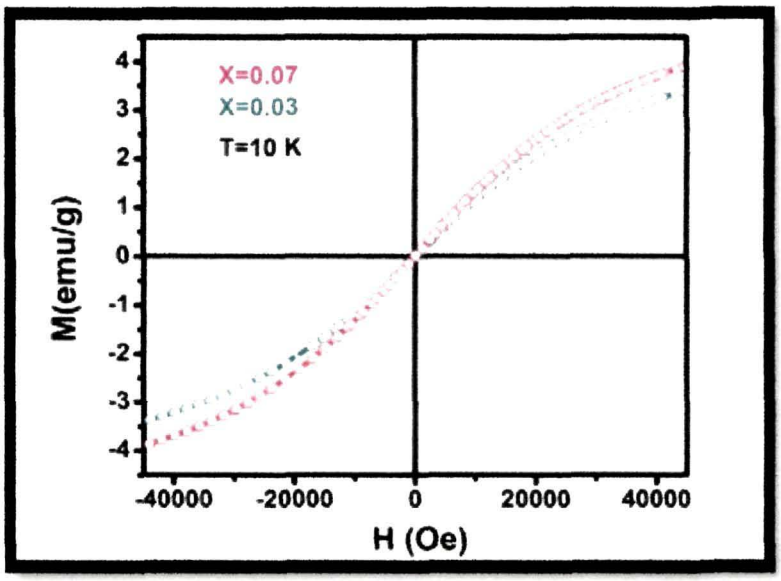

Fig.7.8: M-H curves of 0.03 mol and 0.07 mol Er doped TiO_2 measured at 10 K.

7.4. Conclusions

The detailed analysis of this chapter leads to the following conclusions:

1. Erbium doping shift the absorption edge of TiO_2 to visible region. The photoluminescence spectra shows distinct peaks related to Er ions. The photocatalytic activity is greatly enhanced due to doping. The order of photocatalytic activity follows the emission intensity spectra: namely stronger the PL intensity greater the photocatalytic activity. The photocatalytic activity however decreases with the increase in concentration inferring there exists a optimum conc-tration of the material to show superior photocatalytic activity. In our study 0.03 mol dopant concentration is the optimum limit to get greater photocatalytic activity.

2. Magnetic measurements reveal predominant paramagnetic nature at room temperature as well as at 10 K. The high magnetization observed at 10K is due to minimization of thermal randomization of the magnetic spins that leads to more effective ordering of the 4*f* electrons. The temperature dependent magnetic measurements reveals concave nature without any bifurcation of the FC and ZFC curve. The results clearly suggest the absence of any ferromagnetic interaction. There is persistence of antiferromagnetic ordering in all the doped samples as anticipated from the negative Curie-Weiss temperature in the temperature dependent magnetization curve. This part of the magnetic study constitute an original work to the best of our knowledge.

References

[1].Zavada,Z.M., et.al. Optical and magnetic behavior of erbium doped GaN epilayers grown by metal-organic chemical vapor deposition, *Appl. Phys. Lett* **91** (5), 054106, 2007

[2].Ravaro,L. P., et.al. Raman and photoluminescence of Er^{3+} doped SnO_2 obtained via the sol-gel technique from solutions with distinct pH, *Opt. Mater.* **33** (1), 66-70, 2010.

[3].Wu,J. & Coffer,J. L. Emissive erbium doped silicon and germanium oxide nanofibres derived from an electrospinning process , *J. Phys. Chem. C* **111** (43) ,16088-16091,2007.

[4].Bouzidi,C., et.al.Strongly Er^{3+} sol-gel SnO_2 for optical laser and amplifier applications, *Appl. Phys. B* **90** (3-4) ,465-469,2008.

[5].Xiao,Z. et.al. Optical properties of Tm-Er Co-doped Aluminate glasses, *J. Korean. Phys. Soc* **52** (11), S54-S57, 2008.

[6].Obadina,V.O and Reddy.B.R. Investigation of Silver Nanostructures and Their Influence on the Fluorescence Spectrum of Er doped Glassses, *Optics and Photonics Journal* **3** (1) , 45-50 ,2013.

[7].Ravaro, L.P.et.al Visible emission from Er doped SnO_2 thin films deposited by sol-gel, *Ceramica* 53, 187-191, 2007.

[8]. Choudhury,B. et.al Extending Photocatalytic activity of TiO_2 nanoparticles to visible region of illumination by Doping of Cerium, *Photochem and Photobio* **88** (2),1-8, 2012.

[9].Liu, Y. & Claus, R.O. Blue light emitting nanosized TiO_2 colloids, *J. Am. Chem. Soc.* **119** (22), 5273-5274, 1997.

[10]. Wu,Wy., et.al Room temperature synthesis of single crystalline anatase TiO_2 Nanowires *Cryst. Growth Des.* **10** (4), 1646-1651,2010.

[11]. Serpone,N., et.al Size effects on the Photophysical Properties of Colloidal Anatase TiO_2 Particles: Size Quantization versus Direct transition in This Indirect, *J.Phys.Chem* **99** (45),16646-16654,1995.

[12]. Yu, J. C.et.al. Effects of F- doping on the Photocatalytic Activity and Microstructures of Nanocrystalline TiO_2 powders, *Chem. Matter.* **14** (9) ,3808- 3816, 2002.

[13]. Benz, F & Strunk,H.P Rare earth luminescence: A way to overcome concentration quenching , *AIP.Adv.* **2**, 042115, 2012.

[14]. Chowdhury,P.S.et.al Influence of nanoenvironment on luminescence of Eu^{3+} activated SnO_2 ,*Solid State Comm* **131** (12) ,785–788, 2004.

[15]. Frindell, K.L.et.al Visible and near-IR luminescence via energy transfer in rare-Earth doped mesoporous titania thin films with nanocrystalline walls, *J. Solid State Chem* **172** (1), 81–88, 2003.

[16]. Yu,K.S., et.al. Synthesis, Characterisation and Photocatalysis of ZnO and Er-doped ZnO, *J. Nanomater.* **2013**, 1-5, 2013.

[17]. Sambasivam,S., et.al Antiferromagnetic interactions in Er doped SnO_2 DMS Nanoparticles, *J.Nanopart.Res.* **13** (10) , 4623-4630, 2011.

[18]. Chen, X.B., et.al. Synthesis of erbium oxide nanosheets and up-conversion Properties, *Nanotech* **22** (29), 295708, 2011.

[19]. Yang, L., (Er, Yb)-co-doped multifunctional ZnO transparent hybrid materials: fabrication, luminescent and magnetic properties., *J. Phys. D: Appl. Phys.* **44**, ,155404 , 2011.

[20]. Bhaumik, S., Optical and magnetic properties of Er doped SnO_2 nanoparticles, *Phys. Status Solidi A* **210** (10) ,2146–2152, 2013.

[21]. Dimiri, M.C., et.al. Ferromagnetism in rare earth doped cerium oxide bulk samples, *Phys. Status Solidi A* **209** (2), 353–358, 2012.

[22]. Qi, J., et.al. Magnetic properties of Er doped ZnO films prepared by reactive magnetron sputtering, *Appl. phys. A* **100** (2) ,79-82, 2010.

CHAPTER 8

Concluding remarks and future directions

8.1. Thesis conclusion

The important point of findings in the thesis are

i. Pristine and metal doped TiO_2 nanoparticles are prepared successfully by simple sol-gel method. Anatase phase is preserved even after doping. Doping influences the position , intensity and width of the diffraction peaks. Presence of the dopant ions in the host matrix disturbs the Ti-O bond by forming oxygen vacancies and result in the shifting in the Raman peaks to higher wave number. XPS results confirm that Ni and Mn are in the +2 state whereas the rare-earth dopant ions: Gd, Er are in the +3 state.

ii. In chapter 3 we have seen that annealing at 650°C results in the formation of anatase-rutile mixed phase. A comparison in the band gap indicates that pure anatase and rutile phase have band gap in the UV region whereas the mixture of these phases have lower band gap and corresponds to the visible region. Presence of defects at the interface of these two phases act as hot spots to enhance the photocatalytic degradation of phenol under visible light irradiation.

iii. Doping of nickel generates large number of non-radiative oxygen vacancies. These oxygen vacancies act as trap center and separate the charge carrier for a longer time. Room temperature ferromagnetism is noticed in the doped sample and the magnetization decreases with the increase in doping concentration. Reduction of magnetization in our system with the increase in dopant concentration is due to Ni^{2+}-O^{2-}-Ni^{2+} super exchange interaction or due to Ni^{2+}-Ni^{2+} interaction. These

interaction leads to anti-parallel alignment of spin, enhancing the anti-ferromagnetic interaction and reducing the overall magnetization

iv. Mn doping distorts the structural quality and band structure of TiO_2 lattice by forming large number of defects. Using density functional theory presence of these defect states due to Mn incorporation has further been confirmed. PL spectra shows that doping is neither introducing any manganese related peak nor is shifting the peak position only quenching in the emission intensity is noticed for all the doped samples. Magnetic measurements carried out under two different annealing atmosphere suggests that presence of adequate number of oxygen vacancies are necessary to bring about ferromagnetism in the system. From the XRD, Raman spectra we find that although oxygen vacancies are generated in air annealed samples but their numbers are insufficient to bring about ferromagnetic ordering. In vacuum annealed samples both ferromagnetic and antiferromagnetic interactions persist. The oxygen vacancies form an impurity band below the conduction band and thereby lead to spin polarization of the dopant ion contributing to ferromagnetism. Some oxygen anions are also present in the system. These oxygen anions undergo super exchange interactions with Mn^{2+} ions (Mn^{2+}-O^{2-}-Mn^{2+}) and thereby degrade the magnetization. In oxygen deficient TiO_2, as the possible presence of metal impurities are ruled out so we believe that in undoped TiO_2 it is only the oxygen vacancies and their densities that influence the ferromagnetism.

v. In case of Gd doping *ab initio* calculation based on density functional theory shows that the Gd ions are localized , indicating that they mainly act as charge carrier trapping centers and delay the electron-hole recombination rate beneficial for enhanced photocatalytic activity. Magnetic study reveals that due to the shielding of $4f$ shell of Gd^{3+} ions by $6s5d$ shell the direct exchange interaction of these Gd^{3+} ions with other Gd^{3+} ions is weak. These non-interacting and localized magnetic spins of Gd^{3+} results in the paramagnetic nature of the sample. The magnetization carried out

at 10 K tries to get the shape of hysteresis and attain very high magnetization. This is expected due to the reduction of thermal randomization of magnetic spins.

vi. Doping of Er into TiO_2 expanded the range of absorption and enhance the intensity of fluorescence. The results of the experiment highlighted that the incorporation of Er modified the optical properties of TiO_2 and greatly improve the photocatalytic activity. Magnetic measurements carried out at room temperature and at 10 K manifest paramagnetic nature of the sample. There is persistence of anti-ferromagnetic interaction and the interaction gets stronger at 10 K.

vii. Introduction of the dopant ion in the titania matrix alters the electronic structure and induces visible light absorption by introducing localized electronic states within the band gap. The incorporated ions creates different surface structure that intrinsically alter the surface transfer of charge carriers and hence the photocatalytic activity. The emission intensity of TiO_2 is largely increased after rare-earth doping and this is attributed to the mixing of *s-p* electrons of the host matrix with the *d-f* electrons of the rare-earth ions [1].

A comparison of the photocatalytic activity of the dopants reveals that Mn^{2+} and Gd^{3+} display higher photocatalytic activity as compared to Ni^{2+} and Er^{3+} doped TiO_2 nanopaticles. This enhanced activity can be critically attributed to stable unique half filled electronic structure of the dopant ions, in accordance with previous reports [2-4]. Manganese has d^5 and Gd has f^7 electronic configuarion. When these dopant ion traps electron/hole there is considerable loss in spin energy due to change in the electronic configuration [5]. These half filled orbitals serves as shallow trap for the charge carriers to accelerate interfacial charge transfer process thereby generating highly reactive oxidative species – superoxide and hydroxyl radicals which are the potential candidates in photocatalytic process.

A close analysis further reveals that Gd^{3+} doped TiO_2 is showing maximum photocatalytic activity. Transition metal ion dopants differ from rare-earth dopants

in nature of *f* orbital. The electrons in the *f* orbital being shielded by completely filled outer $5s^2$ and $5p^6$, are weakely affected by the ions in the surrounding medium in the host matrix. These shielding by outer electrons minimizes the interactions between the dopant ions and the host matrix and thereby imparts longer lifetime to the charge carriers in turn contributing to enhanced photocatalytic activity [6]. The lowest photocatalytic activity of Ni^{2+} doped TiO_2 might be due to the presence of partially filled electronic configuration that results in formation of deep trap of the charge carriers rather than the shallow traps [5].

viii. As anticipated room temperature magnetic measurements of air annealed Mn, Gd, Er doped TiO_2 nanoparticles reveals paramagnetic behavior. However, the paramagnetic moments of rare earth ions are higher than transition metal ions [7]. For the transition metals, the 3*d* electrons are exterior and delocalized, the orbital momentum is zero, leading to small total magnetic moments per atom [8]. In RE metals, the 4*f* electrons are localized, exchange interactions are indirect, via 5*d* or 6*s* conduction electrons, the high orbital momentum leads to high total magnetic moments per atom [8,9].

Magnetic measurements carried out for vacuum annealed pristine and Mn doped TiO_2 nanoparticles reveals ferromagnetic nature of the samples. But the magnetization of vacuum annealed Mn doped TiO_2 is less as compared to vacuum annealed pristine TiO_2.

8.2. Future Direction.

- ✓ We have seen that that presence of two different phases in the same system shows improved catalytic activity due to the presence of defects. We will incorporate dopants in the biphasic system and carry out a comparative study to identify the system (that is undoped mixed phase and doped mixed phase) best suited for photocatalysis.

- ✓ To have better insight into the magnetic nature of the sample , we will do first principle calculation using DFT

- ✓ Magnetism of rare earth doped TiO_2 has not been explored fully. We will study the magnetic behavior of other rare earth doped TiO_2 nanostructures.

- ✓ Co-doping is a significant area of research , we will extend our work to study the photocatalytic activity and magnetic property of transition and rare-earth co-doped TiO_2 nanostructure.

References

[1]. Xu,S.J., et.al. Luminescence characteristics of impurities-activated ZnS nanocrystals prepared in microemulsion with hydrothermal method, *Appl.Phys.Lett* **73** (4), 478-480, 1998.

[2]. Choi,W., et.al The Role of Metal Ion Dopants in Quantum-Sized TiO_2: Correlation between Photoreactivity and Charge Carrier Recombination Dynamics, *J.Phys.Chem* **98** (52), 13669-13679, 1994.

[3]. Xu, A.W., The preparation, Characterization, and their photocatalytic Activities of Rare –Earth doped TiO_2 Nanoparticles, *J.Catal* **207** (2), 151-157,2002.

[4]. Graf,C., Preparation and characterization of doped metal-supported TiO_2- layers, *J. Photochem. Photobiol. A: Chem.* **188** (2-3), 226-234, 2007.

[5]. Devi, L. G., & Kumar, G.R., Influence of physicochemical-electronic properties of transition metal ion doped polycrystalline titania on the photocatalytic degradation of Indigo Caramine and 4-nitrophenol under UV/solar light, *Appl.Surf.Sci* **257** (7), 2779-2790, 2011.

[6]. Pandiyan,R. *Growth by Radio frequency sputtering and characterization of rare-earth doped wide band gap oxides*, Ph.D Thesis, University of Trento at Department of Physics, Italy, 2013.

[7] Jensen, J., & Mackintosh, A.R. *Rare earth magnetism: Structures and excitations,* Clarendon Press, Oxford, 1991.

[8] Sharma,M & Gairola, R.P., Performance Evaluation of ZnO based Rare Earth Element Doped Thin Films, *Orient J Chem* **29** (3), 1021-1025 ,2013.

[9] Dalpian,G.M., & Wei,S.H., Electron-induced stabilization of ferromagnetism in $Ga_{1-x}Gd_xN$, *Phys.Rev.B* **72** (11), 115201, 2005.

APPENDIX

Crystallographic and physical data of three phases of TiO_2

	Anatase	**Rutile**	**Brookite**
Chemical Formula	TiO_2	TiO_2	TiO_2
Crystal Structure	Tetragonal	Tetragonal	Orthorhombic
Space group	I41/amd	P42/mnm	Pbca
Crystal parameters (nm)	a=b=0.3785 c=0.9514	a=b=0.4594 c=0.2958	a=0.9184 b=0.5447 c=0.5245
Molecule/cell	4	2	8
Static dielectric constant	31	170	----------
Band Gap (eV)	3.2	3.00	----------

References

[1]. Diebold, U. The surface science of titanium dioxide, *Surf Sci Rep* **48** (5-8), 53229, 2003.

[2]. Winkler, J., *Titanium dioxide*, Vincentz, Germany, 2003.

List of Publications

1. Effect of manganese doping on the optical property and photocatalytic activity of nanocrystalline titania: Experimental and theoretical investigation: *J.Alloys and Compd* **583** , 578–586, 2014.
2. Magnetic property study of Gd doped TiO_2 nanoparticles. *J.Alloys and Compd* **601**, 201–206, 2014.
3. Enhanced visible light photocatalytic activity of Gadolinium doped titania: An experimental and theoretical study. *J colloids. Interface Sci* **439**, 54-61,2015.
4. Effect of nickel doping on the optical property and photocatalytic activity of titanium dioxide nanoparticle. *Micro & Nano Letters* **8** (4), 184-187, 2013.
5. Investigation of the optical property and photocatalytic activity of mixed phase nanocrystalline titania, *Applied Nanoscience* **4**,839-847, 2014.
6. Visible Light Photocatalytic Activity Of Manganese doped TiO_2 nanoparticles, IJIRD **1** (7), 24-31, 2012.
7. Participation of oxygen vacancies on paramagnetic to ferromagnetic transition in Mn doped TiO_2 nanoparticles. (Communicated).
8. Investigation of magnetic property of Er doped TiO_2 nanoparticles. (Communicated).

National/International Conference

1. Presented oral presentation in International Congress On Renewable Energy (ICORE) organized by Department of Energy , Tezpur University from 2-4th Nov, 2011.
2. Presented oral presentation in International Conference on Advanced Nanomaterials and Emerging Engineering Technologies, Sathyabama University, Chennai, 24-26th July, 2013.
3. Presented poster in International Conference on Material Science, Tripura University , 21- 23 rd , 2013.
4. Presented poster in National Seminar on Current Trends in Physics Research, Darrang College , Tezpur, 30 th Jan-1 st Feb, 2014.
5. Presented poster in National Conference On Physical Sciences Sept 13-14, D.H.S.K

College. Dibrugarh.

6. Presented paper 1 ª In-house symposium Dec 21, 2014, Tezpur University